UNIVERSITÀ DI PISA
Scuola di Dottorato in Ingegneria "Leonardo da Vinci"

Corso di Dottorato di Ricerca in
INGEGNERIA DELL'INFORMAZIONE
(SSD: Ing-Inf-01)

Tesi di Dottorato di Ricerca

Numerical simulation of transport and noise in low-dimensional devices for nanoelectronics

Demetrio Logoteta

Anno 2013

Sommario

La tesi presenta i risultati ottenuti nell'ambito della simulazione numerica della conduzione in sistemi di portatori a ridotta dimensionalità, realizzati su differenti materiali.
Aderendo al notevole interesse suscitato dalle potenzialità del grafene nello sviluppo di una tecnologia alternativa e con margini di miglioramento superiori rispetto alla attuale CMOS, sono state prese in considerazione alcune tematiche di rilievo relative al trasporto su grafene monolayer e bilayer.
Nel caso del grafene monolayer si è proceduto allo sviluppo di un metodo efficiente per la simulazione del trasporto in campioni di grandi dimensioni e in presenza di un potenziale elettrostatico con andamento quasi completamente generico. Il metodo, basato sull'approssimazione di funzione inviluppo, fornisce un'alternativa ai modelli atomistici, che richiederebbero, nei casi trattati, costi computazionali estremamente elevati. Alcune caratteristiche del trasporto su grafene monolayer sono state analizzate in dettaglio e inscritte nell'ambito della recente teoria delle Hamiltoniane non Hermitiane e della rottura spontanea della simmetria $\mathcal{PT}$ (parità e inversione temporale).
Nel caso del grafene bilayer le simulazioni sono state orientate all'interpretazione di misure di scanning gate spectroscopy in presenza dell'effetto Hall quantistico intero. Partendo da un modello semiclassico, originariamente sviluppato per sistemi di portatori bidimensionali ordinari, è stato messo a punto un metodo numerico in grado di riprodurre con buona accuratezza i risultati sperimentali e di fornirne una spiegazione.
L'ultimo tema trattato attiene allo studio della soppressione del rumore shot in dispositivi a semiconduttore mesoscopici. Le simulazioni di trasporto, con-

dotte su quantum wire definiti in eterostrutture GaAs/AlGaAs in presenza di disordine unidimensionale e bidimensionale, hanno indagato la possibilità di raggiungere un regime di trasporto completamente diffusivo, e, di conseguenza, una soppressione di un fattore 1/3 della densità spettrale di potenza del rumore shot, in campioni reali. I risultati ottenuti forniscono un'indicazione chiara dell'improbabilità che una tale soppressione si manifesti, contribuendo a risolvere l'apparente contrasto tra predizioni teoriche e misure sperimentali.

Abstract

This thesis presents the results obtained in the field of the numerical simulation of conduction in low-dimensional carrier systems on different materials.
Motivated by the significant interest aroused by the potential of graphene for the development of an alternative technology with margin for improvement larger than the current CMOS, we have taken into account some important issues related to transport in monolayer and bilayer graphene.
In the case of monolayer graphene, an analysis of transport in large area samples has been carried out within the envelope function approximation. An efficient numerical method has been developed for the simulation of conduction in the presence of a quite general electrostatic potential. The method provides an alternative to the atomistic approaches, that in the case of the considered domain would require an enormous computational burden. Some peculiarities of transport in monolayer graphene have been studied in detail, by inscribing them into the framework of the recent theory of non Hermitian Hamiltonians and the of the spontaneous breaking of the $\mathcal{PT}$ symmetry.
The simulations of transport on bilayer graphene have been oriented to the explanation of scanning gate spectroscopy measurements performed in the presence of the integer quantum Hall effect. We started form a semiclassical model, initially proposed for ordinary two-dimensional systems, and we have developed a numerical method able to reproduce with good accuracy the experimental results and to explain them.
The last subject we deal with is the suppression of the shot noise power spectral density in mesoscopic semiconductor devices. We simulated transport in quantum wires defined in GaAs/AlGaAs hetherostructures in the presence of one-

dimensional and two-dimensional disorder, investigating the possibility that a completely diffusive transport regime be established in real samples, and thus a 1/3 suppression of the shot noise power spectral density measured. The obtained results clearly indicate that it is unlikely to measure such a suppression and therefore contribute to explain the exisisting disagreement between theory and experiments.

Contents

Introduction

The scaling down of silicon-based CMOS technology has, until now, driven the growth of the electronics market. The economic returns have allowed to support the research efforts needed to overcome the difficulties encountered in keeping pace with the exponential trend of Moore's law. Nowadays, however, scaling is approaching the fundamental limit of the atomic dimensions, close to which it will inevitably stop, and the investigation of alternative technologies that can offer greater opportunities for improvement has become of primary importance.

Many different approaches have been proposed, based on new materials, the exploitation of new physical effects and the definition of new state variables other than the electric charge (e.g. spin, molecular state, photons, phonons, mechanical state, magnetic flux). A conservative approach consists in replacing the FET channel with a two-dimensional high-mobility carrier system. The control of current flow is still obtained via the modulation of the carrier density, induced by electrodes capacitively coupled with the carriers.

The first two-dimensional systems to be exploited for the implementation of new generations of devices have been the electron gases obtained at the interface of a heterojunction between materials with different band gap. Mobilities of $\sim 10^7$ $\mathrm{cm^2V^{-1}s^{-1}}$ have been obtained [1], and by electrostatically confining the electron gas, a variety of quantum devices, exploiting effects of energy quantization, tunneling and interference can be obtained.

Quite recently, the unexpected isolation of graphene [2] has opened new perspectives. Basically, graphene is a single atomic plane of graphite and from the point of view of electrical conduction it behaves as a zero-gap semicon-

ductor. Many of its unusual properties are currently the subject of intense research and debate. Moreover, these properties can be easily modified with the application of electric and magnetic fields, control of the geometry of the sample and chemical doping, resulting in a variety of possible applications. Graphene can be easily obtained from graphite without the need of expensive sample-growing techniques and, as a consequence of its intrinsic bidimensionality (it is not buried in a 3D structure), can allow further scaling of the devices while avoiding short-channel effects. Values of mobility at room temperature of $10,000 - 15,000$ cm^{2}V^{-1}s^{-1} are typically measured for graphene on SiO_2 [2,4], and values of $\sim 10^6$cm^{2}V^{-1}s^{-1} have been reached for suspended graphene at low temperature [5].

Besides digital applications, which rely on narrow graphene nanoribbon FETs, in which a band gap is obtained as a result of the strong lateral confinement, graphene is promising also for the development of new radiofrequency devices and sensors. For such applications a band gap in the pristine graphene sheet is generally not required and devices can be based on large-area flakes, avoiding in this way the significant mobility degradation measured in nanoribbons.

Besides single layer graphene, also bilayer graphene (two stacked layers of graphene coupled to each other) have drawn the attention of the scientific community, since it exhibits properties in many respects different from the monolayer one. In view of technological applications, the possibility to tune its band gap by applying an external electric field [3] attracts considerable interest. Both monolayer and bilayer graphene display an Integer Quantum Hall effect distinctively different from that observed in conventional two–dimensional systems; this aspect is the object of intense theoretical study, as well as of interest for using graphene in the definition of a handy metrological standard for the resistance.

In this thesis we deal both with the numerical simulation of transport in monolayer and bilayer graphene, though we treat them in different contexts, the first in the presence of a generical electrostatic potential, the second threaded, in addition, by a strong orthogonal magnetic field and thus in the presence of the Integer Quantum Hall effect. In both cases we consider large area graphene samples; since micron-sized flakes are the most common sample format on

which measurement are made, this allows a direct comparison of the simulation results with the experiments. On the other hand, in order to limit the computational burden, numerical simulation cannot be based on an atomistic model, but must rely on different, more approximate, techniques. In detail, the simulations we have performed are all based on a $\boldsymbol{k} \cdot \boldsymbol{p}$ approximation.

An important topic in the study of mesoscopic devices is their characterization in terms of noise. Indeed, in mesoscopic devices the useful signal is inevitably very small, and a careful optimization of the signal–to–noise ratio is mandatory. Moreover, the analysis of noise provides information about the carrier interactions and dynamic that can not be obtained by taking into account conductance alone. In the literature particular attention has been devoted to the shot noise suppression phenomena. Shot noise is the intrinsic component of noise that dominate at low temperature; in mesoscopic devices its power spectral density can be suppressed, with respect to the value given by the Schottky formula, as a result of the effect of electron interactions. The entity of this suppression depends on the particular kind of device considered and on the transport regime established in it.

In this thesis we address the debated issue of the measurability of the 1/3 suppression of the power spectral density of the shot noise in mesoscopic semiconductor devices, referring, in particular, to quantum wires in GaAs/AlGaAs heterostructures. Also in this case the large size of the considered devices has required the adoption of a continuum approximation in the simulation models.

We conclude these introductive remarks with a short outline of the thesis.

In **Chapter 1** we present and compare the numerical methods developed for the simulation of non dissipative transport in large area graphene samples when the system is perturbed by an external electrostatic potential. Some other reformulations of the problem are presented in **Appendix A**. The last section of the chapter is devoted to an analytical study of some peculiar properties of the transport in armchair graphene nanoribbons.

Chapter 2 deals with the simulation of experiments of scanning gate spectroscopy on bilayer graphene in the presence of the Integer Quantum Hall effect. We first discuss the model we have considered; then we present the simulation results, systematically comparing them with the available experimental

data, of which we propose an interpretation.
In **Chapter 3** We discuss the results of a numerical investigation, performed on disordered quantum wires in GaAs/AlGaAs heterostructures of the conditions under which a completely diffusive transport regime is established and thus a suppression by 1/3 of the power spectral density of the shot noise is obtained.

Chapter 1

Simulation of transport in large area graphene samples

In this chapter we address the issue of the numerical simulation of transport in large area samples of monolayer graphene, when an external electrostatic potential is present. As pointed out in the introduction of this thesis, this holds a technological relevance in view of the implementation of large area graphene-based radiofrequency and sensor devices. Moreover, this allows for a close comparison with several experimental measurements, tipically performed on micron-sized samples. An external potential (namely a potential superimposed on top of that due to the atomic structure of the crystal) is always present, since it results from the effect of electrodes capacitively coupled with the flake and the perturbations induced by charged impurities. The considered size of the simulation domains, however, does not allow numerical simulation with atomistic detail and more approximate techniques have to be used. We refer, in particular, to a two-band $\boldsymbol{k} \cdot \boldsymbol{p}$, envelope function approximation, within which the dispersion relationship of monolayer graphene is linear; as a consequence, electrons can be assimilated to massless relativistic particles and can

be described by means of the Dirac differential equation.
This approach has been largely used for the numerical simulation of transport in armchair nanoribbons in the presence of a potential constant in the confinement direction (which we refer to as transverse direction) [6–8], exploiting analytical expressions for the wave function [9–11].
However, if a generic potential is considered, no analytical expression is available and the Dirac equation has to be numerically solved. Due to the fundamental problems deriving from the application of a standard discretization scheme to the direct-space solution of the Dirac equation, this represents a nontrivial task. Tworzidło *et al.* [12] successfully performed a real-space transport analysis of armchair graphene ribbons with a large aspect ratio, for which (being the precise boundary conditions largely uninfluent) periodic boundary conditions can be assumed. In order to overcome the above mentioned problems, they solve the two-dimensional Dirac equation adopteding the Stacey discretization scheme [14,15]. More recently, Hernández *et al.* [13] have studied the transport properties of a zigzag and of an armchair ribbon in the direct space, with the exact boundary conditions. In the first case they have adopted the Susskind discretization [16] in the transverse direction and the Stacey one longitudinally, while in the second case they have used the Stacey discretization in both directions.
In this chapter we propose some different numerical approach for the transport analysis, applied to a large area armchair graphene nanoribbon, with which we model the simulation domain. We will consider exact Dirichlet boundary conditions at the edges and we include the possibility of width discontinuities in the ribbon, that allow, as we will see, the approximation of domains of arbitrary shape. We perform the computation of the conductance with a recursive scattering matrix approach, mapping the two-dimensional problem into a set of interconnected one-dimensional ones. The most demanding task in this procedure is the diagonalization of a set of one-dimensional Dirac equations, and most of this chapter is devoted to the investigation of different numerical method to efficiently solve this problem.
In the following, after an introduction to the envelope function approximation for graphene, we set formally the problem of the diagonalization of the Dirac

equation and we examine different numerical approaches to solve it. We begin by discussing finite differences approaches in the spatial domain; we will highlight the drawbacks of standard discretization schemes and propose several solutions to overcome them. Later, the problem will be reformulated in the Fourier domain and the numerical efficiencies obtained with the different approaches will be compared. Then, the remaining steps for the conductance calculation will be detailed. Finally, in the last section of the chapter, the properties of the solutions obtained for the Dirac equation will be analyzed in detail and interpreted in the framework of the theory of the Non-Hermitian Hamiltonian and $\mathcal{PT}$-symmetry breaking.

1.1 The band structure of graphene

Graphene is a single sheet of carbon atoms arranged in a hexagonal lattice. This structure is the result of the sp^2 hybridization of the $2s$, $2p_x$, $2p_y$ orbitals of each carbon atom and of the formation of three covalent σ bonds (at $2\pi/3$ angles each other) with the nearest neighbor atoms. The remaining single valence electrons per carbon atom occupy the $2p_z$ orbitals and give rise to the formation of bonding π and antibonding π^* bands. As the wavefunction associated to the σ bands are even under reflection with respect to the plane of graphene, while those associated to the π bands are odd, mixing is not possible and σ bands and π bands can be studied separately. Actually the almost delocalized electrons within π bands support electrical conduction in graphene, thus σ bands can be neglected, as a good approximation, for an analysis of transport. We proceed with the calculation of the band structure of graphene within a nearest-neighbours tight-binding approximation.

A hexagonal lattice is composite, with two atoms per unit cell, and can be split into two interpenetrating triangular Bravais lattices, which we refer to in the following as A and B sublattices (see Fig. 1.1). As a consequence, the two Bloch sums built with the $2p_z$ orbital of the carbon atoms lying on the A and on the B sublattices

$$\Phi_\alpha(\boldsymbol{k}, \boldsymbol{r}) = \frac{1}{\sqrt{N}} \sum_{\boldsymbol{t}_m} e^{i\boldsymbol{k}\cdot\boldsymbol{t}_m} \phi(\boldsymbol{r} - \boldsymbol{t}_m - \boldsymbol{d}_\alpha) \qquad \alpha = A, B \tag{1.1}$$

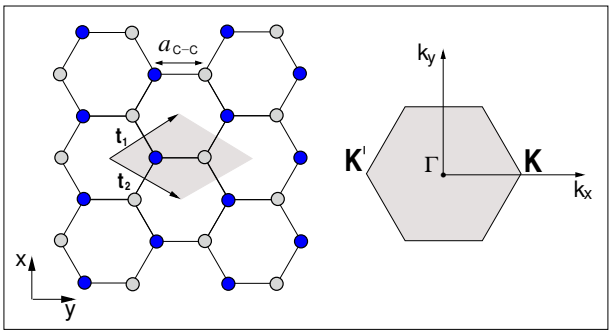

Figure 1.1: Left: structure of graphene lattice; carbon atoms represented with circles of the same color belong to the same sublattice. The shaded area represent the unit cell corresponding to the primitive lattice vectors $\boldsymbol{t}_1$ and $\boldsymbol{t}_2$. Right: depiction of the first Brillouin zone of graphene.

can be assumed as basis functions, and a crystal wave function $\Psi(\boldsymbol{k}, \boldsymbol{r})$ can be expanded as

$$\Psi(\boldsymbol{k}, \boldsymbol{r}) = \sum_{\alpha} c_{\alpha}(\boldsymbol{k}) \Phi_{\alpha}(\boldsymbol{k}, \boldsymbol{r}) \tag{1.2}$$

In Eq. (1.1) we indicated with N the number of unit cell of the crystal and with $\boldsymbol{t}_m$ the translation vectors for the hexagonal lattice, while the vectors $\boldsymbol{d}_A$ and $\boldsymbol{d}_B$ define the relative position of one of the atoms in the unit cell with respect to the other. In particular, we choose as primitive lattice vectors

$$\boldsymbol{t}_1 = \frac{a}{2} \begin{pmatrix} 1 \\ \sqrt{3} \end{pmatrix} \qquad \boldsymbol{t}_2 = \frac{a}{2} \begin{pmatrix} -1 \\ \sqrt{3} \end{pmatrix} , \tag{1.3}$$

where $a = \sqrt{3} a_{C-C}$ is the graphene lattice constant and $a_{C-C} \approx 0.142$ nm is the distance between nearest-neighhbor atoms. Thus $\boldsymbol{d}_A = 0$ and $\boldsymbol{d}_B = (a/\sqrt{3})(0, 1)$.

In this basis the Schrödinger equation is mapped into the generalized eigensystem

$$\sum_{\beta} H_{\alpha\beta} c_{\beta}(\boldsymbol{k}) = E \sum_{\beta} S_{\alpha\beta} c_{\beta}(\boldsymbol{k}) \qquad \alpha, \beta = A, B \,, \tag{1.4}$$

with the Hamiltonian matrix elements

$$\begin{aligned} H_{\alpha\beta}(\boldsymbol{k}) =& \frac{1}{N}\sum_{\boldsymbol{t}_m,\boldsymbol{t}_n} e^{i\boldsymbol{k}\cdot(\boldsymbol{t}_n-\boldsymbol{t}_m)}\langle\phi_\alpha(\boldsymbol{r}-\boldsymbol{t}_m-\boldsymbol{d}_\alpha)|H|\phi_\beta(\boldsymbol{r}-\boldsymbol{t}_m-\boldsymbol{d}_\beta)\rangle = \\ & \sum_{\boldsymbol{t}_n} e^{i\boldsymbol{k}\cdot\boldsymbol{t}_n}\langle\phi_\alpha(\boldsymbol{r}-\boldsymbol{d}_\alpha)|H|\phi_\beta(\boldsymbol{r}-\boldsymbol{t}_n-\boldsymbol{d}_\beta)\rangle\,. \end{aligned} \tag{1.5}$$

To simplify the calculations, the lattice potential can be approximated as a superposition of the potentials $U_a(\boldsymbol{r}-\boldsymbol{t}_n-\boldsymbol{d}_\alpha)$ pertaining to the isolated atoms and the overlaps of orbitals localized on different atoms can be neglected with respect to the expectation value of the energy for electrons in a $2p_z$ orbital (onsite energy). Assuming the atomic orbitals to be normalized we find, thus,

$$\begin{aligned} & \sum_{\boldsymbol{t}_n} e^{i\boldsymbol{k}\cdot\boldsymbol{t}_n}\langle\phi_\alpha(\boldsymbol{r}-\boldsymbol{d}_\alpha)|H|\phi_\beta(\boldsymbol{r}-\boldsymbol{t}_n-\boldsymbol{d}_\beta)\rangle \approx \\ & \epsilon_{2p}\delta_{\alpha\beta} + \sum_{\boldsymbol{t}_n} e^{i\boldsymbol{k}\cdot\boldsymbol{t}_n}\int d\boldsymbol{r}\phi^*_\alpha(\boldsymbol{r}-\boldsymbol{d}_\alpha)U'\phi^*_\beta(\boldsymbol{r}-\boldsymbol{t}_n-\boldsymbol{d}_\beta)\,, \end{aligned} \tag{1.6}$$

with

$$U' = \left(\sum_{\alpha,t_n} U_a(\boldsymbol{r}-\boldsymbol{t}_n-\boldsymbol{d}_\alpha)\right) - U(\boldsymbol{r}-\boldsymbol{d}_A) - U(\boldsymbol{r}-\boldsymbol{d}_B)\,;$$

$\epsilon_{2p} \simeq 8.97eV$ indicates the onsite energy. Finally, we assume

$$\begin{aligned} & \sum_{\boldsymbol{t}_n} e^{i\boldsymbol{k}\cdot\boldsymbol{t}_n}\int d\boldsymbol{r}\phi^*_\alpha(\boldsymbol{r}-\boldsymbol{d}_\alpha)U'\phi^*_\beta(\boldsymbol{r}-\boldsymbol{t}_n-\boldsymbol{d}_\beta) \approx \\ & \sum_{\langle\boldsymbol{t}_n\rangle} e^{i\boldsymbol{k}\cdot\boldsymbol{t}_n}\int d\boldsymbol{r}\phi^*_\alpha(\boldsymbol{r}-\boldsymbol{d}_\alpha)U'\phi^*_\beta(\boldsymbol{r}-\boldsymbol{t}_n-\boldsymbol{d}_\beta) = \\ & \gamma_0\sum_{\langle\boldsymbol{t}_n\rangle} e^{i\boldsymbol{k}\cdot\boldsymbol{t}_n} = \gamma_0 f(\boldsymbol{k}) \end{aligned} \tag{1.7}$$

where the angular parentheses in the subscript $\langle\boldsymbol{t}_n\rangle$ indicate that the sum is now extended only to the nearest-neighbor atoms, γ_0 is the value of the hopping integral between the $2p_z$ orbitals of nearest-neighbor atoms, and $f(\boldsymbol{k})$ reads, in the chosen reference frame,

$$f(\boldsymbol{k}) = 1 + 2\cos(\frac{k_x a}{2})\exp(-i\frac{\sqrt{3}k_y a}{2})\,. \tag{1.8}$$

We obtain

$$\begin{aligned} H_{AA} &= H_{BB} = \epsilon_{2p} \\ H_{AB} &= H^*_{BA} = \gamma_0 f(\boldsymbol{k})\,. \end{aligned} \tag{1.9}$$

Similarly, the overlap matrix elements can be written $S_{AA} = S_{BB} = 1$ (as a consequence of the normalization of the atomic wave functions), and $S_{AB} = S_{BA} = s_0 f(\boldsymbol{k})$, with $s_0 = \langle \phi(\boldsymbol{r} - \boldsymbol{d}_A) | \phi(\boldsymbol{r} - \boldsymbol{d}_B) \rangle$.
The eigenvalues of the generalized eigensystem (1.4) are

$$E^{\pm}(\boldsymbol{k}) = \frac{\epsilon_{2p} \mp \gamma_0 \sqrt{f(\boldsymbol{k})}}{1 \mp s_0 \sqrt{f(\boldsymbol{k})}}\,.$$

The value of the parameters ϵ_{2p}, γ_0 and s_0 is usually estimated by fitting the data obtained experimentally or by first-principles computations. Since $s_0 < 0.1$ eV, the approximation $s_0 \approx 0$ is often made, so that the bands $E^+(\boldsymbol{k})$ and $E^-(\boldsymbol{k})$ become symmetric with respect to ϵ_{2p}. In Fig. 1.2 the bands are plotted within the first Brillouin zone, assuming $\gamma_0 \approx 2.7$ eV and setting ϵ_{2p} as the energy reference.

1.2 The envelope function approximation

In the presence of an external potential breaking the periodicity of the crystal structure, Bloch states with different $\boldsymbol{k}$ can be mixed; as a consequence a continuum of Bloch sums has to be considered in order to expand an eigenfunction Ψ of the Hamiltonian:

$$\Psi(\boldsymbol{r}) = \int d\boldsymbol{k}\, \hat{\psi}_A(\boldsymbol{k}) \Phi_A(\boldsymbol{k}, \boldsymbol{r}) + \hat{\psi}_B(\boldsymbol{k}) \Phi_B(\boldsymbol{k}, \boldsymbol{r})\,. \tag{1.10}$$

For the Bloch sums we assume the orthonormality conditions

$$\int d\boldsymbol{r}\, \Phi^*_\beta(\boldsymbol{r}, \boldsymbol{k}')\, \Phi_\alpha(\boldsymbol{r}, \boldsymbol{k}') = \delta_{\alpha\beta}\, \delta(\boldsymbol{k} - \boldsymbol{k}')\,. \tag{1.11}$$

Let us consider the Schrödinger equation for the crystal in the presence of an external potential $U_{ext}(\boldsymbol{r})$,

$$\left[H^{(0)} + U_{ext}(\boldsymbol{r}) \right] \Psi(\boldsymbol{r}) = E \Psi(\boldsymbol{r})\,, \tag{1.12}$$

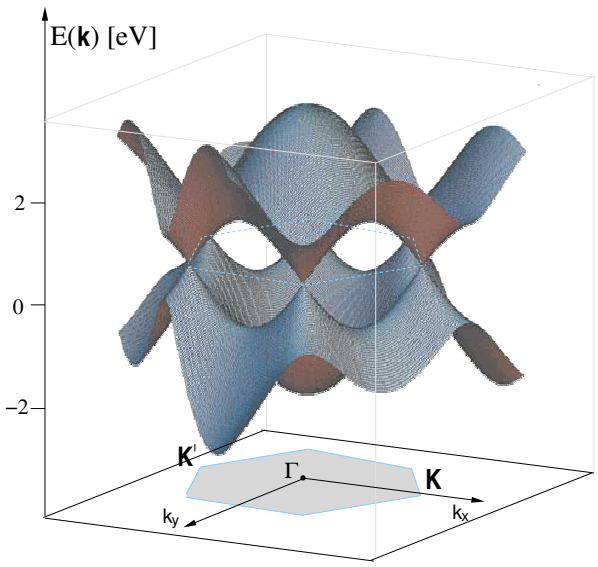

Figure 1.2: Band structure of graphene as obtained within the considered nearest-neighbor tight-binding approximation.

where $H^{(0)} = -(\hbar^2/2m)\nabla(\boldsymbol{r}) + U(\boldsymbol{r})$ denotes the Hamiltonian of the unperturbed periodic crystal ($U(\boldsymbol{r})$ is the periodic lattice potential). By substituting in Eq. (1.12) the expansion (1.10), we obtain

$$\sum_{\alpha=A,B} \int d\boldsymbol{k}\, \hat{\psi}_\alpha(\boldsymbol{k}) H^{(0)} \Phi_\alpha(\boldsymbol{k},\boldsymbol{r}) + \int d\boldsymbol{k}\, \hat{\psi}_\alpha(\boldsymbol{k}) U_{ext}(\boldsymbol{r}) \Phi_\alpha(\boldsymbol{k},\boldsymbol{r}) = E \sum_{\alpha=A,B} \int d\boldsymbol{k}\, \hat{\psi}_\alpha(\boldsymbol{k}) \Phi_\alpha(\boldsymbol{k},\boldsymbol{r})\,. \tag{1.13}$$

Let us now project this equation onto the Bloch states $\Phi_\beta(\boldsymbol{k}', \boldsymbol{r})$, $\beta = A, B$. For the first term on the left-hand side we have:

$$\begin{aligned}
&\sum_{\alpha=A,B} \langle \Phi_\beta(\boldsymbol{k}', \boldsymbol{r})| \int d\boldsymbol{k}\, \hat{\psi}_\alpha(\boldsymbol{k}) H^{(0)} \Phi_\alpha(\boldsymbol{k}, \boldsymbol{r})\rangle = \\
&\sum_{\alpha=A,B} \int d\boldsymbol{k}\, \hat{\psi}_\alpha(\boldsymbol{k}) \langle \Phi_\beta(\boldsymbol{k}', \boldsymbol{r})| H^{(0)} |\Phi_\alpha(\boldsymbol{k}, \boldsymbol{r})\rangle = \\
&\sum_{\alpha=A,B} \int d\boldsymbol{k}\, \hat{\psi}_\alpha(\boldsymbol{k}) H^{(0)}_{\beta\alpha}(\boldsymbol{k}) \delta(\boldsymbol{k} - \boldsymbol{k}') = \\
&\sum_{\alpha=A,B} H_{\beta\alpha}(\boldsymbol{k}') \hat{\psi}_\alpha(\boldsymbol{k}')\,,
\end{aligned} \tag{1.14}$$

where we have used the fact that $H^{(0)}$ does not mix Bloch states associated to different values of the momentum. Keeping a nearest neighbor tight–binding approximation, the functions $H_{\beta\alpha}(\boldsymbol{k})$ coincide with those found in the previous section.
Concerning the second term on the left-hand side of Eq. (1.13), we have to evaluate

$$\sum_{\alpha=A,B} \int d\boldsymbol{k}\, \hat{\psi}_\alpha(\boldsymbol{k}) \langle \Phi_\beta(\boldsymbol{k}', \boldsymbol{r})| U_{ext}(\boldsymbol{r}) |\Phi_\alpha(\boldsymbol{k}, \boldsymbol{r})\rangle\,. \tag{1.15}$$

In order to introduce some approximations for the potential we can rewrite the Bloch wavefunctions as

$$\Phi_\alpha(\boldsymbol{k}, \boldsymbol{r}) = e^{i\boldsymbol{k}\cdot\boldsymbol{r}} \frac{1}{\sqrt{N}} \sum_{\boldsymbol{t}_m} e^{i\boldsymbol{k}\cdot(\boldsymbol{t}_m - \boldsymbol{r})} \phi(\boldsymbol{r} - \boldsymbol{d}_\alpha) = e^{i\boldsymbol{k}\cdot\boldsymbol{r}} u_\alpha(\boldsymbol{k}, \boldsymbol{r})\,, \tag{1.16}$$

where u_α is periodic in $\boldsymbol{r}$ with the lattice periodicity. With this assumption we can write:

$$\begin{aligned}
\langle \Phi_\beta(\boldsymbol{k}', \boldsymbol{r})| U_{ext}(\boldsymbol{r}) |\Phi_\alpha(\boldsymbol{k}, \boldsymbol{r})\rangle = &\int d\boldsymbol{r}\, e^{-i(\boldsymbol{k}' - \boldsymbol{k})\cdot\boldsymbol{r}} u^*_\beta(\boldsymbol{k}', \boldsymbol{r}) u_\alpha(\boldsymbol{k}, \boldsymbol{r}) U_{ext}(\boldsymbol{r}) = \\
&\sum_{\boldsymbol{g}_m} c_m(\boldsymbol{k}, \boldsymbol{k}', \alpha, \beta) \int d\boldsymbol{r}\, e^{-i(\boldsymbol{k}' - \boldsymbol{k} - \boldsymbol{g}_m)\cdot\boldsymbol{r}} U_{ext}(\boldsymbol{r}) = \\
&\sum_{\boldsymbol{g}_m} c_m(\boldsymbol{k}, \boldsymbol{k}', \alpha, \beta) \hat{U}(\boldsymbol{k} - \boldsymbol{k}' + \boldsymbol{g}_m)\,,
\end{aligned} \tag{1.17}$$

where we have expanded the periodic functions $u^*_\beta(\boldsymbol{k}', \boldsymbol{r})u_\alpha(\boldsymbol{k}, \boldsymbol{r})$ in Fourier series as

$$u^*_\beta(\boldsymbol{k}', \boldsymbol{r})u_\alpha(\boldsymbol{k}, \boldsymbol{r}) = \sum_{\boldsymbol{g}_m} c_m(\boldsymbol{k}, \boldsymbol{k}', \alpha, \beta)e^{i\boldsymbol{g}_m \cdot \boldsymbol{r}} \tag{1.18}$$

(the sum is extended over all the reciprocal lattice vectors $\boldsymbol{g}_m$), and we have denoted with $\hat{U}(\boldsymbol{k})$ the Fourier transform of $U_{ext}(\boldsymbol{r})$.
We now suppose that the potential slowly varies over a length scale of the order of the lattice constant, so that $\hat{U}(\boldsymbol{g}_m) \approx 0$, for all the $\boldsymbol{g}_m$s. In this hypothesis the off-diagonal matrix elements $\langle \Phi_\alpha | U_{ext} | \Phi_\beta \rangle$, $\alpha \neq \beta$, are vanishing, because the potential cannot significantly mix Bloch functions associated to different sublattices. Moreover, from Eq. (1.17),

$$\begin{aligned} &\langle \Phi_\alpha(\boldsymbol{k}', \boldsymbol{r}) | U_{ext}(\boldsymbol{r}) | \Phi_\alpha(\boldsymbol{k}, \boldsymbol{r}) \rangle \approx c_0(\boldsymbol{k}', \boldsymbol{k}, \alpha, \alpha)\hat{U}(\boldsymbol{k} - \boldsymbol{k}') = \\ &\left(\frac{1}{\Omega} \int_\Omega d\boldsymbol{r}\, u^*_\alpha(\boldsymbol{k}, \boldsymbol{r})u_\alpha(\boldsymbol{k}', \boldsymbol{r}) \right) \hat{U}(\boldsymbol{k} - \boldsymbol{k}') \approx \frac{\hat{U}(\boldsymbol{k} - \boldsymbol{k}')}{(2\pi)^2}\,, \end{aligned} \tag{1.19}$$

where Ω is the area of the unit cell of the graphene lattice; the last passage is justified by the normalization chosen for the Bloch sum and by the condition $\boldsymbol{k} \approx \boldsymbol{k}'$.
Concerning the right-hand side, because of Eq. (1.11), the projections give simply

$$\sum_{\alpha = A,B} \langle \Phi_\beta(\boldsymbol{k}', \boldsymbol{r}) | \int d\boldsymbol{k}\, \hat{\psi}_\alpha(\boldsymbol{k}) \Phi_\alpha(\boldsymbol{k}, \boldsymbol{r}) \rangle = \hat{\psi}_\beta(\boldsymbol{k}'). \tag{1.20}$$

In the basis of the $\Phi_\alpha(\boldsymbol{r}, \boldsymbol{k})$, we arrive, thus, to the following form for Eq. (1.12)

$$\begin{aligned} &\begin{pmatrix} 0 & f(\boldsymbol{k}) \\ f^*(\boldsymbol{k}) & 0 \end{pmatrix} \begin{pmatrix} \hat{\psi}_A(\boldsymbol{k}) \\ \hat{\psi}_B(\boldsymbol{k}) \end{pmatrix} + \\ &\frac{1}{(2\pi)^2} \begin{pmatrix} \int d\boldsymbol{k}'\, \hat{U}(\boldsymbol{k} - \boldsymbol{k}')\hat{\psi}_A(\boldsymbol{k}') & 0 \\ 0 & \int d\boldsymbol{k}'\, \hat{U}(\boldsymbol{k} - \boldsymbol{k}')\hat{\psi}_B(\boldsymbol{k}') \end{pmatrix} = E \begin{pmatrix} \hat{\psi}_A(\boldsymbol{k}) \\ \hat{\psi}_B(\boldsymbol{k}) \end{pmatrix}. \end{aligned} \tag{1.21}$$

We introduce now another approximation. Since we are intersted in the transport properties, we restrict ourselves to the low energy regions of the band, limiting the integration domain in the left side of Eq. (1.21) to the neighboroods of the two inequivalent Dirac points $\boldsymbol{K} = (4\pi/3a)(1, 0)$ and $\boldsymbol{K}' = (4\pi/3a)(-1, 0)$. Since the distance between the Dirac points is of the order of the inverse of

the lattice spacing, the supposed smoothness of the external potential make it possible to neglect the mixing between states near different Dirac points. This entails that the integrals $\int d\boldsymbol{k}' U(\boldsymbol{k}-\boldsymbol{k}')\hat{\psi}_\alpha(\boldsymbol{k}')$ do not couple the components of $\hat{\psi}_\alpha$ close to $\boldsymbol{K}$ with those close to $\boldsymbol{K}'$, so that Eq. (1.21) can be split into two independent equations, one pertaining to a small neighborood of the $\boldsymbol{K}$ Dirac point, the other to a small neighborood of $\boldsymbol{K}'$.
In order to perform the described approximation it is convenient to define

$$\hat{F}_A^{\boldsymbol{K}}(\boldsymbol{\kappa}) = \frac{\hat{\psi}_A(\boldsymbol{K}+\boldsymbol{\kappa})}{\sqrt{N}}\,, \quad \hat{F}_B^{\boldsymbol{K}}(\boldsymbol{\kappa}) = \frac{\hat{\psi}_B(\boldsymbol{K}+\boldsymbol{\kappa})}{\sqrt{N}} \tag{1.22}$$

and

$$\hat{F}_A^{\boldsymbol{K}'}(\boldsymbol{\kappa}) = -\frac{\hat{\psi}_A(\boldsymbol{K}'+\boldsymbol{\kappa})}{\sqrt{N}}\,, \quad \hat{F}_B^{\boldsymbol{K}'}(\boldsymbol{\kappa}) = \frac{\hat{\psi}_B(\boldsymbol{K}'+\boldsymbol{\kappa})}{\sqrt{N}} \tag{1.23}$$

where $\boldsymbol{\kappa} = \boldsymbol{k} - \boldsymbol{K}$ for Eqs. (1.22) and $\boldsymbol{\kappa} = \boldsymbol{k} - \boldsymbol{K}'$ for Eqs. (1.22). Let us first consider the equation for the Dirac point $\boldsymbol{K}$, rewritten in terms of the $\hat{F}_\alpha^{\boldsymbol{K}}(\boldsymbol{\kappa})$:

$$\begin{pmatrix} 0 & f(\boldsymbol{K}+\boldsymbol{\kappa}) \\ f^*(\boldsymbol{K}+\boldsymbol{\kappa}) & 0 \end{pmatrix} \begin{pmatrix} \hat{F}_A^{\boldsymbol{K}}(\boldsymbol{\kappa}) \\ \hat{F}_B^{\boldsymbol{K}}(\boldsymbol{\kappa}) \end{pmatrix} + \\ \frac{1}{(2\pi)^2} \begin{pmatrix} \int d\boldsymbol{\kappa}' \hat{U}(\boldsymbol{\kappa}-\boldsymbol{\kappa}')\hat{F}_A^{\boldsymbol{K}}(\boldsymbol{\kappa}') & 0 \\ 0 & \int d\boldsymbol{\kappa}' \hat{U}(\boldsymbol{\kappa}-\boldsymbol{\kappa}')\hat{F}_B^{\boldsymbol{K}}(\boldsymbol{\kappa}') \end{pmatrix} = E \begin{pmatrix} \hat{F}_A^{(\boldsymbol{K})}(\boldsymbol{\kappa}) \\ \hat{F}_B^{(\boldsymbol{K})}(\boldsymbol{\kappa}) \end{pmatrix}. \tag{1.24}$$

Since we are concerned only with a small neighborhood around $\boldsymbol{K}$ we may develop the function $f(\boldsymbol{k})$ to the first order in $\boldsymbol{\kappa}$, obtaining

$$\begin{pmatrix} 0 & f(\boldsymbol{K}+\boldsymbol{\kappa}) \\ f^*(\boldsymbol{K}+\boldsymbol{\kappa}) & 0 \end{pmatrix} \approx \hbar v_F \begin{pmatrix} 0 & \kappa_x - i\kappa_y \\ \kappa_x + i\kappa_y & 0 \end{pmatrix}, \tag{1.25}$$

where $\hbar$ is the reduced Plank constant and $v_F = \sqrt{3}a\gamma_0/(2\hbar)$ is the Fermi velocity in graphene. This corresponds to considering a $\boldsymbol{k}\cdot\boldsymbol{p}$ approximation for the band structure of graphene.
With these approximations, by taking the inverse Fourier transform of Eq. (1.24), we obtain

$$\Big[-i\hbar v_F \nabla\cdot\boldsymbol{\sigma} + U_{ext}(\boldsymbol{r})I \Big] \begin{pmatrix} F_A^{\boldsymbol{K}}(\boldsymbol{r}) \\ F_B^{\boldsymbol{K}}(\boldsymbol{r}) \end{pmatrix} = E \begin{pmatrix} F_A^{\boldsymbol{K}}(\boldsymbol{r}) \\ F_B^{\boldsymbol{K}}(\boldsymbol{r}) \end{pmatrix}, \tag{1.26}$$

where $\boldsymbol{\sigma} = (\sigma_x, \sigma_y)$, σ_x and σ_y denoting the Pauli matrices, I is the 2×2 identity matrix, and we have introduced the *envelope functions* $F_\alpha^{\boldsymbol{K}}(\boldsymbol{r})$, $\alpha = A, B$, as the inverse Fourier transform of the functions $\hat{F}_\alpha^{\boldsymbol{K}}(\boldsymbol{\kappa})$.
With analogous steps it can be obtained the equation for the envelope functions around the Dirac point $\boldsymbol{K}'$:

$$\Big[-i\hbar v_F \nabla \cdot \boldsymbol{\sigma}^* + U_{ext}(\boldsymbol{r}) I \Big] \begin{pmatrix} F_A^{\boldsymbol{K}'}(\boldsymbol{r}) \\ F_B^{\boldsymbol{K}'}(\boldsymbol{r}) \end{pmatrix} = E \begin{pmatrix} F_A^{\boldsymbol{K}'}(\boldsymbol{r}) \\ F_B^{\boldsymbol{K}'}(\boldsymbol{r}) \end{pmatrix} . \tag{1.27}$$

The equations obtained are formally analogous to the two-dimensional Dirac equation describing massless relativistic particles. The spin degree of freedom for the Dirac equation is replaced in graphene by the presence of the two projections of the wave function on the sublattices A and B. The corresponding dispersion relationship, symmetric with respect to $E = 0$, is linear, resembling that of photons, with the role of the velocity of light played by the Fermi velocity. This can be easily shown by rewriting the effective Hamiltonian in Eq. (1.25) as

$$\hbar v_F \begin{pmatrix} 0 & \kappa_x - i\kappa_y \\ \kappa_x + i\kappa_y & 0 \end{pmatrix} = \hbar v_F |\boldsymbol{\kappa}| \begin{pmatrix} 0 & e^{-i\theta(\boldsymbol{\kappa})} \\ e^{i\theta(\boldsymbol{\kappa})} & 0 \end{pmatrix} , \tag{1.28}$$

with $\theta(\boldsymbol{\kappa}) = \angle f(\boldsymbol{\kappa})$. This makes it evident that the eigenspectrum is

$$E = \pm \hbar v_F |\boldsymbol{\kappa}| . \tag{1.29}$$

Finally we give the relations linking the envelope functions to the tight-binding

wavefuntion $\varphi(\boldsymbol{r})$. From Eq. (1.10), Eqs. (1.22) and Eqs. (1.23) we can write

$$\begin{aligned}
\Psi(\boldsymbol{r}) = \sum_{\alpha=A,B} \int d\boldsymbol{\kappa} \Big(\sqrt{N} F_\alpha^{\boldsymbol{K}}(\boldsymbol{\kappa}) \Phi_\alpha(\boldsymbol{K}+\boldsymbol{\kappa}, \boldsymbol{r}) + (-1)^{1-\delta_{\alpha B}} \sqrt{N} F_\alpha^{\boldsymbol{K}'}(\boldsymbol{\kappa}) \times \\
\Phi_\alpha(\boldsymbol{K}'+\boldsymbol{\kappa}, \boldsymbol{r}) \Big) = \sum_\alpha \int d\boldsymbol{\kappa} \Big(F_\alpha^{\boldsymbol{K}}(\boldsymbol{\kappa}) \sum_{\boldsymbol{t}_n} e^{i(\boldsymbol{K}-\boldsymbol{\kappa})\cdot\boldsymbol{t}_n} \times \\
\phi(\boldsymbol{r}-\boldsymbol{t}_n-\boldsymbol{d}_\alpha) + (-1)^{1-\delta_{\alpha B}} F_\alpha^{\boldsymbol{K}'}(\boldsymbol{\kappa}) \sum_{\boldsymbol{t}_n} e^{i(\boldsymbol{K}'-\boldsymbol{\kappa})\cdot\boldsymbol{t}_n} \times \\
\phi(\boldsymbol{r}-\boldsymbol{t}_n-\boldsymbol{d}_\alpha) \Big) = \sum_{\alpha,\boldsymbol{t}_n} \Big(e^{i\boldsymbol{K}\cdot\boldsymbol{t}_n} \int d\boldsymbol{\kappa}\, \hat{F}_\alpha^{\boldsymbol{K}}(\boldsymbol{\kappa}) e^{-i\boldsymbol{\kappa}\cdot\boldsymbol{t}_n} + \\
(-1)^{1-\delta_{\alpha B}} e^{i\boldsymbol{K}'\cdot\boldsymbol{t}_n} \int d\boldsymbol{\kappa}\, \hat{F}_\alpha^{\boldsymbol{K}'}(\boldsymbol{\kappa}) e^{-i\boldsymbol{\kappa}\cdot\boldsymbol{t}_n} \Big) \phi(\boldsymbol{r}-\boldsymbol{t}_n-\boldsymbol{d}_\alpha) = \\
\sum_{\alpha,\boldsymbol{t}_n} \Big(e^{i\boldsymbol{K}\cdot\boldsymbol{t}_n} F_\alpha^{\boldsymbol{K}}(\boldsymbol{t}_n) + (-1)^{1-\delta_{\alpha B}} e^{i\boldsymbol{K}'\cdot\boldsymbol{t}_n} F_\alpha^{\boldsymbol{K}'}(\boldsymbol{t}_n) \Big) \times \\
\phi(\boldsymbol{r}-\boldsymbol{t}_n-\boldsymbol{d}_\alpha)
\end{aligned} \tag{1.30}$$

We can thus write $\Psi(\boldsymbol{r})$ as

$$\Psi(\boldsymbol{r}) = \sum_{\alpha,\boldsymbol{t}_n} \psi_\alpha(\boldsymbol{t}_n) \phi(\boldsymbol{r}-\boldsymbol{t}_n-\boldsymbol{d}_\alpha)\,, \tag{1.31}$$

with

$$\psi_\alpha(\boldsymbol{t}_n) = e^{i\boldsymbol{K}\cdot\boldsymbol{t}_n} F_\alpha^{\boldsymbol{K}}(\boldsymbol{t}_n) + (-1)^{1-\delta_{\alpha B}} e^{i\boldsymbol{K}'\cdot\boldsymbol{t}_n} F_\alpha^{\boldsymbol{K}'}(\boldsymbol{t}_n)\,. \tag{1.32}$$

In the following we disregard the atomic details of the functions ψ_αs, referring to the continuous form

$$\psi_\alpha(\boldsymbol{r}) = e^{i\boldsymbol{K}\cdot\boldsymbol{r}} F_\alpha^{\boldsymbol{K}}(\boldsymbol{r}) + (-1)^{1-\delta_{\alpha B}} e^{i\boldsymbol{K}'\cdot\boldsymbol{r}} F_\alpha^{\boldsymbol{K}'}(\boldsymbol{r})\,, \tag{1.33}$$

as it is customary in the framework of the envelope function approximation.

1.3 Armchair graphene nanoribbons

A graphene nanoribbon is a strip of graphene, that can be obtained by cutting a graphene sheet along a determinate direction. In this way a lateral confinement is introduced. The direction of the confinement with respect to the graphene

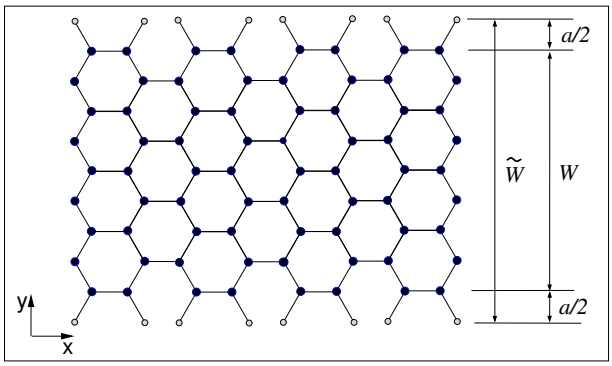

Figure 1.3: Depiction of an armchair nanoribbon with 9 dimer lines. The gray circles at the top and bottom edge represent passivation atoms.

lattice determines the characteristics of the nanoribbon edges, that can strongly affect its transport properties. Here we treat only graphene nanoribbons with perfect armchair edges, that can be thought of as obtained cutting the graphene sheet along the direction of the nearest-neighbor carbon bonds (see Fig. 1.3). Unless explicitly remarked, in the following we refer to a generical armchair nanoribbon with N_D dimer lines of carbon atoms across its width, so that the distance between the opposite (confining) edges is $W = (N_D - 1)\, a/2$. For the sake of convenience we will use a reference frame in which the Dirac points have only a nonzero component along the confinement direction (y) of the ribbon: $\boldsymbol{K} = -K\hat{y}$ and $\boldsymbol{K'} = K\hat{y}$, with $K = 4\pi/(3a)$. In order to obtain in this new reference frame the same form for Eq. (1.26) and Eq. (1.27) we have to introduce suitable phase factors into Eq. (1.22) and Eq. (1.23). For our purposes, it is sufficient to take into account that Eq. (1.33) now become

$$\begin{cases} \psi_A(\boldsymbol{r}) = e^{i\boldsymbol{K}\cdot\boldsymbol{r}} F_A^{\boldsymbol{K}}(\boldsymbol{r}) - i e^{i\boldsymbol{K'}\cdot\boldsymbol{r}} F_A^{\boldsymbol{K'}}(\boldsymbol{r}) \\ i\psi_A(\boldsymbol{r}) = e^{i\boldsymbol{K}\cdot\boldsymbol{r}} F_A^{\boldsymbol{K}}(\boldsymbol{r}) + e^{i\boldsymbol{K'}\cdot\boldsymbol{r}} F_A^{\boldsymbol{K'}}(\boldsymbol{r}) \end{cases} . \tag{1.34}$$

We position the origin of the y-axis on one of the two dimer lines of passivating hydrogen atoms just outside the ribbon, assumed at a distance $a/2$ from the ribbon edges (we neglect edge relaxation). These constitute the effective

boundaries of the ribbon, along which the wave function vanishes. For what has been said, they are identified by the conditions $y = 0$ and $y = \tilde{W} \equiv W + a$. Within the envelope function approximation, an AGNR is still described by Eq. (1.26) and Eq. (1.27), provided that the lateral confinement is accounted for by means of appropriate boundary conditions. In the armchair case each boundary contains atoms belonging to both the A and the B sublattice. Due to the strong spatial localization of the $2p_z$ atomic orbitals, from Eq. (1.31) we deduce that the vanishing of the overall wave function Ψ along the boundaries entails vanishing of both the ψ_A and ψ_B functions. We restrict now to the case in which the potential energy U depends only on the transverse coordinate y, so that the longitudinal component of the momentum is constant; we will denote the longitudinal wave vector by κ_x. The envelope functions that are solution of the Dirac equations (1.26) and (1.27) can be factored into a product of a propagating wave along x and a confined component in the transverse direction:

$$F_\beta^{\boldsymbol{K}^{(\prime)}}(\boldsymbol{r}) = e^{i\kappa_x x}\Phi_\beta^{\boldsymbol{K}^{(\prime)}}(y) \tag{1.35}$$

($\alpha = A, B$). The functions $\Phi_\beta^{\vec{\alpha}}$ satisfy (see Eq. (1.26) and Eq. (1.27))

$$\begin{cases} \left(\sigma_x f(y) + \sigma_z \dfrac{d}{dy}\right)\vec{\varphi}^{\boldsymbol{K}}(y) = -\kappa_x \vec{\varphi}^{\boldsymbol{K}}(y) \\ \left(\sigma_x f(y) - \sigma_z \dfrac{d}{dy}\right)\vec{\varphi}^{\boldsymbol{K}'}(y) = -\kappa_x \vec{\varphi}^{\boldsymbol{K}'}(y) \end{cases}, \tag{1.36}$$

where we have introduced the shorthands

$$\vec{\varphi}^{\boldsymbol{K}}(y) = \begin{bmatrix} \Phi_A^{\boldsymbol{K}}(y) \\ \Phi_B^{\boldsymbol{K}}(y) \end{bmatrix}, \qquad \vec{\varphi}^{\boldsymbol{K}'}(y) = \begin{bmatrix} i\,\Phi_A^{\boldsymbol{K}'}(y) \\ i\,\Phi_B^{\boldsymbol{K}'}(y) \end{bmatrix}, \tag{1.37}$$

and $f(y) = (U(y) - E)/\gamma$.
The boundary conditions are written

$$\begin{cases} \vec{\varphi}^{\boldsymbol{K}}(0) = \vec{\varphi}^{\boldsymbol{K}'}(0) \\ \vec{\varphi}^{\boldsymbol{K}}(\tilde{W}) = e^{2iK\tilde{W}}\vec{\varphi}^{\boldsymbol{K}'}(\tilde{W}) \end{cases}, \tag{1.38}$$

We see that while in unconfined graphene the envelope functions associated to different Dirac points decouple, in AGNR they are in fact mixed by the boundary conditions (1.38).

In the presence of a generic external electric field the problem cannot be solved analytically and it is necessary to rely on numerical methods in order to obtain approximate expressions for the transverse components Φ of the envelope functions and the corresponding longitudinal wave vectors κ_x.

1.4 Discretization methods in the direct space

In this section, we set up the numerical problem using finite difference techniques.

We consider as unknowns, together with the longitudinal wave vectors κ_x, the value of the functions Φ's on a uniform grid of N_y points along the effective width $\tilde{W}$ of the ribbon: $y_i = (i-1)\Delta_y$, with $\Delta_y = \tilde{W}/(N_y - 1)$ and $i = 1, \ldots, N_y$. The derivatives are expressed as linear combinations of the values of the Φ's on a finite number of grid points, and the boundary conditions, relating the values of the Φ's at the edges of the ribbon, are exploited to reduce the number of unknowns.

In this way the system of equations (1.36) is mapped onto an eigenvalue problem $A\,\vec{v} = -\kappa_x\,\vec{v}$, where the elements of the vector $\vec{v}$ are the values of the Φ's at the grid points and the eigenvalues give the longitudinal wave vectors κ_x.

In general, as Δ_y approaches zero, a subset of eigenvectors of A (together with their respective eigenvalues) converge to the solutions of Eq. (1.36). The remaining eigenvectors have no meaningful continuum limit. We will refer to them as spurious solutions.

The discretization scheme that we decide to adopt can affect both the numerical efficiency and the appearance of spurious solutions. In particular, two aspects must be taken into account: boundary conditions and the fermion doubling problem. We now discuss the implications of the simplest discretization schemes:

(a) naive asymmetric discretization

(b) naive symmetric discretization

(c) improved symmetric discretization.

In the scheme (a) we evaluated the first differential equation of (1.36) at the points y_i with $i = 1, \ldots, N_y - 1$ and the second differential equation of (1.36) at y_i with $i = 2, \ldots, N_y$. In addition, we used different representations for the derivatives: in the first equation we used the two-point forward discretization formula $(d\Phi/dy)|_{y_i} \simeq (\Phi(y_{i+1}) - \Phi(y_i))/\Delta_y$ and in the second one the two-point backward discretization $(d\Phi/dy)|_{y_i} \simeq (\Phi(y_i) - \Phi(y_{i-1}))/\Delta_y$. We enforced the boundary conditions by substituting, wherever the discretization of the derivatives requires the values of $\vec{\varphi}^{\boldsymbol{K}'}(y_1)$ and $\vec{\varphi}^{\boldsymbol{K}}(y_{N_y})$, their expression (1.38) as a function of $\vec{\varphi}^{\boldsymbol{K}}(y_1)$ and $\vec{\varphi}^{\boldsymbol{K}'}(y_j)$. In this way, the unknowns of the discretized problem are $\vec{\varphi}^{\boldsymbol{K}}(y_i)$ for $i = 1, \ldots, N_y - 1$ and $\vec{\varphi}^{\boldsymbol{K}'}(y_j)$ for $j = 2, \ldots, N_y$. The differential equations (1.36) are thus mapped onto a $(4\,(N_y - 1)) \times (4\,(N_y - 1))$ eigenvalue problem. We also considered the alternative scheme of a symmetric discretization formula inside the ribbon and an asymmetric one at the edges. In both cases we experienced a very slow convergence to the exact solutions and also obtained a large number of spurious solutions, which persist also when higher order discretization schemes are used.

As an example, in Fig. 1.4 we show the eigenvalues κ_x obtained for a null potential energy $U(y)$ using a 5-point discretization formula, symmetric inside the ribbon and asymmetric at the edges. Since for $U(y) \equiv 0$ the problem is exactly solvable, it is known that the continuum κ_x values have to be either real or purely imaginary. The discretized problem has instead also complex solutions with nonzero real and imaginary parts. In this simple case we can identify them as spurious solutions. However, for a general potential energy $U(y)$, complex solutions can be physical [19], so that they cannot be rejected *a priori*.

In the scheme (b) the grid is modified in order to exploit a symmetric discretization scheme in every grid point. Defining $y_0 = -\Delta_y$ and $y_{N_y+1} = \tilde{W} + \Delta_y$, we replaced the original boundary conditions (1.38) with

$$\begin{cases} \vec{\varphi}^{\boldsymbol{K}}(y_0) = \vec{\varphi}^{\boldsymbol{K}'}(y_1) \\ \vec{\varphi}^{\boldsymbol{K}'}(y_0) = \vec{\varphi}^{\boldsymbol{K}}(y_1) \\ \vec{\varphi}^{\boldsymbol{K}}(y_{N_y+1}) = e^{i2K\tilde{W}}\vec{\varphi}^{\boldsymbol{K}'}(y_{N_y}) \\ \vec{\varphi}^{\boldsymbol{K}'}(y_{N_y+1}) = e^{-i2K\tilde{W}}\vec{\varphi}^{\boldsymbol{K}}(y_{N_y}) \end{cases}, \tag{1.39}$$

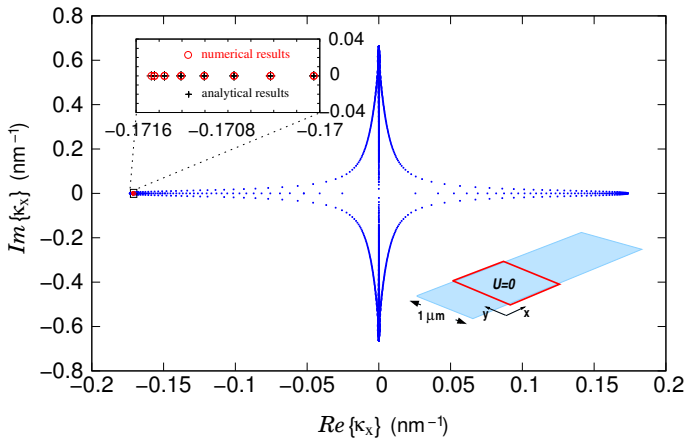

Figure 1.4: Longitudinal wave vectors obtained by solving the Dirac equation for a single transversal slice of a 1 μm wide ribbon in the absence of an external potential. The results have been obtained with a 5-point discretization formula symmetric inside the ribbon and asymmetric at the edges. Besides wave vectors that are good approximations of the analytical ones (see the inset), the presence of a large number of spurious solutions, corresponding to the points outside the axes, is apparent.

which coincide with (1.38) in the continuum limit.

We evaluated the differential equations of the system (1.36) using a symmetric 3-point discretization formula $(d\Phi/dy)|_{y_i} \simeq (\Phi(y_{i+1}) - \Phi(y_{i-1}))/(2\,\Delta_y)$ in all the points y_i of the grid ($i = 1, \ldots, N_y$), substituting the values in y_0 and y_{N_y+1}, wherever they are needed, with the relations (1.39). The differential equations are thus mapped into a $(4\,N_y) \times (4\,N_y)$ eigenvalue problem. The eigenvalues of the discretized problem turn out to be double degenerate, while the discretized eigenfunctions show an alternating sign between consecutive gridpoints. In detail, each eigenspace is the span of two vectors, let us say $\vec{v}_{(c)}$ and $\vec{v}_{(l)}$, such that the $\vec{v}_{(l)}$ components display even-odd oscillations whilst the others have oscillation frequency almost independent of N_y. The eigenvector

$\vec{v}_{(l)}$ cannot have a continuum counterpart, hence the double degeneracy is in fact a lattice artefact. This is a clear manifestation of the so-called fermion doubling problem: a "naive" direct space discretization of the Dirac equation results in the appearance of 2^d fermions (instead of the single one expected) in d space dimensions (in our case $d = 1$); this is an infrared effect, i.e. it does not disappear in the continuum limit $\Delta_y \to 0$. This is a very well known problem in the field of lattice quantum chromodynamics (see e.g [17]) and is deeply connected with the chiral anomaly (see e.g [18]), i.e. with the impossibility of regularizing a theory with fermions in a local, chiral symmetric way. In our simple case, this problem is brought on by our choise of the symmetric 3-point discretization formula for the derivative, which involves an incremental step of $2\,\Delta_y$, and hence makes odd and even grid points decoupled.

Many methods have been developed to overcome the fermion doubling problem. In the scheme (c) we employed the method proposed in Refs. [14, 15], which has quite a simple implementation and was already applied [12] (considering periodic boundary conditions) to study some transport properties of graphene ribbons. We still use a symmetric 3-point discretization formula for the derivative, but with an incremental step equal to Δ_y instead of $2\,\Delta_y$. This can be done by evaluating the differential equations on an auxiliary grid, with nodes at the centers of the cells of the original grid: $y_{i+(1/2)} = (y_i + y_{i+1})/2$, for $i = 1, \ldots, N_y - 1$. The derivative is then approximated by $(d\Phi/dy)|_{y_{i+(1/2)}} \simeq (\Phi(y_{i+1}) - \Phi(y_i))/\Delta_y$. The potential energy U is known for every value of y and can be directly evaluated at $y_{i+(1/2)}$. The value of the functions Φ at $y_{i+(1/2)}$ can be estimated by the average of the values at y_i and y_{i+1}: $\Phi(y_{i+(1/2)}) \simeq (\Phi(y_i) + \Phi(y_{i+1}))/2$.

We have considered as unknowns $\vec{\varphi}^{\boldsymbol{K}}(y_i)$ for $i = 1, \ldots, N_y - 1$ and $\vec{\varphi}^{\boldsymbol{K}'}(y_j)$ for $j = 2, \ldots, N_y$, substituting the values of $\vec{\varphi}^{\boldsymbol{K}'}(y_1)$ and $\vec{\varphi}^{\boldsymbol{K}}(y_{N_y})$ with their expression (1.38) as a function of $\vec{\varphi}^{\boldsymbol{K}}(y_1)$ and $\vec{\varphi}^{\boldsymbol{K}'}(y_j)$. The original differential equations (1.36) are thus mapped into the generalized eigenproblem $A\,\vec{v} = -\kappa_x\,B\,\vec{v}$, where A and B are $(4\,(N_y - 1)) \times (4\,(N_y - 1))$ matrices. Since the matrix B is invertible, this problem is indeed equivalent to the standard eigenproblem $(B^{-1}\,A)\,\vec{v} = -\kappa_x\,\vec{v}$.

We notice, however, that while in the previous cases the matrix of the eigensys-

tem was a sparse matrix, and thus optimized solution techniques, such as the Arnoldi method, could be used, in this case A and B are sparse matrices, but $B^{-1}\,A$ is not. In order to exploit the sparsity of A and B in a numerically optimized eigensolver, the multiplication $\vec{y} = B^{-1}\,A\vec{x}$, which is the fundamental operation in algorithms for solving eigenproblems, is performed in two steps: first the multiplication by a sparse matrix $A\vec{x}$ and then the solution of a sparse linear system $B\vec{y} = \vec{z}$ (with $\vec{z}$ the result of the previous multiplication).
In the discretization scheme (c) the problems of the previous schemes are solved: there are neither spurious eigenvalues nor unphysical double degeneracies. This method can thus effectively be employed in order to study numerically Eq. (1.36). As a matter of fact, we'll show in the next sections that it is not the most efficient way to handle to the system of differential equations (1.36).

1.5 Reformulation as a problem with periodic boundary conditions

The numerical techniques in the real domain that we described in Sec. 1.4 do not allow an efficient and accurate numerical analysis of the problem (1.36)-(1.38). Indeed, in order to obtain high precision results, very large matrices have to be diagonalized, and the size becomes soon prohibitive. Indeed, working in the reciprocal space can be advantageous. First of all, the fermion doubling problem is absent, as one could argue tracing back its origin to the periodicity of the wave function across the Brillouin zone induced by the space discretization (a simple topological argument is given in Ref. [18], §13.1).
In this section we reformulate the problem (1.36)-(1.38) as one on a different domain but with periodic boundary conditions. In the next section, then, we will set up the numerical problem in the reciprocal space.
We define the two-component function

$$\vec{\varphi}(y) = \begin{cases} \vec{\varphi}^{\boldsymbol{K}}(y) & y \in [0, \tilde{W}] \\ e^{i2K\tilde{W}}\vec{\varphi}^{\boldsymbol{K'}}(2\tilde{W} - y) & y \in [\tilde{W}, 2\tilde{W}]\,. \end{cases} \tag{1.40}$$

From the second of the boundary conditions (1.38) we see that $\vec{\varphi}$ is continuous in its whole domain, while the first condition gives

$$e^{i2K\tilde{W}}\vec{\varphi}(0) = \vec{\varphi}(2\tilde{W}) \ . \tag{1.41}$$

The differential equation satisfied by $\vec{\varphi}$ can be easily deduced from Eq. (1.36) and can be written in the compact form

$$\begin{cases} \left(\dfrac{d}{d\,y}\sigma_z + h(y)\sigma_x\right)\vec{\varphi}(y) = -\kappa_x\vec{\varphi}(y) \\ e^{-i2K\tilde{W}}\vec{\varphi}(2\tilde{W}) = \vec{\varphi}(0)\,, \end{cases} \tag{1.42}$$

where

$$h(y) = f(\tilde{W} - |\tilde{W} - y|) \qquad \forall y \in [0, 2\,\tilde{W}]\,. \tag{1.43}$$

We have halved the number of first-order differential equations by doubling the solution domain. Moreover the quasi-periodic boundary conditions in Eq. (1.42) can be interpreted as periodic boundary conditions for the function $e^{-iKy}\vec{\varphi}(y)$.

The methods described in the previous section could be also used to solve the problem (1.42). In particular, in this case it is possible, exploiting the periodic boundary condition, to directly use the symmetric discretization formula for the first derivatives, with incremental step $2\,\Delta_y$, over all the points of a uniform grid defined on the $[0, 2\,\tilde{W}]$ domain, but the solution still suffers from the fermion doubling problem. The application of the discretization scheme (c) described in the previous section instead allows to obtain the correct results, but we have not observed any efficiency gain with respect to the discretization of the original differential problem.

In appendix A we show that Eq. (1.42) can be recast in the form of a complex second order differential equation for a scalar unknown function; in that form the discretization in direct space is free from doublers. We show, moreover, that the problem Eq. (1.42) can be mapped onto an algebraic eigensystem by reformulating it in a cardinal sines basis. Also in this case no spurious solutions are present. We do not treat in detail these alternatives, focusing, instead, on the method of solution of the problem in the reciprocal space, which turns out to be more efficient.

1.6 Solution in the reciprocal space

A key feature of the discretization in the direct space (discussed in section 1.4) was the representation of the derivative. In particular, it is reasonable to expect that an n-point discretization introduces errors

$$|\vec{\varphi}'(y_\ell) - \vec{\varphi}'_{(N_y)}(y_\ell)| \gtrsim \mathcal{O}(N_y^{1-\min(\alpha,n)}) \,, \tag{1.44}$$

where $\vec{\varphi}'_{(N_y)}(y_\ell)$ is the n-point discretization of the first derivative on a grid with N_y points and α is the order of the first discontinuous derivative of the function.
In our specific case (1.42), it is enough that the first derivative of the potential is nonzero at the boundaries (i.e. the external electric field has a nonzero transverse component at the edges) for the second derivative of the eigenfunctions to be discontinuous at $y = 0, \tilde{W}$ (see Eq. (1.43)): in that case, also an increase of the number n of points used in the discretization of the derivatives does not result in an increase of the approximation of the derivatives. Thus, Eq. (1.44) is a very strong limitation.
The methods in the Fourier domain are better behaved in this respect: the direct space methods involve a global distortion of the dispersion relation, which is instead exact for frequencies lower than the cut-off in the Fourier case.
We begin by noticing that, since $h(y)$ and $e^{-iKy}\vec{\varphi}(y)$ assume the same values in 0 and $2\tilde{W}$, they can be extended by periodicity with period $2\tilde{W}$ without introducing discontinuities. However, unlike the slowly varying function $\vec{\varphi}(y)$, the function $e^{-iKy}\vec{\varphi}(y)$ exhibits high frequency components (the factor e^{-iKy} performs a shift of the spectrum of $\vec{\varphi}(y)$ around K). Since it is convenient to limit to the low frequencies the spectral content of the eigenfunctions, in the following we will replace K with $\tilde{K} = K + n_0\pi/\tilde{W}$, where $n_0 = -\lfloor K\tilde{W}/\pi \rceil$. As $e^{-i\tilde{K}y} = e^{-iKy}$, this subsitution leaves the boundary conditions unchanged, but allows to keep down to a minimum the spectral shift of the eigenfunctions with respect to $\vec{\varphi}(y)$.
We define $h_\ell \equiv h_{-\ell}$ and $\vec{a}_m$ as the Fourier coefficients of $h(y)$ and $e^{-iKy}\vec{\varphi}(y)$,

respectively:

$$\begin{aligned} h(y) &= \sum_{\ell=-\infty}^{\infty} h_\ell e^{i\pi\ell y/\tilde{W}} \\ \vec{\varphi}(y) &= \sum_{m=-\infty}^{\infty} \vec{a}_m e^{i(m\pi/\tilde{W}+\tilde{K})y}\,. \end{aligned} \tag{1.45}$$

Substituting these expressions inside the differential equation of (1.42) and then projecting onto the exponential functions $e^{i\pi(n-\eta/3)y/\tilde{W}}$, for the generical index n we obtain in the reciprocal space

$$\sum_{m=-\infty}^{+\infty} \left[i\left(\frac{n\pi}{\tilde{W}} + \tilde{K}\right)\sigma_z \delta_{n,m} + h_{n-m}\,\sigma_x \right] \vec{a}_m = -\kappa_x \vec{a}_n\,, \tag{1.46}$$

where $\delta_{n,m}$ is the Kronecker delta function. These equations are still exact and can be rewritten in the matrix form

$$M\vec{a} = -\kappa_x \vec{a} \tag{1.47}$$

where M is a structured infinite matrix whose 2×2 block is given by

$$M_{n,m} = P_n \delta_{n,m} + Q_{n,m} \tag{1.48}$$

with

$$P_n = i\left(\frac{n\pi}{\tilde{W}} + \tilde{K}\right)\sigma_z\,, \quad Q_{n,m} = h_{n-m}\,\sigma_x\,. \tag{1.49}$$

The weight of the blocks P_n (which contribute only to the diagonal of M) is marginal for small values of $|n|$, while increases for larger values of $|n|$. On the other hand, if the $h(y)$ is square integrable, the contribution of the blocks $Q_{n,m}$ vanishes for large values of $|n-m|$, i.e. sufficiently far from the diagonal of the matrix M, because of the Parseval theorem. Actually, for the regular potentials for which the envelope function approach gives reliable results, the hypothesis of square integrability of $h(y)$ is a very weak hypothesis.
If we consider a sufficiently large positive integer D such that

$$\left|\frac{\pi}{\tilde{W}}\left(\pm D\frac{\pi}{\tilde{W}}\right)\right| \gg \max_j |h_j|\,, \tag{1.50}$$

inside the matrix M we can identify 3 matrices (lying on the diagonal of M): M_L, M_0, and M_H, which contain: the blocks $M_{n,m}$ with $n, m < -D$, those with

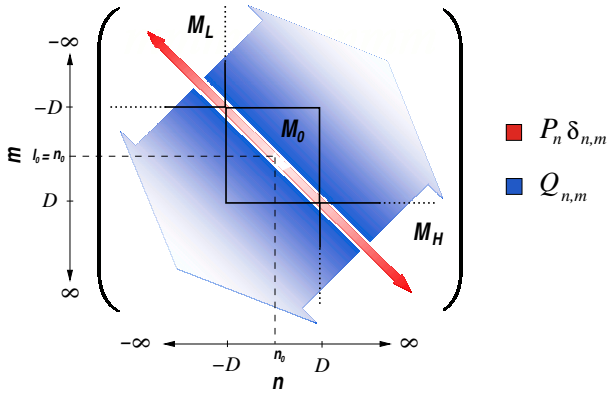

Figure 1.5: The considered partitioning of the matrix M defined in the text. The red arrows correspond to the 2×2 $P_n \delta_{n,m}$ blocks, while the blue arrows correspond to the 2×2 $Q_{n,m}$ blocks. The color of the arrows intensifies in the direction of the increase of the relative weight of the blocks they are associated to.

$-D \leq n, m \leq D$, and those with $n, m > D$, respectively. On the basis of our previous considerations, we notice that all the rest of the matrix M (including only blocks $Q_{n,m}$) is negligible with respect to these submatrices, and that M_L and M_H (where the blocks P_n dominate on the blocks $Q_{n,\ell}$) are approximately diagonal. Therefore in our numerical analysis, M can be substituted with the matrix with elements

$$\begin{aligned} \bar{M}_{n,m} = i \left(\frac{n\pi}{\tilde{W}} + \tilde{K} \right) \sigma_z \delta_{n,m} \\ + h_{n-m} \sigma_x \Theta(|n| < D) \Theta(|m| < D) \end{aligned} \tag{1.51}$$

(where $\Theta(\text{true}) = 1$ and $\Theta(\text{false}) = 0$), which contains only M_0 and the diagonals of M_L e M_H. We can treat the rest $\delta\bar{M} \equiv M - \bar{M}$ as a small perturbation and, at the lowest order, completely ignore its existence. The corrections to this approximate solution can then be worked out by the standard perturbation theory on the operator $\bar{M}$ perturbed with $\delta\bar{M}$.

At the lowest order, the matrices M_L and M_H introduce purely imaginary eigenvalues $\kappa_x = \pm\, i \left(\frac{n\pi}{\tilde{W}} + \tilde{K}\right)$ with large modulus (since in these matrices $|n|$ is large). These eigenvalues correspond to high-order evanescent modes, which are generally negligible in a transport analysis.
Therefore, once we have chosen a sufficiently large cut-off threshold D, we can limit our analysis to the matrix M_0, in which both the P_n and the $Q_{n,\ell}$ blocks have to be considered. The finite dimensional problem $(M_0 + k_x)\vec{v}_0 = 0$ is not affected by doubling. The eigenvalues of M_0 are accurate estimations of the longitudinal wave vectors κ_x. Instead, the components of the eigenvectors v_0 of M_0 are the vectors $[\vec{a}_0]_m \approx \vec{a}_m$. Form these we can reconstruct the eigenfunctions $\vec{\varphi}(y)$ as

$$\vec{\varphi}(y) \approx \vec{\varphi}_D(y) \equiv \sum_{m=-D}^{D} [\vec{a}_0]_m \, e^{i(n\pi/\tilde{W}+\tilde{K})} \,. \tag{1.52}$$

and, from (1.78) and (1.37), the transversal components Φ of the envelope functions ($\beta = A, B$)

$$\begin{aligned} \Phi_\beta^{\boldsymbol{K}}(y) &\approx \sum_{m=-D}^{D} [a_0^\beta]_m \, e^{i(n\pi/\tilde{W}+\tilde{K})} \\ \Phi_\beta^{\boldsymbol{K}'}(y) &\approx -i \sum_{m=-D}^{D} [a_0^\beta]_m \, e^{-i(n\pi/\tilde{W}+\tilde{K})} \,. \end{aligned} \tag{1.53}$$

Finally, from Eq. (1.31) and Eq. (1.35) we obtain that

$$\Psi_\beta(\vec{r}) = 2\, i \sum_{m=-D}^{D} \left[[a_0^\beta]_m \, \sin\left((m-n_0)\pi y/\tilde{W}\right)\right] e^{i\kappa_x x} \,. \tag{1.54}$$

From the numerical point of view, all these calculations can strongly benefit by the use of optimized FFT (fast Fourier transform) routines for the calculation of the Fourier series.
In Fig. 1.6 the set of wave vectors obtained for a Lorentzian-shaped transversal potential is shown. We notice the presence of wave vectors with simultaneously non-vanishing real and imaginary part, symmetrically located with respect to the real and the imaginary axis. Indeed, as we detail in Sec. 1.9, from eq. (1.42)

it may be deduced that κ_x is an eigenvalue of the system, if and only if $-\kappa_x$, κ_x^* and $-\kappa_x^*$ are eigenvalues, as well. Solutions with nonreal κ_x^2 (i.e. κ_x with nonzero real and imaginary parts) can be found in the presence of an external electric field. Their appearance is related to the existence of exceptional points, *i.e.* points in which the operator in Eq. (1.42) is not diagonalizable (this is possible since it is not self-adjoint). The existence of nonreal κ_x^2 values is a manifestation of the $\mathcal{PT}$ symmetry breaking in the system [19] (see Sec. 1.9). Moreover, we notice that, coherently with the nature of the Dirac equation, the solution of the problem includes both electron and hole states, the former being localized at the minima of the potential energy $U(y)$, the latter at the maxima. As an example of hole state we plot in Fig. 1.7 the real and imaginary part of the function $\Phi_A^{\boldsymbol{K}}$ and $\Phi_A^{\boldsymbol{K}'}$, corresponding to the largest real wave vector in Fig 1.6.

1.7 Comparison between the methods

In this section we draw a comparison of numerical efficiency between the methods introduced so far, performing a numerical analysis of the convergence rate for several test cases.
We are going to compare three main strategies:

(S). method (c) of Sec. 1.4

(S_p). method (c) of Sec. 1.4 applied to the periodic problem (1.42)

(F). the Fourier method described in Sec. 1.6

In the case (F) the coefficients h_n are computed on an extremely fine grid (by means of a FFT), independent of the dimension D of the cut-off matrix to be diagonalized.

We consider a nanoribbon composed of $N_D = 4065$ dimer lines (corresponding to an effective width $\tilde{W} \approx 500\,\mathrm{nm}$) for several electric fields, with potentials (see Fig. 1.8):

- step potential

$$U(y) = \begin{cases} 0\,\mathrm{eV} & y \leq 200\,\mathrm{nm} \\ 0.2\,\mathrm{eV} & y > 200\,\mathrm{nm} \end{cases} \tag{1.55}$$

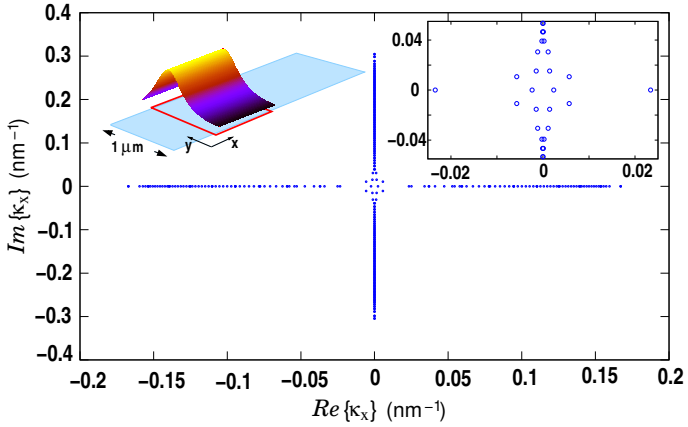

Figure 1.6: Longitudinal wave vectors obtained by solving the Dirac equation in the reciprocal space for a single transversal slice of a 1 m wide ribbon. The external potential, longitudinally constant in the considered region, is assumed to be Lorentzian–shaped with a half-width of 150 nm and a peak value of 0.2 eV. Inset: enlargement of a region around the origin of the Gauss plane; the plot highlights the presence of longitudinal wave vectors with simultaneously non-vanishing real and imaginary part.

- Lorentzian potential

$$U(y) = A\frac{\Gamma/2}{(y-y_0)^2 + (\Gamma/2)^2} \tag{1.56}$$

  with $y_0 = 200\,\text{nm}$, $\Gamma = 100\,\text{nm}$ and $A = 10\,\text{eV nm}$

- parabolic potential

$$U(y) = \bar{A}(y-\bar{y})^2 \tag{1.57}$$

  with $\bar{y} = 250\,\text{nm}$ and $\bar{A} = 0.2\,\text{eV}/(250\,\text{nm})^2$.

We set the electron injection energy at $E = 0.1\,\text{eV}$ and study the scaling of the eigenvalue precision as a function of the execution time on an Intel(R) Xeon(R) CPU E5420 2.50GHz processor. Diagonalization was performed by means of

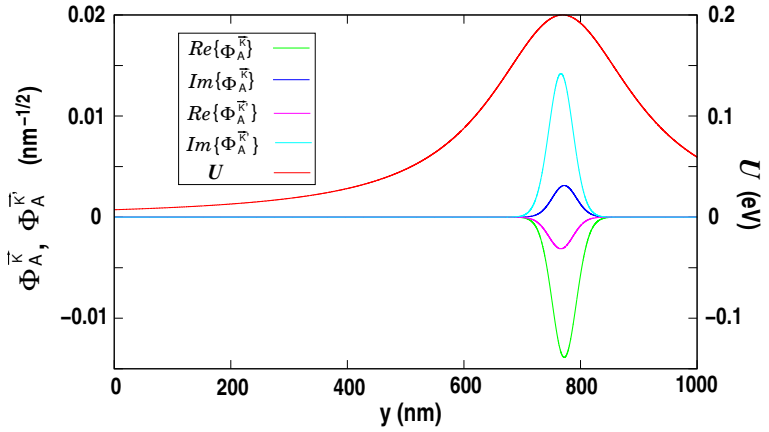

Figure 1.7: Plot of the real and imaginary part of the functions $\Phi_A^{\boldsymbol{K}}$ and $\Phi_A^{\boldsymbol{K}'}$ associated to the largest real eigenvalue in Fig. 1.6. A cross section of the external potential U is also shown.

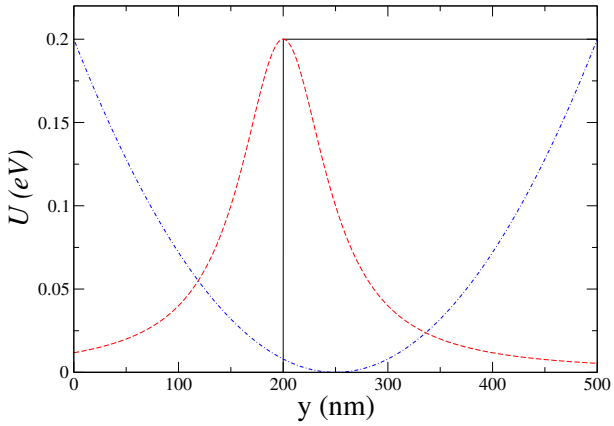

Figure 1.8: Plot of the potentials used for the evaluation of the relative efficiency of the numerical methods.

standard LAPACK routines. Figures refer to the minimum and maximum real eigenvalues; we have not found noticeable differences in the behavior of other eigenvalues. Eigenvalues corresponding to larger κ_x values converge faster to the corresponding eigenvalues of the original problem (1.42): this can be explained as a consequence of the fact that, since the total energy is constant, large κ_x values correspond to small kinetic energy in the transverse direction, *i.e.* to transversal modes with large wavelength, which are less sensitive to the discretization.
Method (S_p) is slightly more efficient than method (S), probably due to the better block structure of the discretization matrix. However, in all the cases we have studied, the Fourier methods largely outperform the direct space ones, often of several order of magnitude.
The better performance of Fourier methods with respect to direct space ones has been recently noticed also in Ref. [20], where a Schr̈odinger equation with position dependent mass is considered . The authors of Ref. [20] use the following "Fourier inspired" discretization for the derivative (DFT stands for Discrete Fourier Transform and k is the reciprocal space variable)

$$\frac{d}{dx} \longrightarrow \mathrm{DFT}^{-1}\, k\, \mathrm{DFT} \tag{1.58}$$

and report a convergence rate exponentially fast in the number of DFT points.

1.8 Solution of the transport problem

We treat the transport in the framework of the Landauer theory, thus under the hypothesis of linear response regime and phase coherent, non dissipative conduction.
In the previous sections we have described the numerical methods that can be used to obtain the fundamental modes (each one characterized by a longitudinal wave vector κ_x and four functions Φ) through which charge transport takes place in a graphene ribbon with translational invariance in the longitudinal direction.
However, in general, in each of these sections the total wave function $\psi(\boldsymbol{r})$ will

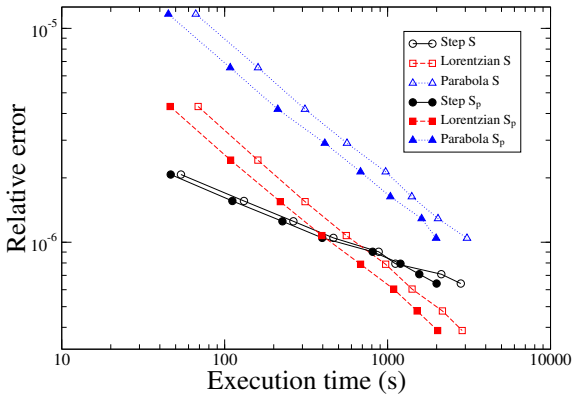

Figure 1.9: Scaling with the execution time of the relative error for the largest real eigenvalue using the spatial methods.

be a linear combination of these modes, and, from Eq (1.31) and Eq (1.31) we deduce that the total functions $\psi_\alpha(\boldsymbol{r})$ and $F_\alpha^{\boldsymbol{K}^{(\prime)}}(\boldsymbol{r})$ ($\alpha = A, B$) will be linear combinations with the same coefficients of ψ of the corresponding single-mode quantities.

In particular, the total wave functions on the two sublattices $\psi_\alpha(\boldsymbol{r})$ will be a linear combination of functions $\psi_{\alpha i}(\boldsymbol{r})$ of the form:

$$\begin{aligned}\psi_{\alpha i}(\boldsymbol{r}) &= \left(e^{-iKy}\Phi_{\alpha i}^{\boldsymbol{K}}(y) - ie^{iKy}\Phi_{\alpha i}^{\boldsymbol{K}'}(y)\right)e^{i\kappa_{xi}x} \\ &\equiv \chi_{\alpha i}(y)\, e^{i\kappa_{xi}x}\end{aligned} \tag{1.59}$$

(where we have exploited the factorization (1.35)). In the general case in which the potential energy $U(\vec{r})$ inside the ribbon varies not only along y but also in the longitudinal direction x and edge discontinuities are present, we can approximate the ribbon as a series of transversal sections, in which U is assumed independent of x and the edges are continuos (see Fig. 1.13). In each of these sections we can apply the methods discussed in the previous sections to estimate the modes and the associated κ_x wavevectors. A mode-matching approach can then be used to connect these partial results in a consistent way. In particular we resort to a recursive scattering matrix approach, according to

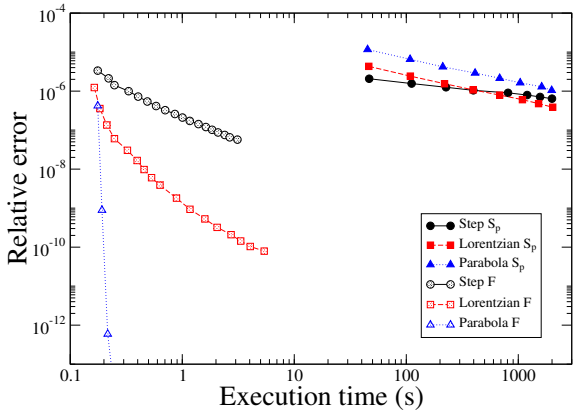

Figure 1.10: Scaling with the execution time of the relative error for largest real eigenvalue. Comparison between the Fourier method and the spatial S_p one. In the case of the parabolic potential the precision almost immediately reaches the machine precision.

which we first evaluate the scattering matrices associated to the discontinuities, and then we compose them recursively to obtain the scattering matrix of the overall system. The mode-matching computation performed at a given discontinuity will provide the elements of the corresponding scattering matrix, namely the transmission and reflection coefficients t_{ni} and r_{ni}. In the following, we first discuss the physical constraints from which the matching conditions derive; then we present the numerical procedure.

In correspondence of the interfaces between adjacent sections with longitudinally constant potential, if we suppose that no δ-type potentials are present, the continuity of the total wave functions must be enforced. According to the expression (1.31) $\psi(\boldsymbol{r})$ is equal to sum of the atomic wave functions modulated by $\psi_A(\boldsymbol{r})$ on the A atoms and by $i\,\psi_B(\boldsymbol{r})$ on the B ones. Because of the strong spatial localization of the atomic orbitals, the continuity of $\Psi(\boldsymbol{r})$ across the discontinuity results, thus, in the separate continuity of the functions $\psi_A(\boldsymbol{r})$ and $\psi_B(\boldsymbol{r})$. Furthermore, by transforming the expressions (1.59) in the reciprocal

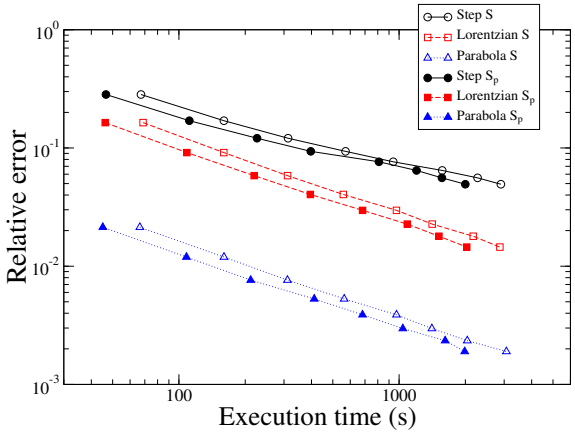

Figure 1.11: Scaling with the execution of the relative error smallest real eigenvalue time using the spatial methods.

space, we see that the slowly-varying components of the envelope functions Fs are translated by the complex exponentials near the large wave vectors $\boldsymbol{K}$ and $\boldsymbol{K}'$. Therefore each of the functions $\psi_\alpha(\boldsymbol{r})$ have in the reciprocal space components strongly localized around the two inequivalent Dirac points, which are significantly separated from each other. Due to this separation, the continuity of the functions $\psi_\alpha(\boldsymbol{r})$ implies also the continuity of the envelope functions F. Here we can notice a difference between the solution of the Dirac problem and that of a Schrödinger problem. In the Schrödinger case, besides the continuity of the envelope function over all the interface between adjacent sections, we should enforce the continuity of its normal derivative wherever the potential energy has a finite value on both sides of the interface. Indeed, the Schrödinger equation directly relates the second derivative of the envelope function to the value of the wave function and of the potential energy. This guarantees also the continuity across the overall section of the probability current density, that in the Schrödinger case depends both on the value of the envelope function and of its first derivative. The Dirac equation, instead, involves the first derivative of the envelope functions and this results into a constraint only for the con-

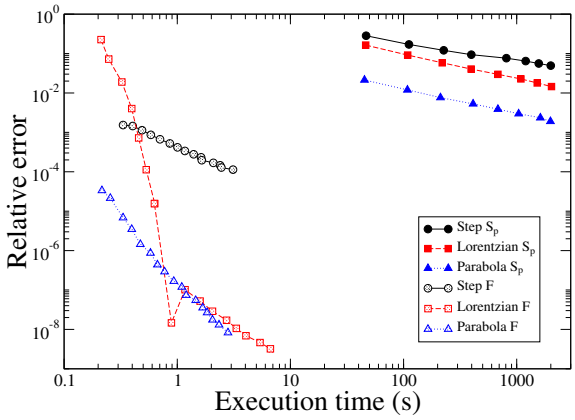

Figure 1.12: Scaling with the execution time of the relative error for the smallest real eigenvalue. Comparison between the Fourier method and the spatial S_p one. The apparent discontinuity in the scaling for the Lorentzian potential is due to the oscillatory convergence to the asymptotic value.

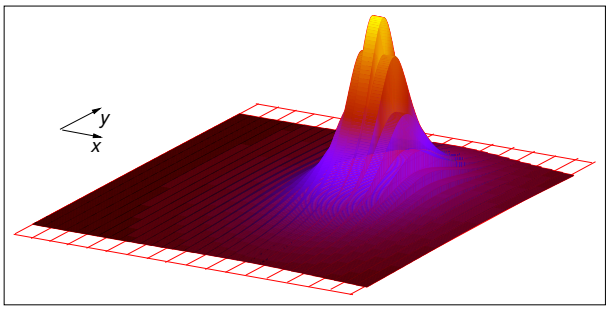

Figure 1.13: Example of the partitioning of the simulation domain into transversal regions in the presence of a Lorentzian-shaped potential. Inside each transverse region the potential is approximated as longitudinally constant.

tinuity of the envelope functions themeselves. However, the continuity of the envelope functions is sufficient to guarantee the continuity of the probability current density, which in this case has the expression [11]

$$J_x(y) = -i\, v_F\, \boldsymbol{F}^\dagger (I \otimes \sigma_x) \boldsymbol{F}\,, \tag{1.60}$$

where

$$\boldsymbol{F} = \left[F_A^{\boldsymbol{K}}, F_B^{\boldsymbol{K}}, F_A^{\boldsymbol{K}'}, F_B^{\boldsymbol{K}'} \right]^T \tag{1.61}$$

and I denotes the 2×2 identity matrix.

Let us now describe in some detail the adopted numerical strategy, focusing on a single discontinuity. We notice that, by exploiting the linearity of the problem, it is possible to evaluate independently of one another the columns of the scattering matrix; this corresponds to impose the matching by considering injection of a single mode at a time, from the left side or from the right side, toward the discontinuity. In the case of a generic mode i impinging from the left side to the discontinuity the wave functions $\psi_\beta(\vec{r})$ on the left side can be written as:

$$\chi_{\beta i}^{l+}(y)\, e^{i\kappa_{xi}^{l+}(x-x_{in})} + \sum_n r_{ni} \chi_{\beta n}^{l-}(y)\, e^{i\kappa_{xn}^{l-}(x-x_{in})}\,, \tag{1.62}$$

while on the right side they can be expressed as

$$\sum_n t_{ni} \chi_{\beta n}^{r+}(y)\, e^{i\kappa_{xn}^{r+}(x-x_{out})}\,. \tag{1.63}$$

In the previous equations x_{in} and x_{out} are the longitudinal positions of the entrance and exit of the considered transverse region, while r_{ni} and t_{ni} are the reflection an transmission coefficients. Moreover we have used the superscript l (r) to denote a mode injected from left (right) and the superscript $+$ ($-$) to indicate a right-going (left-going) mode. We subdivide the modes into right-moving and left-moving according to the sign of the associated longitudinal probability current I_x, positive for the former and negative for the latter. If a mode has $I_x = 0$, we consider it right-going if $\Im(\kappa_x) > 0$ and left-going if $\Im(\kappa_x) \leq 0$, in order to avoid the numerical problems deriving from diverging modes. We notice that the calculation of the probability current in the longitudinal direction can be carried out directly in terms of the coefficients

$[a_0^\alpha]_m$; indeed, by integrating over the transverse section Eq. (1.60) and using Eq. (1.53) we easily arrive at

$$I_x = \int_0^{\tilde{W}} J_x(y)dy = 4v_F\tilde{W}\Re\left(\sum_{n=-D}^{D}(a_n^A)^* a_n^B\right). \tag{1.64}$$

Moreover, by using definition eq. (1.78), I_x can be rewritten as

$$I_x = v_F \int_0^{2\tilde{W}} \vec{\varphi}(y)^\dagger \sigma_x \vec{\varphi}(y)dy\,, \tag{1.65}$$

from which it can be shown (*cf.* Eqs. (1.86) and (1.88) in Sec 1.9) that $(I_x)_{-\kappa_x} = -(I_x)_{\kappa_x}$, $(I_x)_{\kappa_x^*} = (I_x)_{\kappa_x}$ and $(I_x)_{-\kappa_x^*} = -(I_x)_{\kappa_x}$. In particular, if κ_x is purely imaginary, we have that $I_x = -I_x$ and therefore $I_x = 0$, i.e. purely imaginary modes do not carry current. This is in general not true for complex eigenvalues.

The continuity of the wave functions ψ_β implies the equality of the functions (1.62) and (1.63) in correspondence of the longitudinal coordinate $x = x_{dis}$ of the discontinuity:

$$\begin{aligned}&\chi_{\beta i}^{l+}(y)\, e^{i\kappa_{xi}^{l+}(x_{dis}-x_{in})} + \sum_n r_{ni}\chi_{\beta n}^{l-}(y)\, e^{i\kappa_{xn}^{l-}(x_{dis}-x_{in})} = \\ &\sum_n t_{ni}\chi_{\beta n}^{r+}(y)\, e^{i\kappa_{xn}^{r+}(x_{dis}-x_{out})}\end{aligned}\,. \tag{1.66}$$

An equation analogous to Eq. (1.66) can be derived in the case of a single mode i impinging from the right side:

$$\begin{aligned}&\chi_{\beta i}^{r-}(y)\, e^{i\kappa_{xi}^{r-}(x_{dis}-x_{in})} + \sum_n r_{ni}\chi_{\beta n}^{r+}(y)\, e^{i\kappa_{xn}^{r+}(x_{dis}-x_{in})} = \\ &\sum_n t_{ni}\chi_{\beta n}^{l-}(y)\, e^{i\kappa_{xn}^{l-}(x_{dis}-x_{out})}\end{aligned}\,. \tag{1.67}$$

Clearly, in the numerical approximation of Eq. (1.66) and (1.67) we can include only a finite number of modes; we denote the number of the left-going (right-going) modes taken into account on the left side as N^{l-} (N^{l+}), and, correspondingly with N^{r-} (N^{r+}) the number of those considered on the right side. In particular, we include in $N^{l\pm}$ and $N^{r\pm}$ all the modes with $I_x \neq 0$

and a number of modes with $I_x = 0$, that we increase until convergence in the conductance calculation is reached. For each included mode with real or purely imaginary κ_x, also the mode corresponding to $-\kappa_x$ is taken into account, so that $N^{l-} = N^{l+}$ and $N^{r-} = N^{r+}$. Moreover, for each included mode with complex κ_x (with non-zero real and imaginary part), also the modes corresponding to $-\kappa_x$, κ_x^* and $-\kappa_x^*$ are considered. As will be clear from the next section, this last choice guarantees the conservation of the current in the transverse direction.
Eqs. (1.66) and (1.67) are systems of two coupled equations that must be satisfied by the $N^{l-} + N^{r+}$ unknowns t_{ni} and r_{ni} for each value of $y \in [0, 2\tilde{W}]$. In order to evaluate all the elements of the scattering matrix, they have to be solved for $i = 1, \ldots, N^{l+}$ and $i = 1, \ldots, N^{r-}$, respectively. A convenient approach to handle the problem is to project each system of coupled equation over a set of suitably chosen functions, in order to map it into a linear system of $N^{l-} + N^{r+}$ independent equations.
Let us first consider the case in which we have only a discontinuity of the potential energy. In that case, we can project the continuity equations on the eigenmodes $\chi^{r+}_{Aj}(y)$ and $\chi^{l-}_{Bj}(y)$ and exploit the relation (for simplicity we specify the modes with just a single index):

$$\begin{aligned}\langle \chi_{\beta j}(y) | \chi_{\beta i}(y) \rangle = \int_0^{\tilde{W}} \chi^*_{\beta j}(y) \chi_{\beta i}(y) dy \approx \\ \int_0^{\tilde{W}} \left[\Phi^{\boldsymbol{K}}_{\beta j}(y)^* \Phi^{\boldsymbol{K}}_{\beta i}(y) + \Phi^{\boldsymbol{K}'}_{\beta j}(y)^* \Phi^{\boldsymbol{K}'}_{\beta i}(y) \right] dy = \\ 2\,\tilde{W} \sum_{n=-D}^{D} \left(a_n^{\beta j}\right)^* a_n^{\beta i} \,.\end{aligned} \tag{1.68}$$

where we have neglected the rapidly oscillating terms in the integrand, which average to zero, and we have used the relations (1.53).
Since, as we have seen in (1.54), the functions $\chi_{\beta i}(y)$ can be expressed as

$$\chi_{\beta i}(y) = 2\,i \sum_{n=-D}^{D} \left[a_n^{\beta i} \, \sin\left((n - n_0)\pi y / \tilde{W} \right) \right] , \tag{1.69}$$

a more efficient choice is to project the continuity conditions on the set of independent functions:

$$S_j(y) = \sin\left((j - n_0)\pi y/\tilde{W}\right) \tag{1.70}$$

where j is an integer. Using this set, if there is no discontinuity in the wire geometry we have that

$$\langle S_j(y)|\chi_{\beta i}(y)\rangle = \int_0^{\tilde{W}} S_j^*(y)\chi_{\beta i}(y)dy = i\tilde{W}a_j^{\beta i}\,. \tag{1.71}$$

We point out that the use of the basis (1.70) allows to impose the mode-matching in an exact (within the numerical errors) form. We notice that if the matrix M_0 diagonalized on the left of the discontinuity (see Sec. 1.6) has the same dimension of that on the right, then the modes $\chi^{l\pm}$ and $\chi^{r\pm}$ have the same number N_c of non-zero Fourier components. Thus, if the condition $N_c = N^{l\pm} = N^{r\pm}$ is verified, from Eq. (1.71) we deduce that the linear system obtained by projecting the coupled equations (1.66) or (1.67) over the $N^{l\pm} = N^{r\pm}$ basis functions (1.70) imposes that all the Fourier components of the ψ_α on the left coincide with the corresponding of the ψ_α on the right. As a consequence, in this case the matching is enforced exactly.
The method can be extended to the case of a domain of arbitrary shape, by approximating the structure with a succession of ribbons of different width, as exemplified Fig. 1.14. The width discontinuities will correspond to some of the interfaces between the transverse sections into which the domain is subdivided. Along interfaces corresponding to a width discontinuity zigzag-shaped transverse edges appear (we do not consider discontinuities originating bearded edges). The matching has now to be imposed in such a way to account for the additional boundary conditions to be enforced along these transverse edges. As in zigzag nanoribbons, we impose the vanishing of the wave function on the transverse line of lattice sites at a distance a_{C-C} from the zigzag edges, where approximately the passivation takes place. Depending on whether these lattice sites belong to the A or the B sublattice, this condition corresponds to enforce the vanishing on the same sites of the function ψ_A or ψ_B, respectively. This corresponds to a continuity condition for ψ_A (ψ_B) along these segments, because the zigzag edges delimit the ribbon from the region outside it, where the

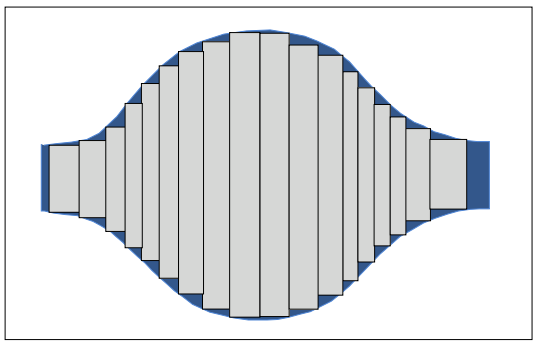

Figure 1.14: Example of approximation of a domain of arbitrary shape with a sequence of rectangular region of different width and length.

wave function is null. Along the remaining part of the interface the continuity has to be imposed, as for the case of constant width, for both ψ_A and ψ_B. We do not consider the case represented in Fig. 1.15 b), where the upper and lower passivation lines correspond to atoms belonging to different sublattices, so that discontinuities in the geometry occour only at the interface between sections of different width, and the overlap region is coincident with the width of the narrower section. The matching can thus be performed by projecting the equations which enforce the continuity of ψ_A (ψ_B) over functions with support extended over the width of the wider section, and the equations which enforce the continuity of ψ_B (ψ_A) over functions with support limited to the width of the narrower one.

Also in this case, with some algebraic manipulation, we can find an expression for the projections in terms of the Fourier coefficients, without the necessity to use the eq. (1.53) and to perform a numerical integration over a transverse spatial grid. For example, we can project the functions $\chi_{\beta i}(y)$ defined over a domain $[\Delta_1, \Delta_1 + \tilde{W}_1]$ over a basis of sines defined over a domain $[\Delta_2, \Delta_2 + \tilde{W}_2]$

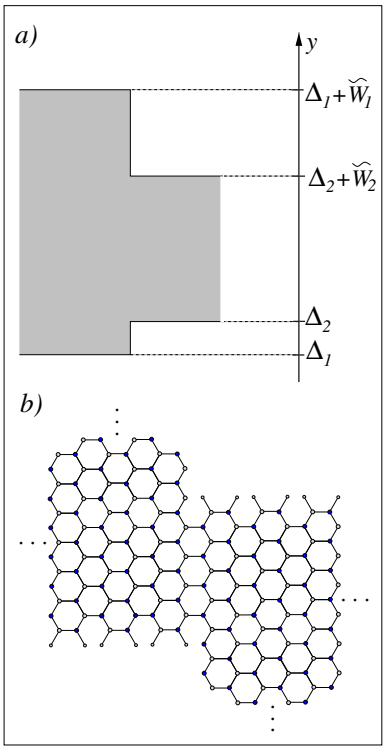

Figure 1.15: a) Sketch of a width discontinuity in a nanoribbon. b) Detail of a width discontinuity for the case $\Delta_1 + \tilde{W}_1 > \Delta_2 + \tilde{W}_2$ and $\Delta_1 > \Delta_2$; as it can be noticed, the atomic sites on the upper and lower transversal edges belong to different sublattices.

(see Fig. 1.15 a)) over an integration domain $[\Delta, \Delta + \tilde{W}]$ using the relation:

$$\begin{aligned}\langle S_j(y)|\chi_{\beta i}(y)\rangle &= \int_{\Delta}^{\Delta+\tilde{W}} \left\{ \left[\sin\left(\frac{(j-n_{02})\pi(y-\Delta_2)}{\tilde{W}_2}\right)\right] \right. \\ &\left. \left[2\,i\sum_{m=-D}^{D} a_{mn}^{\beta i}\,\sin\left(\frac{(m-n_{01})\pi(y-\Delta_1)}{\tilde{W}_1}\right)\right]\right\} dy \\ &= i\sum_{m=-D}^{D} a_{mn}^{\beta i}(h(c_{1-},c_{2-}) - h(c_{1+},c_{2+}))\end{aligned} \tag{1.72}$$

where $n_{01} = -\lfloor K\tilde{W}_1/\pi \rceil$ and $n_{02} = -\lfloor K\tilde{W}_2/\pi \rceil$, and

$$\begin{aligned} h(a,b) &= \frac{\sin(a(\Delta+\tilde{W})-b) - \sin(a\Delta - b)}{a}\,, \\ c_{1\pm} &= \pi\left(\frac{j-n_{02}}{\tilde{W}_2} \pm \frac{m-n_{01}}{\tilde{W}_1}\right)\,, \\ c_{2\pm} &= \pi\left(\frac{(j-n_{02})\Delta_2}{\tilde{W}_2} \pm \frac{(m-n_{01})\Delta_1}{\tilde{W}_1}\right)\,. \end{aligned} \tag{1.73}$$

We notice that, when a width discontinuity is involved, the matching cannot be imposed exactly, but only within an approximation that asymptotically improve by increasing the number of modes considered in the computation. Indeed, due to the difference in the supports, the modes defined over the narrower section have an infinite number of components when expanded in a basis defined over the wider section. As a consequence, when the continuity over the wider section is imposed, in order to obtain costraints involving all components of the modes on the narrower section, it would be needed to project Eqs. (1.66) and (1.67) on a infinite number of basis functions. If the ratio between the width of the narrower and the wider section is small, the number of components to be taken into account can be quite large. Since, for consistency, this requires a large number of unknowns (r_{ni} and/or t_{ni}) to be considered and, thus, a large number of modes, it is needed to diagonalize quite large matrices. We can conclude that in the presence of a geometrical discontinuity the numerical evaluation of the scattering matrix associated to a transversal region can be much more demanding with respect to the case in which only the potential is discontinuous.

Once the scattering matrix

$$S = \begin{pmatrix} r & \tilde{t} \\ t & \tilde{r} \end{pmatrix} \tag{1.74}$$

(where r and t are the reflection and transmission matrices, respectively, for the modes impinging from the left, while $\tilde{r}$ and $\tilde{t}$ for the modes impinging from the right) corresponding to the various (potential or boundary) discontinuities have been computed, they can be composed by using the standard procedure, see e.g. Ref. [61], in order to obtain the total scattering matrix S describing transport in the ribbon. It is then convenient to introduce a different form S' of the scattering matrix:

$$S' = \begin{pmatrix} r' & \tilde{t}' \\ t' & \tilde{r}' \end{pmatrix} , \tag{1.75}$$

relating the "current amplitude" instead of the "wave amplitude" of the modes [61]. This matrix involves only the modes with $I_x \neq 0$ and its elements are given by

$$\begin{aligned} r'_{nm} &= r_{nm}\sqrt{|I_{xn}|/|I_{xm}|} \quad , \quad t'_{nm} = t_{nm}\sqrt{|I_{xn}|/|I_{xm}|} \quad , \\ \tilde{r}'_{nm} &= \tilde{r}_{nm}\sqrt{|I_{xn}|/|I_{xm}|} \quad , \quad \tilde{t}'_{nm} = \tilde{t}_{nm}\sqrt{|I_{xn}|/|I_{xm}|} \, . \end{aligned} \tag{1.76}$$

By using the conservation of the current it can be shown that S' is unitary (see e.g. [61]).

We can then compute the conductance of the ribbon by means of the Landauer-Büttiker formula

$$G = \frac{2\,e^2}{h} \sum_{n,m} |t'_{nm}|^2 \, , \tag{1.77}$$

where the sum runs only on the modes with $I_x \neq 0$ in the first and last transversal regions of the ribbon.

In studies of unconfined graphene or ribbons with large aspect ratio, it is safe to assume periodic boundary conditions instead of the Dirichlet condition that we have used here. In those cases the two Dirac points completely decouple and it is customary to solve the Dirac equation for just one valley and use in Eq. (1.77) a factor of 4 instead of 2. We cannot do that since, as previously noted after Eq. (1.38), the Dirichlet boundary conditions introduce a coupling between the two inequivalent Dirac points.

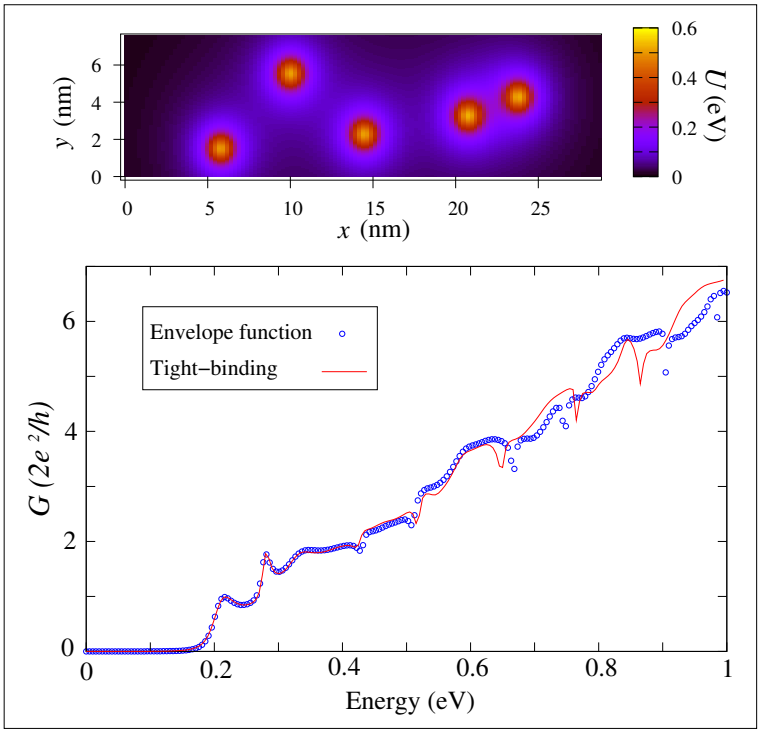

Figure 1.16: Bottom: comparison of the results obtained for the zero-temperature values of the conductance as a function of the Fermi energy with the corresponding results from a tight-binding simulation. The results refer to a $\approx$ 29 nm long armchair nanoribbon with 60 dimer lines. Top: map of the potential landscape inside the ribbon.

As an example of simulation of transport, in Fig 1.16 we show the plot of the transmission $[Gh/(2e^2)]$ as a function of the injection energy, for an armchair nanoribbon with a potential obtained as the superposition of five slowly-varying Lorentzian functions. This behavior is compared with that obtained, for the same case, using a Non Equilibrium Green's Functions code (NanoTCAD ViDES [23]) in which a tight-binding model for the structure has been adopted. We note a substantial agreement between the results of the two approaches, as far as low injection energies, for which the envelope function method can be rigorously applied, are considered.

1.9 $\mathcal{PT}$-symmetry breaking in armchair graphene nanoribbons

One of the fundamental axioms in quantum mechanics is the requirement of the Hermiticity for the Hamiltonian. This ensures that all the expectation values of the energy are real and that the time-evolution operator e^{-iHt} is unitary, so that the norms of the states remain constant in time.
In the literature, however, it has been quite recently pointed out that Hermiticity is not necessary in order for the aforementioned conditions on eigenvalues and states norms to be satisfied. It has been shown, in particular, that it is possible to describe physical systems by means of so-called $\mathcal{PT}$-symmetric Hamiltonians, namely Hamiltonians that commute with the composition of the linear parity operator $\mathcal{P}$, defined by the properties

$$\mathcal{P}p\mathcal{P}^{-}1 = -p\,, \qquad \mathcal{P}x\mathcal{P}^{-}1 = -x\,,$$

and the antilinear time reversal operator $\mathcal{T}$, defined by the properties

$$\mathcal{T}p\mathcal{T}^{-}1 = -p\,, \qquad \mathcal{T}x\mathcal{T}^{-}1 = -x\,, \qquad \mathcal{T}i\mathcal{T}^{-}1 = -i \text{ (antilinearity)}\,.$$

These Hamiltonians may be not Hermitian, but nevertheless they can have a real spectrum. The condition under which this happens is related to the realization of the $\mathcal{PT}$-simmetry of the eigenvectors of the Hamiltonian. Indeed, since the $\mathcal{PT}$ operator is not linear, a $\mathcal{PT}$-symmetric Hamiltonian not necessarily shares its eigenvectors with it. When the eigenvectors of a $\mathcal{PT}$-symmetric

Hamiltonian are not $\mathcal{PT}$-symmetric it is said that the $\mathcal{PT}$-symmetry of H is *spontaneously broken*. Otherwise the symmetry is said to be *unbroken*. It is easy to show that in this last case the spectrum of the Hamiltonian has to be real. To this aim we will use the following properties of the operator $\mathcal{PT}$:

$$(\mathcal{PT})^2 = 1$$

(it immediately follows from $\mathcal{P}^2 = \mathcal{T}^2 = 1$ and $[\mathcal{P}, \mathcal{T}] = 0$), and

$$(\mathcal{PT})i(\mathcal{PT}) = -i$$

(antilinearity: it is immediately deduced from the previous property and from the antilinearity of the operator $\mathcal{T}$).
We start by showing that the eigenvalues of the operator $\mathcal{PT}$ are always different from zero. Let ψ be an eigenvector of $\mathcal{PT}$ and λ the corresponding eigenvalue; by applying the operator $\mathcal{PT}$ to both side of the equation $\mathcal{PT}\psi = \lambda\psi$ and exployting the property $(\mathcal{PT})^2 = 1$, we can write

$$\psi = (\mathcal{PT})\lambda(\mathcal{PT})^2\psi = (\mathcal{PT})\lambda(\mathcal{PT})\lambda\psi = \lambda^*\lambda\psi\,,$$

where, the last equality follows from the antilinearity of $\mathcal{PT}$. We obtain $\psi = |\lambda|^2\psi$ and, thus, $\lambda = e^{i\alpha} \neq 0$.
Let us now suppose that ψ is also an eigenvector of the $\mathcal{PT}$-symmetric Hamiltonian H: $H\psi = E\psi$. With analogous steps and exploiting the fact that H commutes with $\mathcal{PT}$, we obtain:

$$H\mathcal{PT}\psi = \mathcal{PT}(E\mathcal{PT})^2\psi \Rightarrow \lambda H\psi = \mathcal{PT}E\mathcal{PT}\lambda\psi \Rightarrow \lambda E\psi = \lambda E^*\psi\,.$$

Since $\lambda \neq 0$, it must be $E^* = E$, namely E has to be real.
When the $\mathcal{PT}$-symmetry is spontaneously broken, eigenvalues with a non zero imaginary part can arise, together with *exceptional points*. Exceptional points are singularities in the spectrum of an operator arising for particular values of a parameter on which the operator depends. They are a typical feature of non-Hermitian Hamiltonians (see *e.g.* the reviews [51]) with no Hermitian counterpart. At an exceptional point two (or more) eigenvalues coalesce, becoming degenerate. This does not represent a genuine degeneracy, because also

the the corresponding eigenvectors coalesce and the eigenspace of the coalescing eigenvalues becomes one-dimensional. As a consequence, at an exceptional point the operator is not diagonalizable [50]. Exceptional points can produce measurable effects and, in fact, their occurrence has been experimentally observed [52–54].
To our knowledge, all the previously proposed physical examples of systems governed by non-Hermitian $\mathcal{PT}$-symmetric Hamiltonians involve dissipative systems, the main emphasis being on microwave cavities [52], optical lattices [55, 56] and lasers [57]. In the following we show that, because of the spinorial nature of the wave function, some properties of graphene nanoribbons can be described by means of an effective non-Hermitian $\mathcal{PT}$-symmetric Hamiltonian, although there is no dissipation. We give numerical evidence for the $\mathcal{PT}$-symmetry breaking and provide an order parameter. Finally we study the behavior of eigenmodes and eigenfunctions in the neighborhood of exceptional points.

1.9.1 The model and the notations

Let us focus on a single transverse section of an AGNR; let us consider open boundary conditions along the longitudinal x direction and the presence of a potential constant in the longitudinal y direction. We refer to the formulation in the doubled domain described in Sec 1.5, but, in order to simplify some calculations, we consider a slightly different reference frame, so that Eq. 1.42 are now referred to the interval $[\tilde{W}, \tilde{W}]$, and the functions $\vec{\varphi}$ and h are now defined as

$$\vec{\varphi}(y) = \begin{cases} \vec{\varphi}^{\boldsymbol{K}}(y + \tilde{W}) & y \in [-\tilde{W}, 0] \\ e^{i2K\tilde{W}} \vec{\varphi}^{\boldsymbol{K}'}(\tilde{W} - y) & y \in [0, \tilde{W}]\,, \end{cases} \tag{1.78}$$

and

$$h(y) = f(\tilde{W} - |y|)\,. \tag{1.79}$$

Moreover, we rewrite Eq. (1.42) in the form

$$i\partial_y \vec{\varphi}(y) = H^{k_x}(y)\vec{\varphi}(y), \quad \vec{\varphi}(\tilde{W}) = e^{2iK\tilde{W}} \vec{\varphi}(-\tilde{W})\,, \tag{1.80}$$

with

$$H^{k_x}(y) = h(y)\sigma_y - ik_x\sigma_z\,, \tag{1.81}$$

so that, by interpreting y/v_F as the time, the first of Eq. (1.80) can be thought of as formally equivalent to a Schrödinger equation for the non-Hermitian Hamiltonian $v_F H^{k_x}$.

1.9.2 Symmetries

From Eq. (1.80) we deduce a simple result on the degeneration of the k_x modes. If we denote by $\mathcal{U}(y)$ the time evolution operator associated to a given eigenvalue k_x, *i.e.* $\vec{\varphi}(y) = \mathcal{U}(y)\vec{\varphi}(-\tilde{W})$ with $\vec{\varphi}(y)$ in the corresponding eigenspace, the boundary condition can be written as $\mathcal{U}(\tilde{W})\vec{\varphi}(-\tilde{W}) = e^{2iK\tilde{W}}\vec{\varphi}(-\tilde{W})$. By using the explicit form of H^{k_x} it is easy to check that $\mathcal{U}^{-1}(\tilde{W}) = \sigma_x\mathcal{U}(\tilde{W})\sigma_x$, from which it follows that

$$\mathcal{U}(\tilde{W})\sigma_x\vec{\varphi}(-\tilde{W}) = e^{-2iK\tilde{W}}\sigma_x\vec{\varphi}(-\tilde{W})\,. \tag{1.82}$$

If $\exp(4iK\tilde{W}) \neq 1$, there cannot be eigenvectors of $\mathcal{U}(\tilde{W})$ other than $\vec{\varphi}(-\tilde{W})$ and $\sigma_x\vec{\varphi}(-\tilde{W})$, and hence just one independent eigenmode corresponds to each k_x. From now on we consider lengths $\tilde{W}$ for which this condition is verified, *i.e.* nanoribbons that are semiconducting in the absence of an external potential also when edge relaxation is neglected.

We now derive some properties of eigenstates that will be used later. Let us denote by $\vec{\varphi}_{k_x}(y)$ the eigenmode associated to k_x and consider the conjugated of the first of Eq. (1.80):

$$i\frac{d\vec{\varphi}^*_{k_x}}{dy}(y) = h(y)\sigma_y\vec{\varphi}^*_{k_x}(y) - i\kappa^*\sigma_z\vec{\varphi}^*_{k_x}(y) \tag{1.83}$$

Since $\vec{\varphi}^*_{k_x}(\tilde{W}) = e^{-2iK\tilde{W}}\vec{\varphi}^*_{k_x}(-\tilde{W})$, the function $\vec{\varphi}^*(y)$ no longer verifies the second of Eq. (1.80), so we consider the function $\vec{\eta}(y) = \vec{\varphi}_{k_x}(-y)$, that satisfies the right boundary conditions. In terms of $\vec{\eta}(y)$ Eq. (1.83) becomes

$$i\frac{d\vec{\eta}^*_{k_x}}{dy}(y) = -h(y)\sigma_y\vec{\eta}^*_{k_x}(y) + i\kappa^*\sigma_z\vec{\eta}^*_{k_x}(y) \tag{1.84}$$

or

$$\begin{aligned} i\,\frac{d(\sigma_x\vec{\eta}^*_{k_x})}{dy}(y) &= -h(y)\sigma_x\sigma_y\sigma_x(\sigma_x\vec{\eta}^*_{k_x}(y)) + i\kappa^*\sigma_x\sigma_z\sigma_x(\sigma_x\vec{\eta}^*_{k_x}(y)) = \\ i\,\frac{d(\sigma_x\vec{\eta}^*_{k_x})}{dy}(y) &= h(y)\sigma_y(\sigma_x\vec{\eta}^*_{k_x}(y)) + i\kappa^*\sigma_z(\sigma_x\vec{\eta}^*_{k_x}(y))\,. \end{aligned} \tag{1.85}$$

The function $\sigma_x\vec{\eta}_{k_x}(y) = \sigma_x\vec{\varphi}^*_{k_x}(-y)$ satisfies thus Eqs. (1.80), but with k_x replaced by k_x^*, and is thus proportional to the eigenvector corresponding to k_x^*:

$$\vec{\varphi}^*_{k_x^*}(y) \propto \sigma_x\vec{\varphi}^*_{k_x}(-y)\,. \tag{1.86}$$

In the case of real k_x Eq. (1.86) implies

$$\begin{aligned}|\vec{\varphi}_{k_x}(y)|^2 = &\vec{\varphi}^\dagger_{k_x}(y)\vec{\varphi}_{k_x}(y) = \left\{\sigma_x\left(\vec{\varphi}^*_{k_x}(-y)\right)\right\}^\dagger\sigma_x\vec{\varphi}^*_{k_x}(-y) = \\ &\vec{\varphi}^T_{k_x}(-y)\sigma_x\sigma_x\vec{\varphi}^*_{k_x}(-y) = \vec{\varphi}^T_{k_x}(-y)\vec{\varphi}^*_{k_x}(-y) = \\ &|\vec{\varphi}_{k_x}(-y)|^2\,;\end{aligned} \tag{1.87}$$

namely, for $k_x \in \mathbb{R}$, $|\vec{\varphi}_{k_x}(y)|^2$ is $\mathcal{P}$-even.
Moreover, with analogous steps, it is possible to derive the relation

$$\vec{\varphi}^*_{-k_x^*}(y) \propto \sigma_z\vec{\varphi}^*_{k_x}(-y)\,, \tag{1.88}$$

that implies $|\vec{\varphi}_{k_x}(y)|^2 = |\vec{\varphi}_{k_x}(-y)|^2$ for purely imaginary k_x. From Eq. (1.86) and Eq. (1.88) it follows that if k_x is in the spectrum then there are also k_x^*, $-k_x^*$ and $-k_x$. Thus the spectrum has a $Z_2 \times Z_2$ symmetry.
Finally, we show that the function $\vec{\varphi}^T(-y)\sigma_z\vec{\varphi}(y)$ is independent of y:

$$\begin{aligned}&\frac{d}{dy}\left(\vec{\varphi}(y)^T(-y)\sigma_z\vec{\varphi}(y)\right) = -\frac{d\vec{\varphi}^T}{dy}(-y)\sigma_z\vec{\varphi}(y) + \vec{\varphi}^T(y)\sigma_z\frac{d\vec{\varphi}}{dy}(-y) = \\ &i\left(h(-y)\sigma_y - ik_x\sigma_z\right)\vec{\varphi}^T(-y)\sigma_z\vec{\varphi}(y) - i\vec{\varphi}^T(-y)\sigma_z\left(h(y)\sigma_y - ik_x\sigma_z\right)\vec{\varphi}(y) = \\ &\vec{\varphi}^T(-y)\left(h(-y)\sigma_x + k_x\right)\vec{\varphi}(y) - \vec{\varphi}^T(-y)\left(h(y)\sigma_x + k_x\right)\vec{\varphi}(y) = 0\,,\end{aligned} \tag{1.89}$$

where in the last passage we used $h(y) = h(-y)$.
To reveal the $\mathcal{PT}$ symmetry of the problem it is convenient to take the square of Eq. (1.80):

$$\begin{aligned}-\partial_y^2\vec{\varphi}(y) = &i\partial_y\left[\left(h(y)\sigma_y - i\kappa_x\sigma_z\right)\vec{\varphi}(y)\right] = \\ &i(\partial_y h(y))\sigma_y\vec{\varphi}(y) + \left(h(y)\sigma_y - i\kappa_x\sigma_z\right)\left(i\partial_y\vec{\varphi}(y)\right) = \\ &i(\partial_y h(y))\sigma_y\vec{\varphi}(y) + \left(h(y)\sigma_y - i\kappa_x\sigma_z\right)\left(h(y)\sigma_y - i\kappa_x\sigma_z\right)\vec{\varphi}(y) = \\ &i(\partial_y h(y))\sigma_y\vec{\varphi}(y) + \left(h^2(y) - \kappa_x^2 - i\kappa_x h(y)\{\sigma_y,\sigma_z\}\right)\vec{\varphi}(y) = \\ &i(\partial_y h(y))\sigma_y\vec{\varphi}(y) + \left(h^2(y) - \kappa_x^2 - i\kappa_x h(y)\right)\vec{\varphi}(y)\,.\end{aligned} \tag{1.90}$$

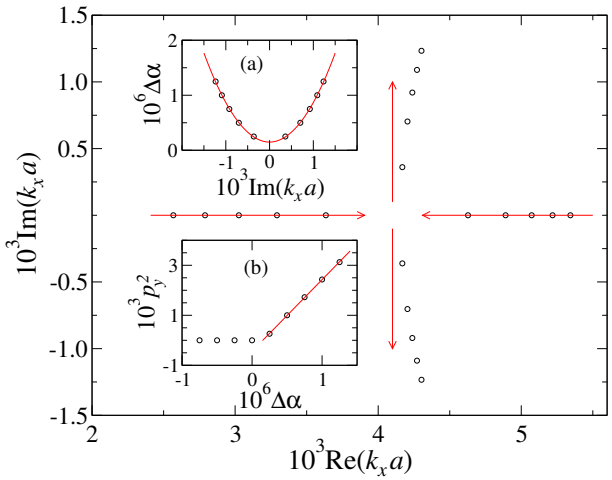

Figure 1.17: Coalescing of two eigenvalues along the real line for $\epsilon = 1/5$; the arrows denote the direction of increasing α values ($\Delta\alpha \equiv \alpha - 0.060953$). In the inset (a) the imaginary parts of the coalescing eigenvalues are shown together with a fit of the form $\alpha = c_1 + c_2(\mathrm{Im}\,(k_x a))^2$. The inset (b) shows the behavior of the square of the transverse momentum together with a linear fit.

Rearranging we find

$$\left(\hat{p}_y^2 - h^2 \mp i(\partial_y h)\right)\vec{\varphi}(y) = -k_x^2\vec{\varphi}(y)\,. \tag{1.91}$$

Let us now expand $\vec{\varphi}(y)$ in the basis of the eigenstates of σ_y as

$$\vec{\varphi}(y) = \phi_+(y)|+\rangle + \phi_-(y)|-\rangle\,, \tag{1.92}$$

where we denoted with $|+\rangle$ the eigenstate of σ_y corresponding to the eigenvalue 1, and with $|-\rangle$ that corresponding to the eigenvalue -1. By subtituting Eq. (1.92) into Eq. (1.91) and projecting over $|+\rangle$ and $|-\rangle$, we obtain the couple of equations

$$\left(\hat{p}_y^2 - h^2 \mp i(\partial_y h)\right)\phi_\pm(y) = -k_x^2\phi_\pm(y), \tag{1.93}$$

which are clearly invariant under the $\mathcal{PT}$ transformation, being the action of the operators $\mathcal{P}$ and $\mathcal{T}$ defined by $p_y \to -p_y$, $y \to -y$ and $p_y \to -p_y$, $y \to y$,

$i \to -i$, respectively. We see that, if the $\mathcal{PT}$ symmetry is unbroken, then k_x has to be real or imaginary; complex conjugate (intended here as a number with nonzero real and imaginary part) pairs appear in the spectrum only if this symmetry is broken.

We explicitly notice that if the Schrödinger equation is used instead of the Dirac one, the equation corresponding to Eqs. (1.37) is similar to Eq. (1.91) but with an Hermitian left hand side, so that all the k_x values have to be real or imaginary.

In the presence of spontaneously broken symmetries it is customary to look for an order parameter, *i.e.* an observable that vanishes when the symmetry is realized in the spectrum, a non zero value signaling the symmetry breaking. We point out that the mean value of the transverse momentum

$$p_y = \int_0^{\tilde{W}} \vec{\Psi}(y)^\dagger(-i\partial_y)\vec{\Psi}(y)\mathrm{d}y \Big/ \int_0^{\tilde{W}} \vec{\Psi}(y)^\dagger\vec{\Psi}(y)\mathrm{d}y \tag{1.94}$$

satisfies this requirement. This can be easily proved exploiting the symmetries of our problem: from Eqs. (1.86) and (1.88) and because $|\vec{\varphi}(y)|^2$ is $\mathcal{P}$-even and $\vec{\varphi}(-y)^T\sigma_z\vec{\varphi}(y)$ is constant, it follows that the numerator of Eq. (1.94) vanishes if k_x^2 is real. We have numerically checked that the transverse momentum p_y is different from zero when k_x is complex (p_y appears to vanish also for complex k_x values only when the potential satisfies $U(y) = U(\tilde{W} - y)$). Thus, in this system the realization of the $\mathcal{PT}$ symmetry in the spectrum is related to the value of the transverse momentum, which is an order parameter for the $\mathcal{PT}$ symmetry breaking.

Finally, it is worth mentioning that the transformation that reverses the sign of $h(y)$ (*i.e.* σ_z) is unitary and independent of p_y, and hence $|\vec{\varphi}(y)|^2$ is invariant for simultaneous flipping of the signs of the potential and of the energy. This is just a manifestation of the chiral symmetry of the system. As long as $h(y)$ does not have a definite sign, heuristic arguments based on that symmetry indicate the presence of eigenfunctions localized around the minima as well as eigenfunctions localized around the maxima of the potential; the former (latter) ones are expected to describe particles with positive (negative, *i.e.* of opposite sign with respect to k_x) group velocities. These observations provide a simple argument for the existence of some singular behavior: by varying the

energy, eigenmodes with opposite group velocities coalesce in a non-analytic way, because they cannot combine in a two-dimensional eigenspace.

1.9.3 $\mathcal{PT}$-symmetry breaking and exceptional points

If $f(y)$ is constant, Eq. (1.80) can be analytically solved: all the k_x values are real or imaginary and all the eigenstates of the Hamiltonian (their projections on the eigenstates of σ_y, to be precise) are also eigenstates of the $\mathcal{PT}$ operator. This is no longer true when an external potential with non-trivial y dependence is present and we now provide numerical evidence that in this system $\mathcal{PT}$-symmetry can get spontaneously broken. As a simple example we use the Lorentzian shaped potential

$$f(y)\, a = \epsilon - \frac{125}{250 + \alpha^2((y/a) - 150)^2}, \tag{1.95}$$

with $\alpha, \epsilon \in \mathbb{R}$. The general qualitative features are however independent of the particular potential adopted. We choose $\tilde{W} = 500a$ as the effective width of the nanoribbon.
It is simple to (numerically) check that by varying the parameters (α and ε in our example) two different phenomena can occur:

A) the number of the real eigenvalues varies but the number of the complex ones is preserved;

B) the number of the complex eigenvalues changes.

In case A) a couple of real eigenvalues turns into a couple of imaginary ones (or vice versa); the $Z_2 \times Z_2$ symmetry then implies the existence of some values of the parameters for which $k_x = 0$ is a doubly degenerate eigenvalue. However, we are assuming $\exp(4iK\tilde{W}) \neq 1$, and hence only one independent eigenfunction is associated to each eigenvalue; as a consequence, this point of the parameter space is an exceptional point. Case B) is completely analogous: two real or imaginary eigenvalues coalesce and become complex (see Fig. 1.17). However, while in case A) the $\mathcal{PT}$ symmetry is unbroken (or broken, if the number of complex eigenvalues is different from 0) irrespective of the EP, in case B) the EP is associated to $\mathcal{PT}$ symmetry breaking. Clearly this kind of EP appears

in a specular way both in the upper (right) and lower (left) half-plane, because of the $Z_2 \times Z_2$ symmetry.

1.9.4 Behavior near EPs.

If we are not at an exceptional point, the variations of the eigenvalues and eigenvectors are linear in the variation δh of h; in particular we will now show that

$$\int_{-\tilde{W}}^{\tilde{W}} \mathrm{d}y \vec{\varphi}_{k_x}^T(-y) \frac{\delta h}{\delta k_x} \sigma_x \vec{\varphi}_{k_x}(y) = -\int_{-\tilde{W}}^{\tilde{W}} \mathrm{d}y \vec{\varphi}_{k_x}^T(-y) \vec{\varphi}_{k_x}(y)\,. \tag{1.96}$$

Let us consider the equation obtained by multipling the first of Eq. (1.80) on the left by $\vec{\varphi}^T(-y)\sigma_z$:

$$\vec{\varphi}^T(-y)\sigma_z \frac{d\vec{\varphi}(y)}{dy} = \vec{\varphi}^T(-y)h(y)\sigma_x\vec{\varphi}(y) + \vec{\varphi}^T(-y)k_x\vec{\varphi}(y) \tag{1.97}$$

To the first order in the variations we have:

$$\delta\left(\vec{\varphi}^T(-y)\sigma_z \frac{d\vec{\varphi}(y)}{dy}\right) = \delta\vec{\varphi}^T(-y)\sigma_z \frac{d\vec{\varphi}(y)}{dy} + \vec{\varphi}^T(-y)\sigma_z \frac{d(\delta\vec{\varphi}(y))}{dy}\,, \tag{1.98}$$

$$\begin{aligned}\delta\left(\vec{\varphi}^T(-y)h(y)\sigma_x\vec{\varphi}(y)\right) =& \delta\vec{\varphi}^T(-y)h(y)\sigma_x\vec{\varphi}(y) + \vec{\varphi}^T(-y)\delta h(y)\sigma_x\vec{\varphi}(y) + \\ & \vec{\varphi}^T(-y)h(y)\sigma_x\delta\vec{\varphi}(y)\,,\end{aligned} \tag{1.99}$$

$$\delta\left(\vec{\varphi}^T(-y)k_x\vec{\varphi}(y)\right) = \delta\vec{\varphi}^T(-y)k_x\vec{\varphi}(y) + \vec{\varphi}^T(-y)\delta k_x\vec{\varphi}(y) + \vec{\varphi}^T(-y)k_x\delta\vec{\varphi}(y)\,. \tag{1.100}$$

Thus we obtain the relation:

$$\begin{aligned}&\delta\vec{\varphi}^T(-y)\sigma_z \frac{d\vec{\varphi}(y)}{dy} + \vec{\varphi}^T(-y)\sigma_z \frac{d(\delta\vec{\varphi}(y))}{dy} = \delta\vec{\varphi}^T(-y)h(y)\sigma_x\vec{\varphi}(y) + \\ &\vec{\varphi}^T(-y)\delta h(y)\sigma_x\vec{\varphi}(y) + \vec{\varphi}^T(-y)h(y)\sigma_x\delta\vec{\varphi}(y) + \delta\vec{\varphi}^T(-y)k_x\vec{\varphi}(y) + \\ &\vec{\varphi}^T(-y)\delta k_x\vec{\varphi}(y) + \vec{\varphi}^T(-y)k_x\delta\vec{\varphi}(y)\end{aligned} \tag{1.101}$$

Let us now consider the integral for $y \in [-\tilde{W}, \tilde{W}]$ of both sides of Eq. (1.101). On the left side we have:

$$\int_{-\tilde{W}}^{\tilde{W}} dy \delta\vec{\varphi}^T(-y)\sigma_z \frac{d\vec{\varphi}(y)}{dy} + \int_{-\tilde{W}}^{\tilde{W}} dy \vec{\varphi}^T(-y)\sigma_z \frac{d(\delta\vec{\varphi}(y))}{dy}\,. \tag{1.102}$$

Integrating by parts the first term, we obtain

$$\int_{-\tilde{W}}^{\tilde{W}} dy \delta\vec{\varphi}^T(-y)\sigma_z \frac{d\vec{\varphi}(y)}{dy} = \left[\vec{\varphi}^T(-\tilde{W})\sigma_z\delta\vec{\varphi}(\tilde{W}) - \vec{\varphi}^T(\tilde{W})\sigma_z\delta\vec{\varphi}(-\tilde{W})\right] - \int_{-\tilde{W}}^{\tilde{W}} dy \frac{d\vec{\varphi}^T}{dy}(-y)\sigma_z\delta\vec{\varphi}(y)\,; \tag{1.103}$$

since $\vec{\varphi}(\tilde{W}) = e^{2iK\tilde{W}}\vec{\varphi}(-\tilde{W})$ and, consequently, $\delta\vec{\varphi}(\tilde{W}) = e^{2iK\tilde{W}}\delta\vec{\varphi}(-\tilde{W})$, the term in the square brackets is zero. Moreover, by considering that, since the integrand is scalar,

$$\frac{d\vec{\varphi}^T}{dy}(-y)\sigma_z\delta\vec{\varphi}(y) = \left(\frac{d\vec{\varphi}^T}{dy}(-y)\sigma_z\delta\vec{\varphi}(y)\right)^T = \delta\vec{\varphi}^T(-y)\sigma_z\frac{d\vec{\varphi}}{dy}(-y)\,, \tag{1.104}$$

and performing the change of variable $y \to -y$, we obtain

$$\int_{-\tilde{W}}^{\tilde{W}} dy \frac{d\vec{\varphi}^T}{dy}(-y)\sigma_z\delta\vec{\varphi}^T(-y) = \int_{-\tilde{W}}^{\tilde{W}} dy \delta\vec{\varphi}^T(-y)\sigma_z\frac{d\vec{\varphi}}{dy}(y)\,. \tag{1.105}$$

In conclusion, the left-hand side results:

$$2\int_{-\tilde{W}}^{\tilde{W}} dy \delta\vec{\varphi}^T(-y)\sigma_z\frac{d\vec{\varphi}}{dy}(y)\,. \tag{1.106}$$

With analogous considerations we obtain, on the right-hand side,

$$\int_{-\tilde{W}}^{\tilde{W}} dy \delta\vec{\varphi}^T(-y)h(y)\sigma_x\vec{\varphi}(y) + \int_{-\tilde{W}}^{\tilde{W}} dy \vec{\varphi}^T(-y)h(y)\sigma_x\delta\vec{\varphi}(y) = 2\int_{-\tilde{W}}^{\tilde{W}} dy \delta\vec{\varphi}^T(-y)h(y)\sigma_x\vec{\varphi}(y)\,, \tag{1.107}$$

and

$$\int_{-\tilde{W}}^{\tilde{W}} dy \delta\vec{\varphi}^T(-y)k_x\vec{\varphi}(y) + \int_{-\tilde{W}}^{\tilde{W}} dy \vec{\varphi}^T(-y)k_x\delta\vec{\varphi}(y) = 2\int_{-\tilde{W}}^{\tilde{W}} dy \delta\vec{\varphi}^T(-y)k_x\vec{\varphi}(y)\,. \tag{1.108}$$

Putting together Eq. (1.106) and the right-hand side of Eq. (1.107) and Eq. (1.108), we obtain

$$2\int_{-\tilde{W}}^{\tilde{W}} dy\, \delta\vec{\varphi}^T(-y)\left[\sigma_z\frac{d\vec{\varphi}}{dy}(y) - (h(y)\sigma_x + k_x)\,\vec{\varphi}(y)\right]\vec{\varphi}(y)\,, \tag{1.109}$$

that vanishes because of the first of Eqs. (1.80) and the arbitrarity of $\delta\vec{\varphi}^T(-y)$. The remaining terms on the right-hand side verify, thus,

$$\int_{-\tilde{W}}^{\tilde{W}} dy\vec{\varphi}^T(-y)\delta h(y)\sigma_x\vec{\varphi}(y) = -\int_{-\tilde{W}}^{\tilde{W}} dy\vec{\varphi}^T(-y)\delta k_x\sigma_x\vec{\varphi}(y)\,, \tag{1.110}$$

from which Eq. (1.96) is immediately deduced.
The group velocity v_x^g in the x direction is obtained in the special case of an energy shift and is given by

$$v_x^g \equiv \frac{\delta E}{\delta k_x} = v_F\frac{\int_{-\tilde{W}}^{\tilde{W}}\mathrm{d}y\,\vec{\varphi}^T_{k_x}(-y)\vec{\varphi}_{k_x}(y)}{\int_{-\tilde{W}}^{\tilde{W}}\mathrm{d}y\,\vec{\varphi}^T_{k_x}(-y)\sigma_x\vec{\varphi}_{k_x}(y)}\,. \tag{1.111}$$

The velocity defined as above has a clear physical interpretation for real modes, for which it is real; however also complex group velocities can provide interesting information in many physical systems (see *e.g.* [58]).
At an EP, $\int_{-\tilde{W}}^{\tilde{W}}\mathrm{d}y\,\vec{\varphi}^T_{k_x}(-y)\vec{\varphi}_{k_x}(y)$ vanishes for some k_x and in the neighborhood of an EP corresponding to the eigenvalue k_x^{EP} we find

$$\delta E \cong \frac{(k_x - k_x^{EP})^2}{2\mu}, \quad \mu = \frac{1}{v_F}\frac{\int_{-\tilde{W}}^{\tilde{W}}\mathrm{d}y\,\vec{\varphi}^T_{k_x}(-y)\sigma_x\vec{\varphi}_{k_x}(y)}{\frac{\delta}{\delta k_x}\int_{-\tilde{W}}^{\tilde{W}}\mathrm{d}y\,\vec{\varphi}^T_{k_x}(-y)\vec{\varphi}_{k_x}(y)}\,. \tag{1.112}$$

This is nothing but the well known square root behavior, in the neighborhood of an EP [50, 51], of two coalescing eigenvalues as a function of the external parameters (see the inset (a) of Fig. 1.17). Near an EP we can then factorize the Hilbert space as the product of the $2d$ space of the collapsing eigenfunctions, for which the k_x's rapidly change with a small shift in E (fast modes), and the span of the other modes (slow modes), which can be assumed as fixed in the neighbourhood of the EP. Here we are assuming that eigenfunctions associated to different exceptional points do not mix; in the considered numerical examples

we checked that this assumption is indeed true. Thus:

$$\begin{pmatrix} \vec{\varphi}_{k_x^{(1)}} \\ \vec{\varphi}_{k_x^{(2)}} \end{pmatrix} \approx R \begin{pmatrix} \vec{\varphi}_+ \\ \vec{\varphi}_- \end{pmatrix} , \tag{1.113}$$

where $k_x^{(1)}, k_x^{(2)}$ are the two coalescing eigenvalues, $R = (r \otimes I)$, with r a 2×2 matrix and I the 2×2 identity matrix, and $\vec{\varphi}_\pm$ are the two initial states. Notice that if the difference between one or more eigenvalues and the coalescing ones is $\delta k_x \lesssim \mu$, they can mix together. It turns out that if they are quasi-degenerate with the coalescing eigenmodes ($\delta k_x \ll \mu$) the mixing between them is just a rotation, that is irrelevant for the features that we are going to describe. As long as we are not at the EP, we can choose the normalization $\int_{-\tilde{W}}^{\tilde{W}} \mathrm{d}y \vec{\varphi}^T_{k'_x}(-y)\vec{\varphi}_{k_x}(y) = \delta_{k_x k'_x}$; taking into account Eq. (1.113) this implies

$$\int_{-\tilde{W}}^{\tilde{W}} \mathrm{d}y \begin{pmatrix} \vec{\varphi}_{k_x^{(1)}}(y) \\ \vec{\varphi}_{k_x^{(2)}}(y) \end{pmatrix}^T \begin{pmatrix} \vec{\varphi}_{k_x^{(1)}}(y) \\ \vec{\varphi}_{k_x^{(2)}}(y) \end{pmatrix} = \int_{-\tilde{W}}^{\tilde{W}} \mathrm{d}y \begin{pmatrix} \vec{\varphi}_+(y) \\ \vec{\varphi}_-(y) \end{pmatrix}^T \begin{pmatrix} \vec{\varphi}_+(y) \\ \vec{\varphi}_-(y) \end{pmatrix} = \int_{-\tilde{W}}^{\tilde{W}} \mathrm{d}y \begin{pmatrix} \vec{\varphi}_+(y) \\ \vec{\varphi}_-(y) \end{pmatrix}^T RR^T \begin{pmatrix} \vec{\varphi}_+(y) \\ \vec{\varphi}_-(y) \end{pmatrix} , \tag{1.114}$$

so that $RR^T = \mathrm{I}$. For the sake of simplicity, in the following we restrict to the case of $\delta h = -\delta E/v_F$ and EPs on the real axis. The qualitative results obtained are nevertheless of general validity. Before the EP is reached, the group velocities of the coalescing real eigenmodes are opposite in sign, as shown by Eq. (1.112) and indicated by the subscript $\pm$ in Eq. (1.113), and from Eqs. (1.86) it follows that $R^* = (\sigma_z \otimes \mathrm{I})R(\sigma_z \otimes \mathrm{I})$. Indeed, because of the normalization chosen, Eq. (1.86) can be written as

$$\vec{\varphi}^*_{k_x^*}(y) = \epsilon_{k_x}\sigma_x\vec{\varphi}^*_{k_x}(-y) , \tag{1.115}$$

with $\epsilon_{k_x} = \pm 1$, and if k_x is real, we have

$$v_x^g = \frac{v_F\epsilon_{k_x}}{\int_{-\tilde{W}}^{\tilde{W}} dy\, \vec{\varphi}^\dagger_{k_x}(y)\vec{\varphi}_{k_x}(y)} . \tag{1.116}$$

Since the denominator in the right-hand side of Eq. (1.116) is positive, $\epsilon_{k_x} = \mathrm{sgn}(v_x^g)$. In the hypothesis that $k_x^{(1)}$ is the wave vector associated with the

positive group velocity, by taking the complex conjugate of Eq. (1.113) and by using Eq. (1.86), we obtain

$$\begin{aligned}(\mathrm{I}\otimes\sigma_x)(\sigma_z\otimes\mathrm{I})\begin{pmatrix}\vec{\varphi}_{k_x^{(1)}}(-y)\\ \vec{\varphi}_{k_x^{(2)}}(-y)\end{pmatrix} = R^*(\mathrm{I}\otimes\sigma_x)(\sigma_z\otimes\mathrm{I})\begin{pmatrix}\vec{\varphi}_{+}(-y)\\ \vec{\varphi}_{-}(-y)\end{pmatrix} = \\ (I\otimes\sigma_x)R^*(\sigma_z\otimes\mathrm{I})\begin{pmatrix}\vec{\varphi}_{+}(-y)\\ \vec{\varphi}_{-}(-y)\end{pmatrix},\end{aligned} \tag{1.117}$$

namely

$$\begin{pmatrix}\vec{\varphi}_{k_x^{(1)}}(-y)\\ \vec{\varphi}_{k_x^{(2)}}(-y)\end{pmatrix} = (\sigma_z\otimes\mathrm{I})R^*(\sigma_z\otimes\mathrm{I})\begin{pmatrix}\vec{\varphi}_{+}(-y)\\ \vec{\varphi}_{-}(-y)\end{pmatrix}. \tag{1.118}$$

Since R is independent of y, by comparing Eq. (1.118) and Eq. (1.113), we obtain the result.
After the EP is crossed, the eigenvalues, as well as $\delta E/\delta k_x$, become complex conjugate and from Eqs. (1.88) it follows that $R^* = \pm(\sigma_x\otimes\mathrm{I})R(\sigma_z\otimes\mathrm{I})$. Indeed, with passages analogous to the previous ones and taking into account that $\epsilon_{k_x^*} = \epsilon_{k_x}$, we find the equation

$$\epsilon_{k_x}\begin{pmatrix}\vec{\varphi}_{k_x^{(2)}}(-y)\\ \vec{\varphi}_{k_x^{(1)}}(-y)\end{pmatrix} = R^*(\sigma_z\otimes\mathrm{I})\begin{pmatrix}\vec{\varphi}_{+}(-y)\\ \vec{\varphi}_{-}(-y)\end{pmatrix}, \tag{1.119}$$

namely

$$\begin{pmatrix}\vec{\varphi}_{k_x^{(1)}}(-y)\\ \vec{\varphi}_{k_x^{(2)}}(-y)\end{pmatrix} = \epsilon_{k_x}(\sigma_x\otimes\mathrm{I})R^*(\sigma_z\otimes\mathrm{I})\begin{pmatrix}\vec{\varphi}_{+}(-y)\\ \vec{\varphi}_{-}(-y)\end{pmatrix}. \tag{1.120}$$

We obtain the result by comparing Eq. (1.120) and Eq. (1.113).
By taking into account the properties of the matrix R and by relaxing the normalization condition, we can parametrize R as follows:

$$R \sim (\mathrm{I} + e^{i\theta}\sigma_y)\otimes\mathrm{I}. \tag{1.121}$$

The domain of definition of the parameter θ is $]\infty i, 0i]\cup[0,\pi]\cup[\pi+0i, \pi+\infty i[$. The k_x values are real if $\mathrm{Im}\,\theta$ is different from 0 and complex if θ is real; the larger $\mathrm{Im}(\theta)$ the further apart the modes $k_x^{(1,2)}$ are. When $\theta = 0$ the eigenfunctions $\vec{\varphi}_{k_x^{(1,2)}}$ are linearly dependent, so this value corresponds to an

exceptional point. We rewrite Eq. (1.112) in terms of the parameter θ in the simplest case in which the term $\Delta \equiv \int_{-\tilde{W}}^{\tilde{W}} \mathrm{d}y \vec{\varphi}_+(-y)^T \sigma_x \vec{\varphi}_-(y)$, which appears in μ, is negligible

$$\begin{cases} k_x^{(1,2)} \approx k_x^0 + 2\mu \dfrac{(v_+^{-1} + v_-^{-1})\cos\theta \mp i(v_+^{-1} - v_-^{-1})\sin\theta}{(v_+^{-1} - v_-^{-1})^2} \\ E \approx E_0 - \dfrac{4\mu}{(v_+^{-1} - v_-^{-1})^2}\cos\theta\,, \end{cases} \tag{1.122}$$

where k_x^0 and E_0 are constants and $v_\pm$ are the group velocities associated to the eigenfunctions $\vec{\varphi}_\pm$. The condition $\Delta \approx 0$ is found for example when one eigenfunction is localized around the minima and the other around the maxima of the potential. The approximate Eq. (1.122) is accurate only in a neighborhood of the EP with $\theta \approx 0$ but, if μ is much less than the energy scale in which the Hilbert space factorization remains valid, then the value $\theta = \pi$ of Eq. (1.121) corresponds actually to another EP, and the previous approximation is good in the whole interval $0 \leq \theta \leq \pi$. This happens when two real eigenvalues collide, become complex and then come back on the real axis, the two EPs being sufficiently close to each other. In this case Eq. (1.122) captures the whole out-of-axes "motion" of the eigenvalues. In Fig. 1.18 the results predicted by Eqs. (1.121) and (1.122) are checked against numerical data and the agreement appears to be excellent. After crossing both exceptional points, the eigenfunctions almost return to the starting ones; observe, moreover, that the energy scale of the phenomenon shown in Fig. 1.18 is of order $\approx 10^{-8} v_F/a$, to be compared with an analytical background of order $\approx 0.2 v_F/a$ (see the caption of Fig 1.18). These aspects make the numerical observation of the phenomenon extremely difficult, so that the effect of two very close EPs may be incorrectly interpreted as a mode-crossing.

1.10 Concluding remarks

In this chapter we have proposed a numerical method, based on the solution in the reciprocal space of the Dirac equation, which allows to perform a transport analysis of an armchair graphene ribbon in quite general conditions.

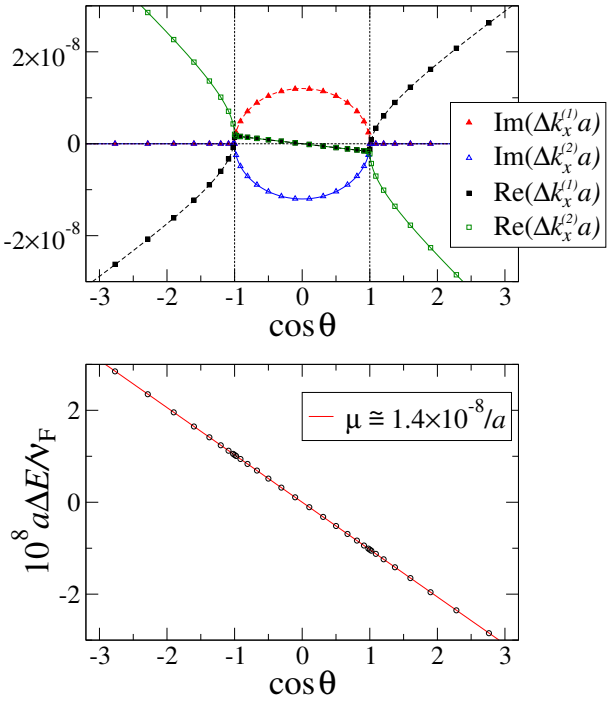

Figure 1.18: The momenta (*top*) $\Delta k_x^{(1,2)} \approx k_x^{(1,2)} - 0.199894795/a$ and the energy (*bottom*) $\Delta E \approx E + 0.200651930\, v_F/a$ of two coalescing modes as functions of $\cos\theta$, estimated from $(\det R - 2)/\sqrt{1 - \det R}$ (see Eqs. (1.113) and (1.121)), for the potential (1.95) with $\alpha = \pi/2$ and $\epsilon = -a\, E/v_F$. The lines in the upper graph follow the prediction (1.122): the asymptotic velocities $v_\pm$ are obtained by considering $\Delta E \gtrsim 2 \cdot 10^{-5}\, v_F/a$ and μ as obtained from the linear fit of the energy versus $\cos\theta$ shown in the bottom graph.

We have shown that this method allows, on one side, to directly solve the problems related to the standard finite difference solution of the Dirac equation and, on the other side, to outperform the approaches based on the Stacey discretization. Since this method will generally be used to solve the transport equation self-consistently with the Poisson equation, and thus inside an iterative procedure, its higher efficiency is likely to determine a considerable increase in the performance of graphene-oriented electrical simulators.
Moreover, we have pointed out a connection between properties of graphene and the theory of non-Hermitian Hamiltonians, by showing that armchair graphene nanoribbons provide the first example of a nondissipative system described by a $\mathcal{PT}$-symmetric non-Hermitian Hamiltonian. An aspect that certainly deserves further study is the effect of exceptional points on the transport properties of graphene nanoribbons in the presence of a potential that varies also in the longitudinal direction. Moreover it would be interesting to study more in depth the properties of complex eigenmodes and the effects of the non-vanishing transverse momentum.

Chapter 1. Simulation of transport in large area graphene samples

Chapter 2

Simulation of transport in bilayer graphene in the presence of the Integer Quantum Hall effect

The Integer Quantum Hall effect is a relevant behavior of two-dimensional disordered electron systems in a strong perpendicular magnetic field. Since its discovery in 1980 [25], it has been attracting significant interest, prompted, on the one hand, by the search for a satisfactory understanding of the physical phenomena involved, and, on the other hand, by the possibility of exploiting the precision in the conductance quantization to define the international standard for resistance in terms of fundamental constant alone.

Actually, there are three known distinct types of Integer Quantum Hall effect: beside the conventional effect characteristic of (non-intrinsically) two-dimensional semiconductor systems, a second and third type of behavior have been observed in monolayer [26] and bilayer [27] graphene, respectively. The discovery of the effect in graphene has paved the way for implementing a new metrological standard at relatively low magnetic fields and even at room tem-

perature, and it has opened the issue of the extent to which the effect in these novel materials shares the same explanation with that in ordinary two-dimensional electron systems.
In this chapter we discuss the numerical simulation of magnetotransport in bilayer graphene based on a single particle percolative model initially developed for conventional two-dimensional systems.
In order to make a close comparison with experimental data possible, we simulate experiments of scanning probe spectroscopy (SGS), a technique particularly suitable for the investigation of the Integer Quantum Hall effect, due to the possibility to perturb, with high spatial resolution, the localized states induced by the magnetic field.
The chapter is structured as follows. We start with some introductory remarks about the band structure of bilayer graphene in the presence of an orthogonal magnetic field, and we continue with a brief outline the phenomenology of the Integer Quantum Hall effect in four–terminal and two–terminal measurements and with a sketch of its explanation as a percolative phenomenon. Then, we introduce the semiclassical description of carrier dynamics, and, in this context, the random network model of Chalker and Coddington, that we assume as starting point of our simulation model. We discuss the latter in Sec. 2.4 together with the details of the numerical approach; finally we present the obtained results, comparing them with the experimental data.

2.1 The band structure of bilayer graphene

Bilayer graphene consists of two coupled monolayer graphene sheets. Here we focus on the Bernal-stacked configuration, in which two of the atoms lying on different sheets among the four unequivalent atoms in the unit cell are aligned. Similarly to the case of monolayer graphene, a nearest neighbours tight-binding description suitable for a transport analysis can be obtained by considering a basis of four Bloch sums built from $2p_z$ atomic orbitals. For the primitive lattice vectors we mantain the choice made in the first chapter for monolayer

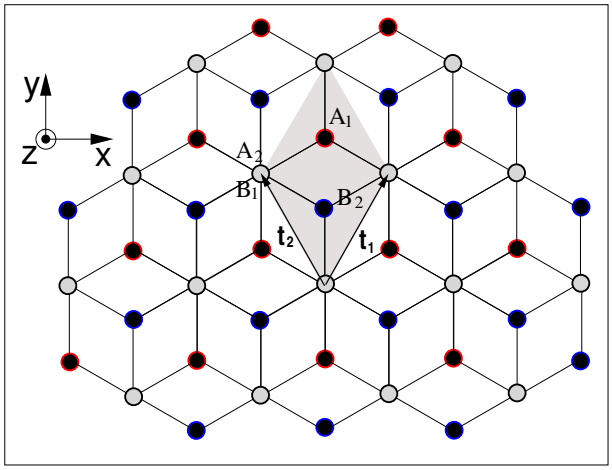

Figure 2.1: Crystal structure of Bernal-stacked bilayer graphene. The circles with blue (red) border represent carbon atoms lying on the upper (lower) layer. The gray circles correspond to the lattice sites where the atom on the upper layer and that on the lower one are superimposed. The shaded area indicates the unit cell corresponding to the primitive lattice vectors $\boldsymbol{t}_1$ and $\boldsymbol{t}_2$.

graphene:

$$\boldsymbol{t}_1 = \left(\frac{a}{2}, \frac{\sqrt{3}a}{2}\right) \; \boldsymbol{t}_2 = \left(-\frac{a}{2}, \frac{\sqrt{3}a}{2}\right) \tag{2.1}$$

The Hamiltonian reads [28]

$$H = \begin{pmatrix} \epsilon_{A1} & -\gamma_0 f(\boldsymbol{k}) & \gamma_4 f(\boldsymbol{k}) & -\gamma_3 f^*(\boldsymbol{k}) \\ -\gamma_0 f^*(\boldsymbol{k}) & \epsilon_{B1} & \gamma_1 & \gamma_4 f(\boldsymbol{k}) \\ \gamma_4 f^*(\boldsymbol{k}) & \gamma_1 & \epsilon_{A2} & -\gamma_0 f(\boldsymbol{k}) \\ -\gamma_3 f(\boldsymbol{k}) & \gamma_4 f^*(\boldsymbol{k}) & -\gamma_0 f^*(\boldsymbol{k}) & \epsilon_{B2} \end{pmatrix} \tag{2.2}$$

where, defining as $\phi_{A1}, \phi_{B1}, \phi_{A2}, \phi_{B2}$ the $2p_z$ orbitals for four the atoms in the primitive cell (see Fig. 2.1 for the nomenclature),

$$\begin{aligned} \gamma_0 &= -\langle \phi_{A1}|H|\phi_1\rangle = -\langle \phi_{A2}|H|\phi_{B2}\rangle \\ \gamma_1 &= \langle \phi_{A2}|H|\phi_{B1}\rangle \\ \gamma_3 &= -\langle \phi_{A1}|H|\phi_{B2}\rangle \\ \gamma_4 &= \langle \phi_{A1}|H|\phi_{A2}\rangle = \langle \phi_{B1}|H|\phi_{B2}\rangle\,; \end{aligned} \tag{2.3}$$

the function $f(\boldsymbol{k})$ is given by Eq. (1.8) and the ϵs are the onsite energies on the four atomic sites in the primitive cell.

As we are intersted in low-energy excitations, more directly involved in the conduction process, we can restrict ourself to the region of the first Brillouin zone near the two unequivalent Dirac points $\boldsymbol{K}$ and $\boldsymbol{K'}$, where the lowest conduction and valence bands, $E^+(\boldsymbol{k})$ and $E^-(\boldsymbol{k})$, are degenerate, and $E^\pm(\boldsymbol{K}) = E^\pm(\boldsymbol{K'}) = 0$. Developing to the first order the function $f(\boldsymbol{k})$ around $\boldsymbol{k} = \boldsymbol{K}^{(')}$ the Hamiltonian becomes:

$$H \approx \begin{pmatrix} \epsilon_{A1} & v\pi^\dagger & -v_4\pi^\dagger & v_3\pi \\ v\pi & \epsilon_{B1} & \gamma_1 & -v_4\pi^\dagger \\ -v_4\pi & \gamma_1 & \epsilon_{A2} & v\pi^\dagger \\ v_3\pi^\dagger & -v_4\pi & v\pi & \epsilon_{B2} \end{pmatrix}, \tag{2.4}$$

where $\pi = \pm p_x + ip_y$, $\pi^\dagger = \pm p_x - ip_y$, with the + sign referring to $\boldsymbol{K}$ and the $-$ to $\boldsymbol{K'}$, $p = |\boldsymbol{p}| = |\hbar(\boldsymbol{k} - \boldsymbol{K}^{(')})|$, $v = \sqrt{3}a\gamma_0/(2\hbar)$, $v_3 = \sqrt{3}a\gamma_3/(2\hbar)$, $v_4 = \sqrt{3}a\gamma_4/(2\hbar)$.

A further approximation we consider is to neglect the interlayer hopping terms

γ_3 and γ_4, that have only a minor relevance at low energies, and to neglect any asymmetry between layers, setting $\epsilon_{A1} = \epsilon_{A2} = \epsilon_{B1} = \epsilon_{B2} = 0$.
Finally, an effective Hamiltonian H_e accounting only for the lowest conduction and valence band can be obtained by restricting to the subspace of the Bloch sums associated only to the $A1$ and $B2$ atoms [28]:

$$H_e = -\frac{1}{2m}\begin{pmatrix} 0 & (\pi^\dagger)^2 \\ \pi^2 & 0 \end{pmatrix}, \tag{2.5}$$

with $m = \gamma_1/(2v^2)$. Within the considered approximations, bilayer graphene is thus characterized by zero gap and parabolic symmetric conduction and valence band, with the parameter m playing the role of an effective mass.
If an orthogonal magnetic field is present, the momentum operator $\boldsymbol{p} = -i\hbar\nabla$ has to be replaced by $\boldsymbol{p} = -i\hbar\nabla + e\boldsymbol{A}$, where $\boldsymbol{A}$ denotes the vector potential. If we choose the second Landau gauge and we refer to the valley at $\boldsymbol{k} = \boldsymbol{K}$, the vector potential is written as $\boldsymbol{A} = (0, -Bx, 0)$ and the π operator becomes $\pi = p_x + i(p_y - eBx)$.
In terms of the operators

$$\eta = \frac{1}{\sqrt{2eB\hbar}}\pi \,, \eta^\dagger = \frac{1}{\sqrt{2eB\hbar}}\pi^\dagger \,, \tag{2.6}$$

that fulfill $[\eta, \eta^\dagger] = 1$, the Hamiltonian can be rewritten as:

$$H_e = \hbar\omega_c \begin{pmatrix} 0 & (\eta^\dagger)^2 \\ \eta^2 & 0 \end{pmatrix}, \tag{2.7}$$

where we set $\omega_c = eB/m$. The square of $(1/\hbar\omega_c)H_e$ results

$$\frac{1}{(\hbar\omega_c)^2}H_e^2 = \begin{pmatrix} (\eta^\dagger)^2\eta^2 & 0 \\ 0 & \eta^2(\eta^\dagger)^2 \end{pmatrix} = \begin{pmatrix} \eta^\dagger(\eta\eta^{\dagger-1})\eta & 0 \\ 0 & \eta(1+\eta^\dagger\eta)\eta^\dagger \end{pmatrix} = \\ \begin{pmatrix} \eta^\dagger\eta(\eta^{\dagger-1}\eta - 1) & 0 \\ 0 & \eta\eta^\dagger(\eta\eta^\dagger + 1) \end{pmatrix} = \begin{pmatrix} \eta^\dagger\eta(\eta^{\dagger-1}\eta - 1) & 0 \\ 0 & (\eta^\dagger\eta + 1)(\eta^\dagger\eta + 2) \end{pmatrix}, \tag{2.8}$$

where we repeatedly used the commutation relation of η and $\eta^\dagger$.
The operator $\eta^\dagger\eta$ can be identified as a number operator and thus the eigenvalues of H_e^2 are of the form $E_n^2 = (\hbar\omega_c)^2\, n(n-1)$. As a consequence, the

eigenvalues of H_e, namely the Landau levels induced by the magnetic field, are:

$$E_n = \hbar\omega_c\sqrt{n(n-1)} \qquad n \in \mathbb{N}\,. \tag{2.9}$$

The same result is obtained with an analogous procedure at the Dirac point $\boldsymbol{K}'$. We notice that the absence of a gap entails the appearence of Landau levels for both electrons and holes; their symmetry with respect to $E = 0$ reflects the symmetry of the lowest energy conduction and valence band for vanishing magnetic field. With respect to those found in conventional two-dimensional gases, the Landau levels in bilayer graphene are not exactly equidistant; moreover, due to the the presence of two valleys, each level shows an additional double degeneracy besides that of spin. Finally, as it is apparent from Eq. (2.9), the lowest level $E = 0$ is eightfold degenerate. Since the Hamiltonian (2.5) is valid only for the low energy range $E \ll \gamma_1$, these results are a good approximation only for the Landau levels E_n for which $E_n \ll \gamma_1$.
In the following we will treat bilayer graphene in this effective mass approximation, neglecting any asymmetry between layers; in particular, we will consider negligible the corrections to the right side of Eq. (2.9) induced by the asymmetries that may be caused by the presence of an external potential.

2.2 The Integer Quantum Hall effect

The integer Quantum Hall effect (IQHE) appears in disordered two-dimensional carrier systems threaded by a strong ortghogonal magnetic field. Four-terminal measurements in these conditions reveal a step-like behavior of the transverse conductivity σ_{xy} as a function of the carrier density, with plateaus precisely quantized in units of e^2/h:

$$\sigma_{xy} = \nu\frac{e^2}{h}\,, \quad \nu \in \mathbb{N}\,. \tag{2.10}$$

Moreover, in correspondence of the plateaus of σ_{xy}, the longitudinal component of the conductivity tensor σ_{xx} vanishes, while it developes pulses in correspondence of the transitions between plateaus. The sequence of the plateau values and of the carrier densities for which the transitions occur differ between

ordinary 2DEG, monolayer and bilayer graphene, as a consequence of the differences in the degeneracy of the Landau levels and in their dipendence on the magnetic field intensity.

By varying the carrier density in two-terminal measurements, a different, "N–shaped", behavior of the conductance, resembling a combination of those of σ_{xy} and of σ_{xx} in the four terminal case, appears. The localization of the maxima and the minima of the conductance is strongly dependent on the shape of the sample, and, for rectangular samples, on their aspect ratio [29, 30].

The explanation of the effect as a percolative phenomenon relies on the existence of disorder-induced localized states at energies between the Landau levels. These states can not contribute to the transport, but pin the Fermi level when the carrier density is varied, allowing the formation of the plateaus. On the contrary, the states in a small neighborood of the Landau levels tend to be delocalized, so that, when the Fermi energy crosses a Landau level, the Hall conductivity undergoes a sudden increase toward the next plateau. The exact quantization of the plateaus can be understood in terms of the formation of *edge states*, extended states which freely propagate along the edges of the sample without suffering backscattering, each one contributing, thus, to the conductance with a conductance quantum e^2/h: each time the Fermi energy crosses a Landau level a new edge state starts propagating.

Despite single particle approaches has been in many respects successfull in providing percolative models for the IQHE, several experiments reporting on the regularity of fluctuations in the two-terminal conductance [31] and electronic compressibility [32, 33] suggest that many-body effects must also be considered for a complete understanding of transport in this regime. In detail, the aformentioned experimental results are explained by referring to the the formation of localized compressible islands due to the nonlinear screening effects induced by electron–electron interactions when the Fermi energy is in between two Landau energies. Transport via these states is only possible when the local potential is sufficient to overcome the Coulomb blockade, and the experimentally detected fluctuations are attributed to the periodic charging and discharging of these islands. As the linear screening regime is approached (this happens when the Fermi energy get close to a Landau level), the compressible regions delocalize,

and a metal–insulator transition occurs.
While the noninteracting model we will adopt cannot account for the charge rearrangements in compressible dots, for the resulting Coulomb blockade effects, and in general, for the evolution of the potential due to screening as the filling factor is varied, it has been pointed out by some authors [34–37] that the predicted critical behavior at the transition between plateaus may exhibit no differences with respect to that obtained with self-consistent Hartree–Fock calculations. In particular, the localization behavior of the wave functions has been found to be similar to that characteristic of a single–particle model.

2.3 The semiclassical picture

Let us consider a two-dimensional electron gas in the (x, y) plane, in the presence of an orthogonal magnetic field $\boldsymbol{B} = B\hat{z}$ and of an external random electrostatic potential $U(x, y)$. The electron wave functions $\Psi(x, y)$ can be represented in the basis of the eigenfunctions ψ_{nk} for $U = 0$. We choose the second Landau gauge, for which the vector potential is written $\boldsymbol{A} = (0, Bx, 0)$ and the ψ_{nk}'s have the form

$$\psi_{nk}(x, y) = \frac{1}{\sqrt{L_y}} e^{iky} \phi_n(x - X)\,, \tag{2.11}$$

where L_y is the length, in the y direction, of the rectangular box where the electrons are supposed to be confined, $X = -k\ell_B^2$ and $\ell_B = \sqrt{\hbar/eB}$ is the magnetic length. For our purposes we do not need the analytical expression of the ϕ_ns; we have only to take into account that they are significantly different from zero only in a neighborood of X of extension $\sim \ell_B$. As can be easily verified, X coincides with the expectation value of x on the states (2.11). It is convenient to introduce also the variable $Y = -i\ell_B^2(d/dX)$, the expectation value of which on the states (2.11) coincides with $\langle y \rangle$. The quantities X and Y can be thought of as a couple of canonically conjugated variables (they fullfill $[X, Y] = i\ell_B^2$), describing the position of the center of the classical cyclotron orbit, also called "guiding center" of the motion. They are referred to as the guiding center coordinates.

We consider an expansion of $\Psi(x,y)$ of the form

$$\Psi(x,y) = \sum_{n,X} C_n(X)\psi_{nX}(x,y)\,. \tag{2.12}$$

By substituting the previous expression into the Schrödinger equation

$$\left[H_0 + U(x,y)\right]\psi_{nX} = E\psi_{nX}\,, \tag{2.13}$$

where H_0 is the Hamiltonian with $U=0$, we obtain

$$\sum_{n'X'} \langle\psi_{nX}|U|\psi_{n'X'}\rangle C_{n'}(X') = (E-E_n)C_n(X) \tag{2.14}$$

We suppose the potential slowly varying on the length scale of the magnetic length, to such an extent that the mixing between the Landau levels can be neglected. After determining the spatial behavior of the wave functions it will be possible to obtain a quantitative constraint on $U(x,y)$ in order for the mixing between Landau levels to result negligible.
In this hypothesis we have to deal only with matrix elements of the form

$$\langle\psi_{nX}|U|\psi_{nX'}\rangle = \frac{1}{L_y}\int dxdy\phi_n(x-X)U(x,y)\phi_n(x-X')e^{iy(X-X')/\ell_B^2}\,. \tag{2.15}$$

In order to rewrite the left-hand side of Eq. (2.15) in a more expressive form, we notice that

$$\begin{aligned}\int dyU(x,y)e^{iy(X-X')/\ell_B^2} &= \int dy\sum_{m=0}^{+\infty}\frac{1}{m!}\frac{\partial^m U}{\partial y^m}(x,0)y^n e^{iy(X-X')/\ell_B^2} = \\ \sum_{m=0}^{+\infty}\frac{1}{m!}\frac{\partial^m U}{\partial y^m}(x,0)(-i\ell_B^2)^n &\int dy(\frac{-iy}{\ell_B^2})^n e^{iy(X-X')/\ell_B^2}\,,\end{aligned} \tag{2.16}$$

where we have expanded in power series the potential as a function of y around $y=0$. Using this result and transforming the sum over X' into an integral, we can write

$$\begin{aligned}\sum_{X'}\langle\psi_{nX}|U|\psi_{nX'}\rangle C_n(X') =& \frac{1}{2\pi\ell_B^2}\int dX'\int dx\phi_n(x-X)\phi_n(x-X')\times \\ &\sum_{m=0}^{+\infty}\frac{1}{m!}\frac{\partial^m U}{\partial y^m}(x,0)(-i\ell_B^2)^n\times \\ &\int dy(\frac{-iy}{\ell_B^2})^n e^{iy(X-X')/\ell_B^2}C_n(X')\,.\end{aligned} \tag{2.17}$$

Since the integral over X' is restricted only to a small neighborood of $X' = X$ and the functions $\phi_n(x - X)$ are localized within a distance $\sim \ell_B$ from X, we can approximate

$$\phi_n(x - X)\phi_n(x - X') \approx \phi_n^2(x - X) \approx \delta(x - X)\,, \tag{2.18}$$

and, thus,

$$\begin{aligned}
&\int dX' \int dx \phi_n(x - X)\phi_n(x - X') \sum_{m=0}^{+\infty} \frac{1}{m!} \frac{\partial^m U}{\partial y^m}(x, 0)(-i\ell_B^2)^n \times \\
&\int dy (\frac{-iy}{\ell_B^2})^n e^{iy(X-X')/\ell_B^2} \approx \\
&\int dX' \sum_{m=0}^{+\infty} \frac{1}{m!} \frac{\partial^m U}{\partial y^m}(X, 0)(-i\ell_B^2)^n \int dy (\frac{-iy}{\ell_B^2})^n e^{iy(X-X')/\ell_B^2} = \\
&\sum_{m=0}^{+\infty} \frac{1}{m!} \frac{\partial^m U}{\partial y^m}(X, 0)(-i\ell_B^2)^n \int dX' \int dy (\frac{-iy}{\ell_B^2})^n e^{iy(X-X')/\ell_B^2} C_n(X')
\end{aligned} \tag{2.19}$$

Finally, by considering that,

$$\begin{aligned}
&\int dX' \int dy (\frac{-iy}{\ell_B^2})^n e^{iy(X-X')/\ell_B^2} C(X') = \\
&\int dy (\frac{-iy}{\ell_B^2})^n e^{iyX/\ell_B^2} \int dX' C(X') e^{-iyX'/\ell_B^2} = 2\pi\ell_B^2 \frac{d^n C}{dX^n}(X)
\end{aligned} \tag{2.20}$$

we obtain for Eq. (2.14) the form

$$\sum_{m=0}^{+\infty} \frac{1}{m!} \frac{\partial^m U}{\partial y^m}(X, 0)(-i\ell_B^2)^n \frac{d^n C}{dX^n}(X) = (E - E_n)\, C(X) \tag{2.21}$$

or

$$U(X, Y(X))\, C(X) = (E - E_n)\, C(X)\,. \tag{2.22}$$

In the previous equation we have denoted with $U(\,\cdot\,, Y(X))$ the function of the operator Y corresponding to $U(\,\cdot\,, y)$. Thus Eq. (2.22) establishes the remarkable result that the energy of an electron with the guiding center in the position (X, Y) can be written as $E = E_n + U(X, Y)$. Furthermore, the guiding center of the motion follows a trajectory $X, Y(X)$ such that the value of the potential energy remain fixed at $E - E_n$, a constant value; in other words the guiding

center drifts along the equipotential lines with $U = E - E_n$.
Equipotential lines closed on themselves correspond to localized states. Depending on the behavior of U, a number of different localized states corresponding to the same value of E can be present, so that the degeneracy of the Landau states for $U = 0$ is lifted.
Close to the sample edges the confining potential tends to dominate over the disorder-induced fluctuations and extended states following nearly straight equipotential trajectories can form. An increase in the Fermi energy tends to push these trajectories towards the edges, without altering the contribution of these states to the conduction. These states represent nothing but the edges states we mentioned in Sec. 2.2.
These results allow to establish a more precise condition on the potential under which the mixing between defferent Landau levels can be considered negligible. Let us consider two states at the same total energy E but associated to adjacent Landau levels E_n and E_{n+1}. No substantial overlap between the wave functions occours if the spatial distance between the corresponding equipotential trajectories is much greater than the magnetic length. Thus, if $\boldsymbol{d}$ is the vector pointing orthogonally from an orbit to the other, it has to be $|d| \ll \ell_B$, and, from $|\nabla U||\boldsymbol{d}| = |(E - E_n) - (E - E_{n+1})| = |E_n - E_{n+1}|$, we deduce the condition $|\ell_B \nabla U| \ll |E_n - E_{n+1}|$. To obtain a condition valid for all the Landau levels, $|E_n - E_{n+1}|$ has to be replaced with $\min_n |E_n - E_{n+1}|$.
In order to evaluate the dependence on $E - E_n$ of the number of the localized states, we can consider the probability that a closed equipotential line with $U = E - E_n$ arises to be proportional to the value of the probability density function of the random potential $p(U)$ for $U = E - E_n$ [38]. In this approximation the local density of states ($LDOS$) can be written as

$$LDOS(E, \boldsymbol{r}) = \sum_n p(E - E_n)|\Psi_{n,E}(\boldsymbol{r})|^2 \tag{2.23}$$

Different approximations for $p(E - E_n)$ have been proposed in the literature; for example, it has been modeled as a Lorentzian [41], a Gaussian [39] or a semielliptic function [40].

2.4 The random network model

In the original version proposed by Chalker and Coddington [42], the random network model describes transport in a two-dimensional system orthogonally threaded by a strong magnetic field within the framework of the semiclassical view outlined in the previous section.
The basic idea is that during the transitions between plateaus the conduction is supported by tunnelling processes between localized states. As the states are confined in narrow strips following equipotential orbits, they tend to surround hills and valleys of the potential and get close to each other only in correspondence of the saddle points of the potential. Here tunnelling between the states can occur. The flow of a net current is caused by the formation of extended states, associated to paths connecting localized states that cross the sample. The quantum Hall effect is thus modeled as a percolative phenomenon, in which, for particular values of the energy, an insulator-metal phase transition occurs. In the model, the two-dimensional system is described as a regular network, with meshes corresponding to the localized current loops and nodes corresponding to the saddle points of the potential. The scattering at each node is described by means of a transmission matrix T, linking the complex amplitudes ζ_i, ζ_o of the waves (incident onto and reflected from the node, respectively) associated to one of the orbit to the corresponding amplitudes η_i, η_o associated to the other orbit (see Fig. 2.2):

$$\begin{pmatrix} \zeta_i \\ \zeta_o \end{pmatrix} = T \begin{pmatrix} \eta_i \\ \eta_o \end{pmatrix} \tag{2.24}$$

Before further discussing the model, it is worth noting some properties of the matrix T. We start from the condition imposed by the constraint ot current conservation:

$$|\zeta_i|^2 - |\zeta_o|^2 = |\eta_i|^2 - |\eta_o|^2 \,. \tag{2.25}$$

This equation can be rewritten as

$$(\zeta_i^*, \zeta_o^*) J \begin{pmatrix} \zeta_i \\ \zeta_o \end{pmatrix} = (\eta_i^*, \eta_o^*) J \begin{pmatrix} \eta_i \\ \eta_o \end{pmatrix} \,, \tag{2.26}$$

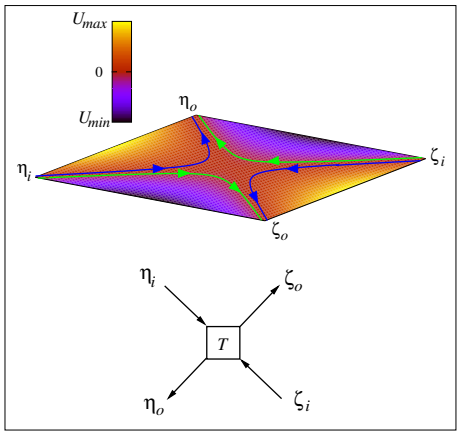

Figure 2.2: Top: equipotential orbits near the saddle point of the quadratic potential $U = x^2 - y^2$, to which the color map refers. The blue orbits are associated to a positive value of U, while the green ones correspond to a negative value. Bottom: description of the scattering at the saddle point by means of the transfer matrix

with $J = \mathrm{diag}(1, -1)$. Since the right hand side can be rewritten as

$$(\zeta_i^*, \zeta_o^*) T^\dagger J T \begin{pmatrix} \zeta_i \\ \zeta_o \end{pmatrix} , \tag{2.27}$$

and Eq. (2.26) has to be valid for all vectors $(\zeta_i, \zeta_o)^T$ we obtain the equation

$$J = T^\dagger J T \, . \tag{2.28}$$

Denoting as τ_{ij} the elements of T, we can write Eq. (2.28) as an equivalent system of four nonlinear equations:

$$\begin{cases} |\tau_{11}|^2 - |\tau_{21}|^2 = 1 \\ |\tau_{12}|^2 - |\tau_{22}|^2 = -1 \\ \tau_{11}\tau_{21}^* - \tau_{21}\tau_{22}^* = 0 \\ \tau_{11}^*\tau_{21} - \tau_{21}^*\tau_{22} = 0 \end{cases} ; \tag{2.29}$$

by rearranging it we obtain

$$\begin{cases} |\tau_{11}| = \sqrt{1+|\tau_{21}|^2} \\ |\tau_{12}| = \sqrt{|\tau_{22}|^2-1} \\ |\tau_{11}||\tau_{12}| = |\tau_{21}||\tau_{22}| \\ \phi_{11}-\phi_{12} = \phi_{21}-\phi_{22}\,, \end{cases} , \tag{2.30}$$

where the ϕ_{ij} indicate the phases of the corresponding τ_{ij}. Finally, by considering the first three equations in Eq. (2.30), we arrive to the relations $\tau_{22} = \tau_{11}$ and $\tau_{21} = \tau_{12}$, from which it is apparent that we can express the matrix T of the amplitude of the τ_{ij} in terms of a single parameter. For example, since $|\tau_{11}| \geq 1$, we can set $|\tau_{11}| = \cosh(\theta)$, so that

$$\mathsf{T} = \begin{pmatrix} \cosh(\theta) & \sinh(\theta) \\ \sinh(\theta) & \cosh(\theta) \end{pmatrix} , \tag{2.31}$$

and, denoting with φ_1, φ_2, φ_3, φ_4 four arbitrary phases,

$$T = \begin{pmatrix} e^{\varphi_3} & 0 \\ 0 & e^{\varphi_4} \end{pmatrix} \begin{pmatrix} \cosh(\theta) & \sinh(\theta) \\ \sinh(\theta) & \cosh(\theta) \end{pmatrix} \begin{pmatrix} e^{\varphi_1} & 0 \\ 0 & e^{\varphi_2} \end{pmatrix} . \tag{2.32}$$

In Fig. 2.3 a complete network is sketched. The squares correspond to the saddle points, while the arrows indicates the direction of the guiding center motion. The network corresponds to a regular pattern of maxima (+) and minima (−) of the potential separated by saddle points. The physical random spatial distribution of the saddle points is accounted for by treating the phase factors φ in Eq. (2.32) as independent random variables uniformly distributed in $[0, 2\pi]$. Two types of transmission matrices, $T = T(\theta)$ and $T' = T(\theta')$, are present, with the parameters θ and θ' linked via $\sinh(\theta)\sinh(\theta') = 1$. This implies that for θ varying from zero to infinity the behavior of the nodes associated to T gradually varies from a perfect transmission of the incident waves to a perfect reflection of them , while, conversely, the behavior of the nodes associated to T' varies gradually from perfect reflection to perfect transmission. Thus, for θ approaching zero and infinity the network decomposes into independent current loops surrounding (with opposite direction of rotation) the minima ($\theta \to 0$) or the maxima ($\theta \to \infty$) of the potential, mimicking the

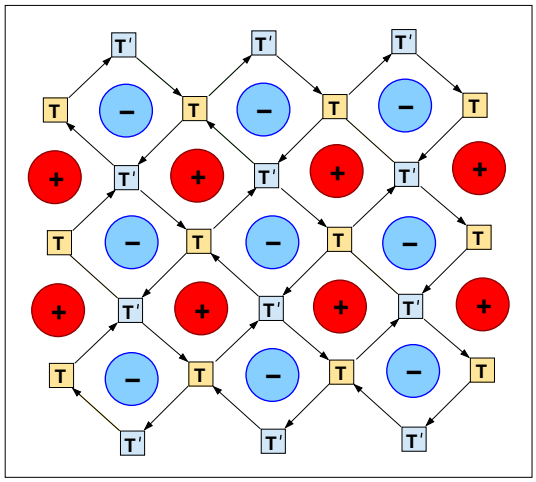

Figure 2.3: Sketch of a complete network: the arrows describe the drift of electrons around the hills (+) and valleys (-) of the potential, while the transfer matrices T and T' characterize tunnelling at the saddle points. Adapted from [43].

physical behavior of the localized states in the tails of a Landau level. These considerations suggest that θ can be regarded as a non-decreasing function of the electron energy.

Finally, let us consider the boundary conditions to be imposed at the edges of the network. At the entry and the exit of the network open boundary conditions are assumed, representing the connection with ideal semi-infinite leads. Concerning the transverse direction, if the size of the network is considered finite, the current flux has to be imposed parallel to the edges: this corresponds to substituting the nodes lying on the edges with a direct connection between the current paths beginning and ending on them. Instead, in order to treat networks infinitely extended in the transverse direction, periodic boundary conditions have to be imposed, by identifying each node lying on one edge with that lying in the correspondent position on the other edge.

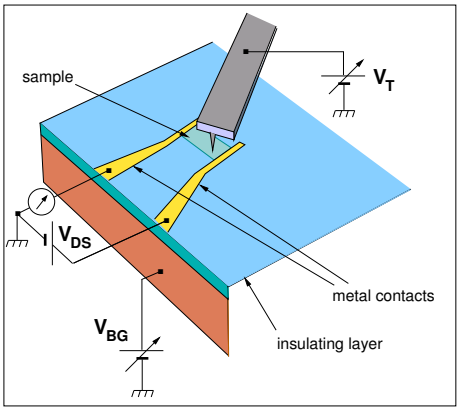

Figure 2.4: Sketch of a simplified SGM setup.

2.5 The simulation model

We start from the model of Chalker and Coddington, introducing a connection with some of the parameters that can be tuned in the setup of a SGS experiment.
In Fig. 2.4 a simplified experimental setup is sketched. In this technique a sharp conductive tip, biased at the voltage V_T, is scanned over the sample surface. The capacitive coupling between the tip and the sample induces local perturbations. A backgate (biased at the voltage V_{BG}) allows for an independent, almost uniform, change of the carrier density in the specimen. For each tip position, the conductance of the sample (biased at the voltage V_{SD}) is measured and compared with that measured in the absence of the tip. In this way it is possible to relate the variations in the global transport properties of the system to the perturbations affecting only small parts of it, and information about the distribution and the dynamics of the carrier can be inferred.
In our model, each θ_{ij} is trated as a function of the electron energy E and of the potential U_{ij} of the saddle point corresponding to the node (i, j). We

assume the functional dependence [43]

$$\theta_{ij}(E, U_{ij}) = \left(\theta_c + \frac{E - E_n - U_{ij}}{\gamma}\right) H\left(\theta_c + \frac{E - E_n - U_{ij}}{\gamma}\right), \tag{2.33}$$

obtained from the analytical result for the transmission probability through a saddle point [44], and which is valid in a neighborhood of the value θ_c for which the transmission probability equals 1/2. We have indicated with E_n the Landau energies (2.9) of the electron motion and with $H(x)$ the Heaviside function. The energy γ can be related to the behavior of the potential in a neighborhood of the saddle point; we assume it to be identical for all of the saddle points and we tune it to optimize the agreement with measurements. The potential U_{ij} can be thought of as the sum of a component $U_{ij}^{(0)}$, due to the impurities and to the imperfections of the material, and a perturbation δU_{ij}, induced by the effect of the back-gate and of the probe. As in [45], the values of the potentials $U_{ij}^{(0)}$ are randomly assigned, with a uniform distribution in an interval $[-\Delta E, \Delta E]$, while the values of the perturbation δU_{ij} is calculated, for each node, by numerically solving in δU_{ij} the equation

$$\begin{aligned}\rho_{ij} = & e \int_{-\infty}^{U_{ij}^{(0)}+\delta U_{ij}} LDOS_{ij}(E)\,[1 - f(E)]\,dE - \\ & e \int_{U_{ij}^{(0)}+\delta U_{ij}}^{\infty} LDOS_{ij}(E) f(E) dE\end{aligned} \tag{2.34}$$

where ρ_{ij} is the local value of charge density, e the modulus of the electron charge, $LDOS_{ij}(E)$ the density of states in the saddle point corresponding to the node (i, j), and $f(E)$ the Fermi-Dirac distribution function for the considered value of temperature and Fermi level. This, in turn, requires the calculation of ρ_{ij} and the knowledge of the function $LDOS_{ij}(E)$. Let us now discuss the approximations that we have used to model the density of states.

Following Ref. [41], in the case of a vanishing constant potential we model the density of states as a sum of Lorentzian-shaped peaks, centered at the Landau energies E_n; the half-width at half maximum of the Lorentzians, which quantifies the broadening of the Landau levels, is assumed to be independent of the energy and is left as a fitting parameter. In the presence of a non vanishing potential, we assume that the energy of the electronic states is locally shifted

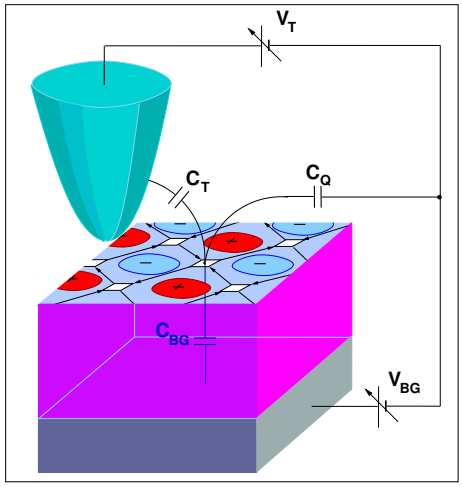

Figure 2.5: Illustration of the model used to link the random network model with some of the parameters that can be tuned in the setup of a scanning gate spectroscopy experiment. C_Q is the quantum capacitance (per unit area) at the considered saddle point.

by an amount equal to the value of the potential, so that we have

$$LDOS_{ij}(E) = LDOS(E - U_{ij}^{(0)} - \delta U_{ij})\,. \tag{2.35}$$

This semiclassical approximation is acceptable if the potential is slowly varying over a length scale of the order of the lattice constant. Moreover, from Eq. (2.23) we see that Eq. (2.35) implies a zeroth-order approximation for the square modulus of the wave function in the saddle points as a function of the energy, namely that in the saddle points $|\Psi_{n,E}|^2$ is independent of E.
Concerning the calculation of ρ_{ij}, we set

$$\rho_{ij} = \rho_{ij}^{(0)} + \delta\rho_{ij}\,; \tag{2.36}$$

here $\rho_{ij}^{(0)}$ is the charge density induced by the term $U_{ij}^{(0)}$ alone and can be evaluated from the Eq. (2.34) with $\delta U_{ij} = 0$, while $\delta\rho_{ij}$ is the perturbation due

to the term δU_{ij}.
We can express $\delta\rho_{ij}$ as a function of the voltages applied to the back-gate and to the probe:

$$\delta\rho_{ij} = C_{BG}\left(\frac{\delta U_{ij}}{-e} - V_{BG}\right) + C_{T,ij}\left(\frac{\delta U_{ij}}{-e} - V_T\right). \tag{2.37}$$

We indicated with C_{BG} and $C_{T,ij}$ the values for the considered node of the capacitances per unit area between the back-gate and the graphene, and the probe and the graphene, respectively. Coupling this relation with Eq. (2.34), we obtain the system

$$\begin{cases} \delta\rho_{ij} &= (C_{BG} + C_{T,ij})\,\dfrac{\delta U_{ij}}{-e} - (C_{BG}V_{BG} + C_{T,ij}V_T) \\ \rho_{ij}^{(0)} + \delta\rho_{ij} &= e\displaystyle\int_{-\infty}^{U_{ij}^{(0)}+\delta U_{ij}} LDOS(E - U_{ij}^{(0)} - \delta U_{ij})\,[1 - f(E)]\,dE \\ & \quad -e\displaystyle\int_{U_{ij}^{(0)}+\delta U_{ij}}^{\infty} LDOS(E - U_{ij}^{(0)} - \delta U_{ij}) f(E) dE \end{cases} \cdot \tag{2.38}$$

Substituting the expression for $\delta\rho_{ij}$ from the first equation into the second one, we obtain a nonlinear equation in δU_{ij}, which we solve numerically.
In the modeling of the coupling between the probe and the graphene we consider a capacitance per unit area $C_{T,ij}$ different for each node; furthermore we allow the elements of the C_T matrix to vary, in order to describe the dependence on the position of the probe tip over the flake. Self-consistent calculations [46] showed that the charge density induced by the probe in bilayer graphene can be modeled by the sum of two two-dimensional Lorentzians, the amplitude of which is linearly dependent on V_T. Therefore, the coupling between the probe and the flake can be described by a linear capacitance per unit area, with the same spatial dependence. In order to obtain more easily interpretable results, in our simulations we consider only the narrower and higher of the two Lorentzians, thus neglecting long-range effects, mainly due to the wider and lower one. In particular, introducing a reference frame (x, y) and defining (x_i, y_j) the coordinates of the node (i, j), we set $C_{T,ij}(\bar{x}, \bar{y}) = \Lambda(x_i - \bar{x}, y_i - \bar{y})$, where $\Lambda(x, y)$ is a two-dimensional Lorentzian, and $\bar{x}$ and $\bar{y}$ account for the

position of the probe tip.
The conductance through the network is calculated in the Landauer-Büttiker framework as

$$G = \frac{1}{V_{SD}} \frac{g_s g_v e}{h} \int_{-\infty}^{\infty} \mathrm{Tr}\left(tt^{\dagger}\right) \left[f^{(S)}(E) - f^{(D)}(E)\right] dE\,, \tag{2.39}$$

where t indicates the transmission matrix, $f^{(S)}(E)$ and $f^{(D)}(E)$ indicate, respectively, the Fermi-Dirac distribution function at the source and drain contacts, and $g_s = g_v = 2$ account for the spin and valley degeneracy of the electrons. In order to compute the transmission matrix, we subdivide the network into transverse slices, each one including two columns of adjacent nodes [42,43]. The transfer matrix T associated to each slice is the product of the transfer matrices associated to each column of nodes and satisfy

$$\begin{pmatrix} \zeta_{o,1}^{(r)} \\ \zeta_{i,1}^{(r)} \\ \vdots \\ \zeta_{o,M}^{(r)} \\ \zeta_{i,M}^{(r)} \end{pmatrix} = T \begin{pmatrix} \eta_{i,1}^{(l)} \\ \eta_{o,1}^{(l)} \\ \vdots \\ \eta_{i,M}^{(l)} \\ \eta_{o,M}^{(l)} \end{pmatrix}\,, \tag{2.40}$$

where we denoted with $\eta_{i,n}^{(l)}$ and $\eta_{o,n}^{(l)}$ the complex amplitudes entering and exiting from the left the $n-$th node of the column on the input of the slice; analogously, $\zeta_{i,n}^{(r)}$ and $\zeta_{o,n}^{(r)}$ denote the complex amplitudes entering and exiting from the right the $n-$th node of the column on the exit of the slice, while the subscript M indicates the number of nodes on each column.
To guarantee the stability of the numerical method, instead of computing the global transfer matrix as the product of the transfer matrices of the sigle slices, we substitute each transfer matrix with the corresponding scattering matrix and we use a recursive approach to compose them. Starting from the transfer matrix T of the generical slice we compute the corresponding scattering matrix as follows. First, we apply to T the transformation

$$T \longrightarrow \tilde{T} = U^{\dagger} T U\,, \tag{2.41}$$

where U is the permutation matrix that implements the reordering

$$(\eta_{i,1}^{(l)}, \eta_{o,1}^{(l)}, \cdots, \eta_{i,M}^{(l)}, \eta_{o,M}^{(l)})^T \rightarrow (\eta_{i,1}^{(l)}, \cdots, \eta_{i,M}^{(l)}, \eta_{o,1}^{(l)}, \cdots, \eta_{o,M}^{(l)})^T\,, \tag{2.42}$$

or, equivalently,

$$(\zeta_{o,1}^{(r)}, \zeta_{i,1}^{(r)}, \cdots, \zeta_{o,M}^{(r)}, \zeta_{i,M}^{(r)})^T \rightarrow (\zeta_{o,1}^{(r)}, \cdots, \zeta_{o,M}^{(r)}, \zeta_{i,1}^{(r)}, \cdots, \zeta_{i,M}^{(r)})^T . \tag{2.43}$$

Therefore, $\tilde{T}$ verifies

$$\begin{pmatrix} \boldsymbol{\zeta}_i^{(r)} \\ \boldsymbol{\zeta}_o^{(r)} \end{pmatrix} = \tilde{T} \begin{pmatrix} \boldsymbol{\eta}_i^{(l)} \\ \boldsymbol{\eta}_o^{(l)} \end{pmatrix} = \begin{pmatrix} \boldsymbol{\tau}_{11} & \boldsymbol{\tau}_{12} \\ \boldsymbol{\tau}_{21} & \boldsymbol{\tau}_{22} \end{pmatrix} \begin{pmatrix} \boldsymbol{\eta}_i^{(l)} \\ \boldsymbol{\eta}_o^{(l)} \end{pmatrix} , \tag{2.44}$$

with $\boldsymbol{\zeta}_\alpha^{(r)} = (\zeta_{\alpha,1}^{(r)}, \zeta_{\alpha,2}^{(r)}, \cdots \zeta_{\alpha,M}^{(r)})^T$ and $\boldsymbol{\eta}_\alpha^{(l)} = (\zeta_{\alpha,1}^{(l)}, \zeta_{\alpha,2}^{(l)}, \cdots \zeta_{\alpha,M}^{(l)})^T$, $\alpha = i, o$. Then we can stightforwardly rewrite the subblocks of the corresponding scattering matrix S, defined by

$$\begin{pmatrix} \boldsymbol{\eta}_o^{(l)} \\ \boldsymbol{\zeta}_o^{(r)} \end{pmatrix} = S \begin{pmatrix} \boldsymbol{\eta}_i^{(l)} \\ \boldsymbol{\zeta}_i^{(r)} \end{pmatrix} = \begin{pmatrix} \boldsymbol{r} & \boldsymbol{t}' \\ \boldsymbol{t} & \boldsymbol{r}' \end{pmatrix} \begin{pmatrix} \boldsymbol{\eta}_i^{(l)} \\ \boldsymbol{\zeta}_i^{(r)} \end{pmatrix} , \tag{2.45}$$

in terms of the subblocks of the transfer matrix as

$$\begin{aligned} \boldsymbol{r} &= -\boldsymbol{\tau}_{22}^{-1}\boldsymbol{\tau}_{12} , \quad & \boldsymbol{t} &= \boldsymbol{\tau}_{11} - \boldsymbol{\tau}_{21}\boldsymbol{\tau}_{22}^{-1}\boldsymbol{\tau}_{12} \\ \boldsymbol{r}' &= -\boldsymbol{\tau}_{21}\boldsymbol{\tau}_{22}^{-1} , \quad & \boldsymbol{t}' &= -\boldsymbol{\tau}_{22}^{-1} . \end{aligned} \tag{2.46}$$

At the end of the procedure for the composition of the partial scattering matrices we obtain the scattering matrix of the overall network, from which we extract t.

2.6 Mapping of local currents

In this section we outline the method we used in order to obtain a map of the current inside the network.

From Eq. (2.24) it follows that the net current flowing through the node is proportional to $\Delta = |\eta_i|^2 - |\eta_o|^2 = |\zeta_o|^2 - |\zeta_i|^2$; in order to obtain a map of the local currents in the network, we have to evaluate this quantity for each node. In general, the set of values of Δ for the overall network is a function of the vector $\boldsymbol{\eta}_i^{(in)}$ of the η_i's entering the network from the edge corresponding to the source contact (which we refer to as the input of the network) and of the vector $\boldsymbol{\zeta}_i^{(out)}$ of the ζ_i's entering from the edge corresponding to the drain contact (which we refer to as the output of the network). In our simulations we

have set $\boldsymbol{\eta}_i^{(in)} = \mathbf{c}$ and $\boldsymbol{\zeta}_i^{(out)} = \mathbf{0}$, where we have indicated with $\mathbf{c}$ the constant vector with components of value $c \in \mathbb{R}$.
In order to compute the complex amplitudes at the entrance or exit of each node and thus the corresponding value of Δ, as in the calculation of the conductance we subdivide the network into slices incuding two columns of adjacent nodes and we use the scattering matrix method. The calculation can be limited to the set of amplitudes η_i, η_o corresponding to the nodes of the entrance side of each slice, from which the value of Δ for these nodes can be directly computed. The value of Δ for the nodes on the exit side of the slice can instead be evaluated observing that the set of the amplitudes ζ_i, ζ_o corresponding to these nodes coincides with the set of amplitudes η_i, η_o on the entrance side of the following slice.
For each slice we split the overall network into two parts: the first one including all the slices from the input to the slice preceding the considered one, and the second one including all the remaining slices, from the considered one to the output. We evaluate the scattering matrix of both subnetworks. The scattering matrix of the first one relates $\boldsymbol{\eta}_i^{(in)}$ to the amplitudes at the entrance of the considered slice, while the scattering matrix of the second one relates these amplitudes to $\boldsymbol{\zeta}_i^{(out)}$. Therefore, these relations constitute two coupled sets of linear equations, which allow to compute all of the complex amplitudes at the entrance of the slice, as a function of $\boldsymbol{\eta}_i^{(in)}$ and $\boldsymbol{\zeta}_i^{(out)}$.

2.7 Results

We refer to the SGM experiments described in Ref. [49]. The measurements are performed on a bilayer graphene flake of dimensions $\approx 2.5 \times 6$ μm^2, deposited onto an higly doped Si substrare capped with a 300 nm thick SiO_2 layer. The sample is cooled at a temperature $T \approx 8$ K and orthogonally threaded by a magnetic field of intensity $B = 6.2$ T. Since the flake has a trapezoidal shape, we consider a rectangular network with aspect ratio equal to that of the largest rectangle that can be inscribed within the flake between the source and drain contatcts. We restrict the simulation to a neighborood of the transition associated to the filling of the $n = 1$ Landau level, with $E_1 \simeq 0.03$ eV. It is worth

noticing that $E_1 \simeq \gamma_1/10$, therefore the low energy approximation (2.9) is justified. For the coupling capacitance between the backgate and the flake we assume the geometrical capacitance of the corresponding parallel plate capacitor: $C_{BG} = 1.15 \times 10^{-8}$ F/cm^{-2}. Concerning the coupling capacitance between the probe and the flake, for which, as already specified, we assume a Lorentzian spatial dependence, we use a half width at half maximum of 50 nm and a peak value of $\sim 10^{-9}$ F/cm^{-2} [46]. The mesh size of the network (corresponding to the average spatial separation between saddle points) and the dispersion of the fluctuation of the potential associated to the nodes have been tuned in order to optimize the agreement with the measurements. The full width at half maximum Γ of the Lorentzians, quantifying the broadening of the Landau levels in our approximation for the $LDOS$, has also been, independently, tuned. The results presented refer to a standard deviation of the potential fluctuation of $\sigma_U \sim 10^{-2}\ eV \sim \Gamma$, and to an average distance between saddle points of 60 nm. These values are in reasonable agreement with the estimates provided in the literature [47, 48]. In the Fig. 2.6 we show the comparison between the measured and simulated behavior of the conductance as a function of V_{BG} in the absence of the probe. The comparison is intended as restricted to the marked region in the panel of the experimental data, where the contribute of the other Landau levels is not essential. At low values of V_{BG}, corresponding, on average, to low values of the θ_{ij}'s, the transmission is suppressed, as a result of the low tunnelling probability through the network nodes. At high values of V_{BG}, corresponding, on average, to high values of the θ_{ij}'s, the transmission tends to stabilize toward the value $4e^2/h$, indicating that a single mode is perfectly transmitted. At intermediate values of V_{BG}, when, on average, the θ_{ij}'s are nearer to the critical value θ_c, the conduction is sustained by the increased probability of tunnelling at the nodes. The lower panels show three maps of the modulus of the current density, corresponding to the values of the conductance indicated by the arrows. As expected, the current density tends to spread out through the flake as V_{BG} is increased from lower to intermediate values, while an edge state (associated to a perfectly transmitted state) tends to develop on the left for high values of V_{BG}.

In Fig. 2.7 we report the comparison between simulated and measured maps of

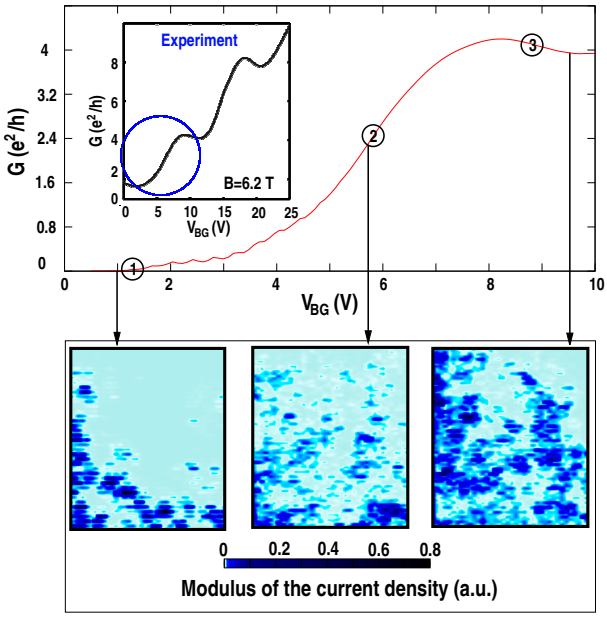

Figure 2.6: Upper panel: Simulated conductance as a function of backgate voltage around the $n = 1$ Landau level. The inset shows the results of the measurements [49]. Lower panel: maps of the modulus of the current density corresponding to the values of the conductance indicated by the arrows; the current injection is from the lower side of the images.

the conductance variation as a function of the probe position over the flake. In each point of the maps we indicated the value of the difference between the conductance obtained with the probe placed at the corresponding point over the sample and the conductance obtained in the absence of the probe. The probe is biased at $V_T = 1$ V, and three values of V_{BG} are considered, corresponding to the values for which the current maps have been obtained. Since the potential landscape for the simulations has been randomly created, there cannot be a one-to-one correspondence with the experimental data (which are relative to a different random potential). The data should therefore be compared from the

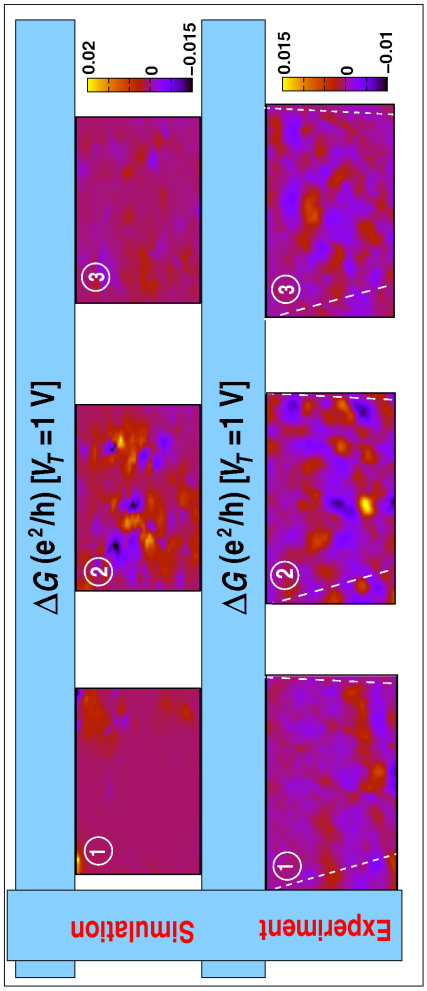

Figure 2.7: Comparison between simulated and measured [49] maps of the variation of the conductance for the values of V_{BG} indicated by circles in Fig. 2.6, and for $V_T = 1$ V.

point of view of the presence, density and intensity of isolated small regions related to huge variations of conductance ("hotspots"), and from the point of view of their behavior as a function of the backgate voltage. We see that the simulation data are able to reproduce with good quantitative agreement the measured density and intensity of hotspots; moreover the increasing intensity and intricacy of the map texture toward the center of the considered Landau

level is also captured by the simulations. The experimental results, thus, can be explained in the framework of our simulation model as follows. The conductance hotspots arise in correspondence of those saddle points of the potential that are crossed by extendend conductive paths or that can couple two localized paths to form an extended one. The effect of the probe can consist in breaking an existing conducting path or promoting the formation of a new path. This, in turn, can induce a significant increase or decrease in the conductance. For saddle points isolated from a conducting path the perturbation induced by the probe results in negligible conductance variations. The intensity and the density of the hotspots decrease for small and high values of V_{BG} as a result of the smaller likelihood for an extended bulk state to arise and of the small amount of current that these states carry in such conditions, due to the strong backscattering at the saddle points.
Finally, in Fig. 2.8, we compare the maps for the variation of conductance for the intermediate value of V_{BG} and two different values of V_T. The experimental data shows that for increasing V_T the hotspots have the tendency to increase in size and to merge togheter into connected areas. This trend is observable also in the simulations, though it is combined with an increase in the hotspot intensity more evident of that in measurements; this discrepancy may be due to the approximation we made about the local density of states (Sec. 2.5) to neglect any change in the square modulus of the wave functions when the bias voltages of the electrodes are varied. Since the carrier density at the saddle points tends to decrease when the potential becomes higher or smaller than the electron energy, the mentioned approximation is likely to result in an overestimation of the probe effect.

2.8 Concluding remarks

The simulation results show that our model, in spite of its simplicity, can describe the main features of the experimental data obtained with SGS techniques. This suggest, in turn, a confirmation in the case of bilayer graphene of the percolation model for the IQHE adopted for the description of the effect in conventional two-dimensional systems. Moreover, the fitting of the simulation

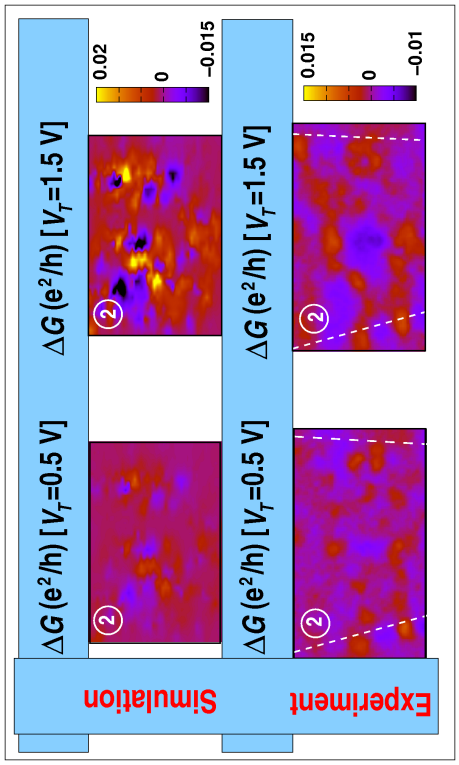

Figure 2.8: Comparison between simulated and measured [49] maps of the variation of the conductance for V_{BG} corresponding approximately to the middle of the percolative riser, and for $V_T = 1$ V and $V_T = 1.5$ V.

results with the measurments provide a way to obtain estimates of physical quantities, related to the undrelying disordered potential, not directly accessible to an SGS experiment.

Chapter 3

Simulative analysis of the suppression of shot noise in diffusive mesoscopic semiconductors

In nanoscale devices shot noise is often suppressed with respect to the value of power spectral density given by the Schottky formula, which would be expected in the absence of correlations between the carriers [59].
As we will review in Sec. 3.1, if the length L of the device is much less than the elastic mean free path l, the transport regime is ballistic and shot noise is strongly suppressed; otherwise, if L is greater than Nl (where N is the number of propagating modes) and the conductor is assumed to be phase coherent, transport is characterized by strong localization, with the resistance increasing exponentially with the length of the device and the shot noise power spectral density approaching the Schottky result; finally, in the intermediate regime in which the values of l (determined by the disorder inside the device), L and N satisfy the unequalities $l \ll L \ll Nl$, transport is diffusive. In this regime the resistance increases linearly with length and shot noise is suppressed by

a factor 1/3. This result has been theoretically obtained for two-dimensional and three-dimensional disorder, using both quantum mechanical [70, 71] and semiclassical [73] approaches; it has been, moreover, obtained in the case of one-dimensional disorder in Ref. [74], in which a series of unevenly spaced tunnel barriers has been considered within a semiclassical model [74].
From the experimental point of view, Henny *et al.* [75] measured the shot noise suppression factor in a thin metallic wire, finding the theoretically predicted 1/3 reduction by asymptotically widening the contact reservoirs and thus reducing the reservoir heating which otherwise would increase the measured noise.
In the case of semiconductor devices, on the other hand, the existing experimental data are not conclusive. Liefrink *et al.* [76] reported, for a wire obtained confining the two-dimensional electron gas in a GaAs/AlGaAs heterostructure, shot noise reduction factors varying between 0.2 and 0.45, depending on the width of the wire. A semiconductor device with one-dimensional disorder (a superlattice with optically generated carriers) has been considered by Song *et al.* [77]; for low applied fields, also in this case the measured suppression factor strongly differs from 1/3, varying from one superlattice to another and, in particular, typically increasing with the width of the barriers.
In this chapter we discuss the possibility of diffusive conduction, and thus of shot noise suppression by a factor 1/3, in mesoscopic semiconductors, in the presence of two-dimensional (2D) and one-dimensional (1D) disorder; to this aim we present the results of several numerical investigations of the noise behavior in quantum wires on GaAs/AlGaAs heterostructures, performed with different models and with varying degree of approximation.
The chapter begins with an introductive section, in which the aspects of the theory most relevant to the following parts are presented. In the next two sections the models and the simulation results are presented for the case of two-dimensional disorder (Sec. 3.2) and one-dimensional disorder (Sec. 3.3). The conclusions we have drawn are briefly summarized in the last section.

3.1 Shot noise in mesoscopic devices

Shot noise in electronic devices consists of random fluctuations of the current, that originate from the granularity of the electric charge. If the correlations between electrons can be neglected, then Schottky's result applies, and the shot noise power spectral density is $S = 2e|\langle I\rangle| = S_P$, with e the modulus of the electron charge and $\langle I\rangle$ the average current [59]. The subscript P remarks that this result corresponds to a Poissonian statistic for the events of transmission of the electrons across the device. In phase coherent mesoscopic devices the quantum statistics of the electrons and the Coulomb repulsion can have important effects on the electron dynamics. Here we account only for the quantum statistics, that is likely to dominate in the examinated cases.
There ia a simple way to deduce the expression for the shot noise power spectral density when the Fermi-Dirac statistics is taken into account [78]. Let us refer to the Landauer theory of transport at zero temperature and consider first a system in which a single mode is transmitted; in these hypotheses the expression of the current is $I = (2e^2/h)VT$, where h is Planck's constant, T is the transmission probability, and eV is the difference between the electrochemical potentials at the contacts. In a time τ, a number $n = (2eV/h)\tau$ of electrons will enter the system, each of which is transmitted with probability T. The Pauli principle guarantees that at zero temperature each state involved in transport is occupied by exactly two electrons, thus keeping n constant over time. The fluctuations in the current may arise only as a consequence of the statistical process of transmission of the incoming electrons. The number n_t of electrons transmitted out of n in the time τ follows a *binomial* distribution:

$$P(n_t) = \binom{n}{n_t} T^{n_t}(1-T)^{n-n_t} \tag{3.1}$$

The variance of n_t is $\langle \delta n_t^2\rangle = nT(1-T)$, and the variance of the current fluctuations results

$$\langle \delta I^2\rangle = \frac{n}{e\tau}T(1-T) = 2\frac{e^3}{h}|V|T(1-T)\,; \tag{3.2}$$

the power spectral density of these fluctuations is, thus,

$$S = 4\frac{e^3}{h}|V|T(1-T)\,. \tag{3.3}$$

If more than one mode enters the system, the overall current is the sum of the contributions of the single modes. Moreover, since the current fluctuations δI associated to the conduction of the single modes are independent random variables, the variance of their sum is just the sum of the variances. Thus, for a multimode propagation, the expression for the power spectral density become, simply,

$$S = 4\frac{e^3}{h}|V|\sum_n T_n(1-T_n)\,. \tag{3.4}$$

Eq. (3.4) predicts a power spectral density of shot noise always suppressed with respect to the Schottky result. In order to quantify the deviations of the power spectral density from S_P it is customary to refer to the *Fano factor* η, defined as

$$\eta = \frac{S}{S_P} = \frac{\sum_n T_n(1-T_n)}{\sum_n T_n} \tag{3.5}$$

In the case of ballistic regime, the T_ns become discrete variables, that can take only the values 0 and 1. As a consequence the shot noise is completely suppressed and $\eta = 0$.
Othewise, Schottky's result is recovered in the condition in which the trasmission probabilities for all the modes are much less than 1:

$$S = 4\frac{e^3}{h}|V|\sum_n T_n(1-T_n) \approx 2e\left(|V|\frac{2e^2}{h}\right)\sum_n T_n = 2e|V|G = 2e|I|\,, \tag{3.6}$$

so that $\eta = 1$. Indeed, in these conditions, the limitation on the maximum number of transmissions in a given time interval imposed by the Pauli principle is ininfluent, and the events of trasmission can be considered as independent; over a time interval τ, large enough to include many transmission attempts, the statistic of n_T tends to become Poissonian with average $\langle n_t\rangle = \langle I\rangle\tau/e$. In order to obtain some insight about the behavior of the conductance in this regime, we can refer for the transmission probabilities to the parametrization [80]

$$T_n = \frac{1}{\cosh^2(\zeta_n L)}\,. \tag{3.7}$$

We see that, for $\zeta_n L \ll 1$, $T_n \approx 1$, while, for $\zeta_n L \gg 1$, $T_n \approx 0$, so that the parameters ζ_n play the role of the inverse of the localization lengths in the

device. The case we are discussing corresponds to $\zeta_n L \gg 1$ for all n, so that the carriers are strongly localized in the sample. Furthermore, since, according to Eq. (3.7), the condition $T_n \ll 1$ implies $T_n \sim \exp(-2\zeta_n L)$, the Landauer expression for the conductance can be approximated as

$$G = \frac{2e^2}{h} \sum_n T_n \approx \frac{2e^2}{h} \sum_n e^{-2\zeta_n L} \sim e^{-2\zeta_{min} L}\,, \tag{3.8}$$

where $\zeta_{min} = \min\{\zeta_n\}$. This suggest that in a phase coherent regime of strong localization the conductance is exponentially suppressed as the lenght of the sample is increased.

We focus now on the Fano factor in devices in which a diffusive regime of transport is established. In phase coherent samples this happens when the condition

$$l \ll L \ll Nl\,, \tag{3.9}$$

where l is the elastic mean free path, L the lenght of the sample and N the number of propagating modes, is verified [79]. Referring to the expression (3.7) for the transmission probabilities, we can easily show that, in this case, the distribution of the ζ_ns has to be uniform. Indeed, in the diffusive regime it is well known that the conductance G is inversely proportional to the sample length L, thus, using the Landauer formula, we can write

$$G/G_0 = N \int_0^\infty d\zeta \rho(\zeta) \frac{1}{\cosh^2(\zeta L)} \propto \frac{1}{L}\,, \tag{3.10}$$

where N is the number of propagating modes and G_0 is the conductance quantum; since

$$\int_0^\infty d\zeta \frac{1}{\cosh^2(\zeta L)} = \frac{1}{L}\,, \tag{3.11}$$

we deduce $\rho(\zeta) = const.$ By comparing Eq. (3.10) with the relation for the transmission [81–83]

$$T = \frac{Nl}{L+l} \approx \frac{Nl}{L}\,, \tag{3.12}$$

where l is the eleastic mean free path, we see that the value of the constant can be approximated to l. The constraint of normalization for $\rho(\zeta)$ implies, in turn, the need to consider an upper bound for the ζs of $\sim 1/l$; this does not affect

the value of the integral in Eq. (3.11), because $L/l \gg 1$ and $1/\cosh^2(L/l)$ has already a very small value. We have, thus, $\rho(\zeta) = Nl\,H(1/l - \zeta)$, where $H(x)$ is the Heaviside function.

Now we are in the position of calculate the distribution of the transmission eigenvalues T_n. We set $f(\zeta) = 1/\cosh^2(\zeta L)$ and we denote with $p(zL)$ the probability density function of the random variable zL. Using the rule for the calculation of the probability density of the functions of a random variable, we have

$$\rho(T) = \frac{p(zL = s)}{|f'(s)|}\,, \tag{3.13}$$

where s is the solution in $[0, l/L]$ of the equation $T = \cosh^{-2}(s)$. Substituting $p(zL) = l/L$ and $s = \mathrm{acosh}(1/\sqrt{(T)})$, we obtain

$$\rho(T) = \frac{l}{2L}\frac{1}{T\sqrt{(1-T)}} \tag{3.14}$$

with $T \in [f(\zeta = 1/l), f(\zeta = 0)] \simeq [4\exp(-2L/l), 1]$. The distribution of the transmission probabilities is therefore *bimodal* with peaks for $T \sim 0$ and $T = 1$. The presence with high probability of modes almost perfectly transmitted entails a suppression of the power spectral density of the shot noise below the Poissonian value, as these modes increase the conductance but do not contribute to the noise. We can confirm this by calculating the Fano factor:

$$\eta = \frac{N\langle T(1-T)\rangle}{N\langle T\rangle} = \frac{\langle T(1-T)\rangle}{\langle T\rangle}\,; \tag{3.15}$$

we find

$$\langle T(1-T)\rangle = \int_{4e^{-\frac{2L}{l}}}^{1} dT\,T\,(1-T)p(T) \simeq \int_{0}^{1} dT\,T\,(1-T)p(T) = \frac{l}{3L}\,, \tag{3.16}$$

$$\langle T\rangle = \int_{4e^{-\frac{2L}{l}}}^{1} dT\,Tp(T) \simeq \int_{0}^{1} dT\,Tp(T) = \frac{l}{L}\,, \tag{3.17}$$

and, thus,

$$\eta = \frac{1}{3}\,. \tag{3.18}$$

This result is *universal*, in the sense that, as long as the geometry is quasi one-dimensional, the condition (3.9) is verified and inelastic process can be neglected, the Fano factor is not affected by the variation of other characteristics

of the system, such as the number of propagating modes or the properties of the disorder.
In order to account for the presence of a magnetic field, in the following we will consider for Eq. (3.9) a more general form [84–86]:

$$l \ll L \ll (\beta N + 2 - \beta) l = L_l \,, \tag{3.19}$$

where we indicated with L_l the average localization length (referred in the following simply as localization length). The symmetry index β takes on the values 2 or 1 depending on whether or not a magnetic field is present, respectively; the value 4 corresponds to strong spin-orbit scattering or scattering from magnetic impurities and is not of interest here.

3.2 Two-dimensional disorder

The structure we consider is a quantum wire obtained laterally confining, by means of negatively biased gates located on the surface, the two-dimensional electron gas (2DEG) of a GaAs/AlGaAs heterostructure. The ionized donors located inside the n-doped AlGaAs layer (together with other charged impurities present inside the heterostructure) determine potential fluctuations at the 2DEG level.
In a previous paper by our group [88] a self-consistent calculation of the average potential, combined with a semi-analytical formula for the effect of ionized donors, was used to fit the conductance measurement on a fabricated quantum wire and to numerically predict its noise behavior. In that case it was found that the Fano factor did not stabilize at 1/3, but it rather crossed it for a single value of the gate bias voltage.
In order to gain a better understanding of the problem, we have now studied the noise behavior of the structure for a larger range of parameters, for some choices of a model potential. In detail, we have considered a 4.9 μm long and 8.4 μm wide conductor with a hard-wall lateral confinement (since in our previous investigations the detailed shape of the confinement potential did not appear to play a significant role on the noise behavior). We have considered that all of the dopants are located at a distance $D = 40$ nm from the 2DEG and, for

each considered dopant concentration (with a uniform random distribution), we have initially evaluated the effect, at the level of the 2DEG, by summing up each individual contribution. The contribution of a single dopant has been evaluated with the semi-analytical expression given by Stern and Howard [89], according to which a point charge Ze located at a distance D from the 2DEG generates on the 2DEG, at a distance r from its orthogonal projection onto the 2DEG plane, a screened potential equal to

$$\phi(r) = \frac{Ze}{4\pi\epsilon_0\epsilon_r} \int_0^\infty \frac{k}{k+s} J_0(kr) e^{-kD} dk \tag{3.20}$$

where J_0 is the Bessel function of order 0 and s the screening length

$$s = 2n_\nu (m^* e^2)/(4\pi\epsilon_0\epsilon_r \hbar^2)$$

(with $n_\nu = 1$ the considered subband degeneracy). In order to have a neutral system with a potential landscape symmetric around zero, which simplifies the investigation and comparison of a large number of different cases, we have considered an artificial situation with an equal number of positive and negative charges. Then, different disorder strengths for each dopant concentration have been obtained simply by multiplying the thus obtained potential profile by a scale factor K. As an example, in Fig. 3.1 we show a map of the potential obtained at the 2DEG level for a concentration $N_D = 1.1 \times 10^{14}$ m^{-2} of impurities located at a distance $D = 40$ nm from the 2DEG, multiplied by a disorder strength scale factor $K = 39$. Once the potential at the 2DEG level has been obtained, the transmission matrix of the device has been evaluated using the recursive Green's function technique, with a rapresentation over the transverse modes in the confined direction and in real space in the transport direction [90,91]. From the transmission matrix t, the conductance G, the shot noise power spectral density S_I and the Fano factor η have been obtained using the Landauer formula

$$G = \frac{2\,e^2}{h} \sum_n T_n \,, \tag{3.21}$$

and Eq. (3.4) and Eq. (3.5), respectively, where the transmission coefficients T_n are obtained as eigenvalues of the matrix $t^\dagger t$. In these calculations we have separately averaged the conductance and noise results (and thus the numerator

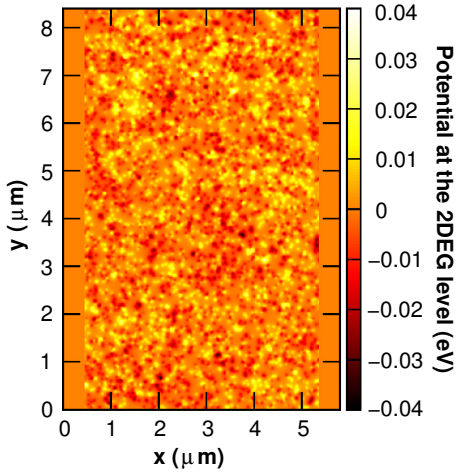

Figure 3.1: Map of the potential obtained at the 2DEG level for a concentration $N_D = 1.1 \times 10^{14}$ m^{-2} of impurities located at a distance $D = 40$ nm from the 2DEG, multiplied by a scale factor $K = 39$.

and denominator of Eq. (3.5)) over 41 energy values uniformly spaced in an energy range of 80 μeV around $E_F = 9$ meV.

In Fig. 3.2 we report the Fano factor that we have obtained for 7 values of the dopant concentration N_D, as a function of the disorder strength scale factor K. We see that for elevated concentrations the interval of disorder strength within which the curves approach the value 1/3 is very narrow, while it gets wider for low concentrations. However, in this latter case the diffusive behavior is obtained only for very large scale factors K. If we focus our attention on the potential deriving, at the 2DEG level, from each single charged impurity and in particular on the portion that more affects transport, i.e. that above the Fermi energy, we see that for these values of K its spatial extent is of the order of hundreds of nanometers. Since this extension is unrealistic for semiconductor devices (while it could be reasonable for metallic conductors, characterized by the presence of large grains), we conclude that in semiconduc-

tor nano devices it is quite unlikely to obtain a 1/3 shot noise suppression factor within a reasonably large parameter range. Finally, for the lowest concentration ($N_D = 1.1 \times 10^{12}$ m^{-2}) the Fano factor remains well below the 1/3 value and thus we have a substantially ballistic regime for all the considered disorder strengths. In Fig. 3.3 we show the normalized conductance G/G_0 (where G_0

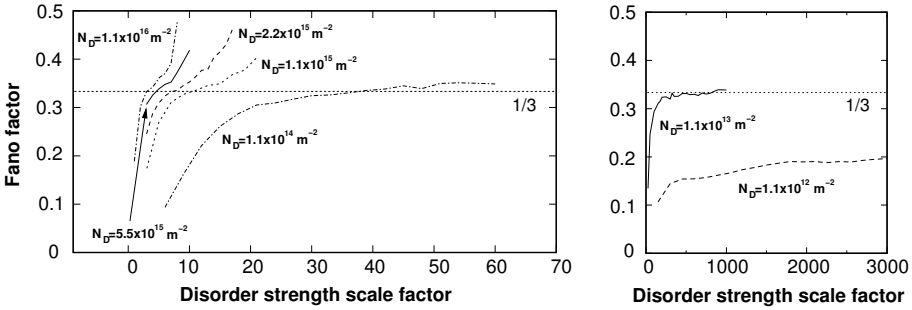

Figure 3.2: Fano factor as a function of the disorder scale factor K for 7 values of the dopant concentration N_D and for $E_F = 9$ meV.

is the conductance quantum $2e^2/h$) as a function of the disorder strength scale factor K for the same impurity concentrations N_D.
Since from Eq. we have that $G/G_0 \approx Nl/(L+l)$, in this case, being $N = 336$, the condition for diffusive transport $l \ll L \ll L_l$ (with $L_l \approx Nl$) is satisfied by a factor of 10 for both unequalities if $9.7 < G/G_0 < 30.5$. We again observe that the interval in which the condition for diffusive transport is satisfied is very narrow for elevated concentrations, while it widens for low concentrations, for which, however, large disorder strengths are needed. Finally, in the case of $N_D = 1.1 \times 10^{12}$ m^{-2}, the conductance never satisfies such a condition.

The comparison between Fig. 3.2 and Fig. 3.3 confirms that the Fano factor assumes values near 1/3 in the same parameter range in which the condition $l \ll L \ll L_l$ is satisfied. This range can clearly be enlarged increasing the number N of propagating modes, but this can be obtained only considering wider conductors, with macroscopic dimensions. In such conditions, however, shot noise is in general not observable, since the longitudinal extension of the

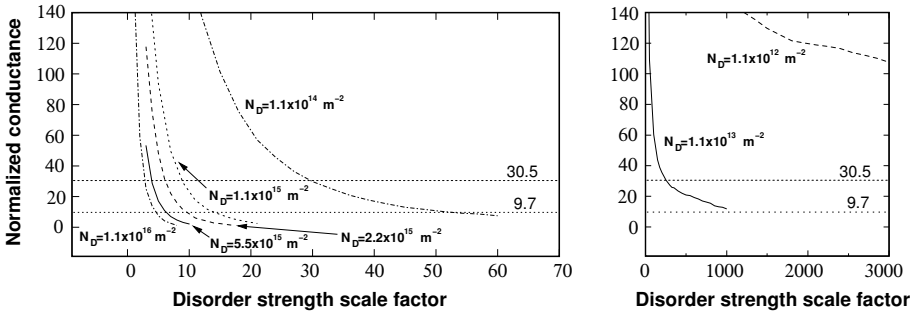

Figure 3.3: Conductance (normalized with respect to the conductance quantum G_0) as a function of the disorder scale factor K for 7 values of the dopant concentration N_D and for $E_F = 9$ meV.

sample exceeds the Debye length [21].
Instead, in the case of metallic conductors, due to the higher number of propagating modes and to the possibility of extended scatterers, diffusive transport can actually be reached and experimentally measured, although with a peculiar choice of size and geometries.
Finally, we have performed some simulations using a more simplified model for the disordered potential [93]. In Ref. [93] a discussion on the exact conditions needed to obtain the diffusive transport regime was presented, and the disordered potential in the the considered 2D wires is modeled with a random distribution of square obstacles. In particular, we have repeated the calculation corresponding to the upper curve of Fig. 6 of Ref. [93], obtaining the results reported in the upper panel of Fig. 3.4. The simulation has been performed considering a wire with a width $W = 5$ μm and a length $L = 8$ μm, containing 300 hard-wall square obstacles, with a 100 nm edge. In the figure we show the Fano factor as a function of the Fermi energy of the impinging elecrons. We see that, as soon as the Fermi energy has reached the value corresponding to a number of propagating modes for which the condition $l \ll L \ll Nl$ is satisfied, the Fano factor reaches the value 1/3. In order to verify whether the diffusive regime is preserved over a large range of scatterer concentrations,

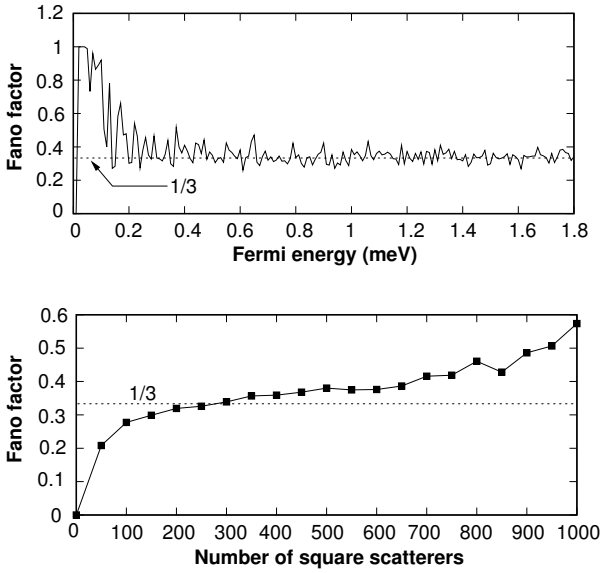

Figure 3.4: Upper panel: Fano factor as a function of the Fermi energy of the impinging electrons, obtained in a 5 μm wide and 8 μm long wire, containing 300 hard-wall 100 nm×100 nm obstacles.
Lower panel: Fano factor as a function of the number of hard-wall square scatterers in the wire.

we have made some simulations varying the number of square scatterers inside the wire and computing the Fano factor around a value of the Fermi energy, $E_F = 1.25$ meV, for which the diffusive regime has been reached in the case of 300 scatterers. In particular, we have separately averaged the conductance and noise results over a set of 41 uniformly spaced energy values in a range of 80 μeV around 1.25 meV. In the lower panel of Fig. 3.4 we show the behavior of the Fano factor as a function of the number of square scatterers inside the conductor. We see that also in this case the Fano factor does not settle around 1/3 for a large range of scatterer numbers, but just crosses the 1/3 value in correspondence of about 300 scatterers, which is indeed the situation for which

the conditions for diffusive regime have been investigated in Ref. [93]. Thus, this was a particular case, not representative of the general behavior.

3.3 One-dimensional disorder

The case of strictly one-dimensional disorder [94, 95], i.e. of unevenly spaced tunnel barriers located in an otherwise purely ballistic device with any dimensionality, is a bit different from the cases of 2D or 3D disorder, even though, according to semiclassical studies of this structure [74, 96], also in this case the shot noise suppression factor should approach 1/3 as the number of cascaded barriers is let go to infinity.

A series of barriers can be defined, for example, in a heterostructure-based device defining a series of gates on the surface of the device. Such gates, when negatively biased, locally deplete the 2DEG, each generating a tunnel barrier for the electrons traveling in the device.

We consider, for simplicity, idealized rectangular barriers, since we have verified that the main results are not modified by the inclusion of realistic features [97]. Since a wire with a series of such rectangular transversal barriers (each extending across the whole cross-section) can be seen as made up of a series of sections differing only for the value of their constant potential, the wave functions associated with the transverse modes are the same in all of the sections and the tunnel barriers do not introduce any mode-mixing. Therefore the transport computation can be subdivided into many purely 1D problems. We have performed the simulation using a scattering matrix approach, evaluating for each mode individually the transmission coefficient. In Fig. 3.5 we report, for a series of identical barriers, the Fano factor as a function of the number of the unevenly spaced barriers for 3 values of the barrier transparency Γ. In detail, we have considered an 8 μm wide structure and we have averaged our conduction and noise results over 500 energy values uniformly distributed in a range of 40 μeV around 9.03 meV. We have considered 0.425 nm thick barriers, with heights equal to 0.8, 0.25 and 0.07 eV. We define the transparency Γ as the squared modulus of the transmission coefficient through each barrier, averaged over all the propagating modes. For the 3 values of barrier height the trans-

parency Γ is about equal to 0.1, 0.5 and 0.9, respectively. In order to obtain a general behavior, we have averaged the results over 50 different sets of interbarrier distances, which is equivalent to introducing dephasing with a simple phase randomization model preserving localization effects [34]. These averages show that, contrary to what was expected from a semiclassical analysis [74], no common asymptotic 1/3 value for the Fano factor is reached increasing the number of barriers.

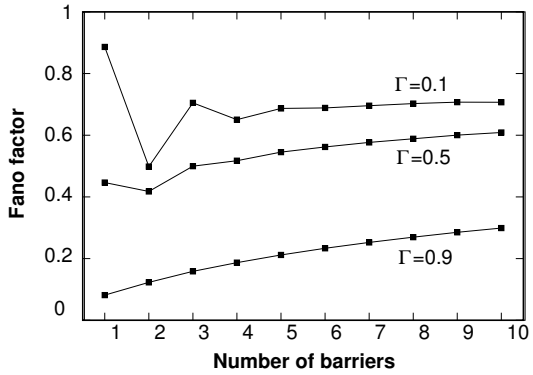

Figure 3.5: Fano factor as a function of the number of barriers for 3 values of the barrier transparency Γ, averaged over 50 different sets of interbarrier distances.

The reason is that in the absence of mode-mixing the overall transport problem is just a collection of intrinsically one-dimensional problems; therefore the localization length L_l is equal to l and thus it is impossible to satisfy the condition for diffusive transport $l \ll L \ll L_l$. Since semiclassical descriptions do not take into account the effect of phase coherence on transport and thus do not include localization, this effect can not be predicted using semiclassical arguments, but results only from a quantum-mechanical analysis.

In Ref. [97] it has been shown that the presence of a realistic amount of edge-roughness in the depletion gates defining the barriers, introducing only a small degree of mode-mixing, does not alter significantly the described results.

On the other hand, the amount of 2D disorder that we should add to the device in order to create mode-mixing and reach the diffusive regime would be such that it would lead to diffusive transport even in the absence of the barriers, and therefore of the 1D disorder. Therefore, in order to reach the diffusive regime while preserving the 1D nature of the disorder, we have to introduce a different source of mode-mixing, for example a magnetic field threading the device.
From Eq. (3.19) with $\beta = 2$ we deduce that a magnetic field cannot modify the localization length for single-mode propagation ($N = 1$). However, in the case of a series of tunnel barriers and, in particular, in the case of quite transparent barriers, the presence of a magnetic field makes it possible to to reach a 1/3 value for the Fano factor [94]. The explanation of this apparent contradiction is that the magnetic field, introducing mode-mixing, changes the effective dimensionality of the system from 1D to 2D; therefore $N > 1$ has to be considered in Eq. (3.19), and the localization length increases from l to $\beta N l$.
Here we show the results obtained for a 1 μm wide conductor containing a series of 66 meV high and 1.56 nm thick barriers, with an average transparency at the considered Fermi energy (9.03 meV) $\Gamma = 0.5$. The transport calculation has been carried out using the recursive Green's function technique, and adopting, for the representation of the vector potential, a Landau gauge with nonzero component only along the transverse direction [107]. The conductance and noise results have been averaged over a set of 25 energy values uniformly distributed over a range of 40 μeV around 9.03 meV. The final results have been averaged over 20 different sets of interbarrier distances. We see in Fig. 3.6 that, while in the absence of magnetic field we observe an exponential behavior of the resistance as a function of the number of the barriers (characteristic of the strong localization regime), applying an orthogonal magnetic field $B = 0.1$ T the resistance behavior becomes approximately linear, i.e. we approach the diffusive regime. In detail, we have found that in our structure L_l increases by about a factor 7 when the magnetic field is applied.

However, in order to obtain a diffusive regime over a really wide range of parameters, the mode-mixing introduced by the magnetic field has to be combined with the presence of a large number of propagating modes, which requires, also in this case, macroscopic dimensions, for which shot noise is

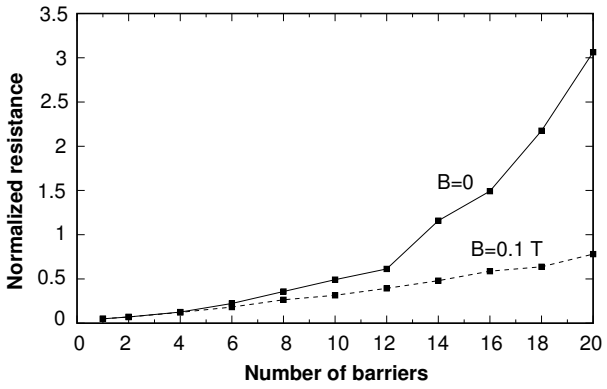

Figure 3.6: Resistance (normalized with respect to the conductance quantum $h/(2e^2)$) as a function of the number of cascaded tunnel barriers in a 1 μm wide conductor with 66 meV high and 1.56 nm thick barriers, with $E_F = 9.03$ meV; the exponential behavior has been obtained without the magnetic field, while the nearly linear one has been found applying an orthogonal magnetic field $B = 0.1$ T.

generally not observable.

3.4 Concluding Remarks

From our numerical simulations, in which different representations for the potential disorder have been adopted, we conclude that it should be rather uncommon to obtain fully diffusive transport in mesoscopic semiconductor devices, due to the insufficient number of propagating modes. Indeed, the simulation results have shown that the diffusive regime tends to be restricted to small regions in the explored parameters space.

In the case of 1D disorder the absence of mode-mixing makes it theoretically impossible to reach the diffusive regime, unless a source of mode-mixing, such as a magnetic field, is introduced.

Our conclusions seem to be supported by existing experimental results, which

in the case of mesoscopic semiconductor devices have not shown a clear 1/3 suppression of shot noise.

Chapter 3. Simulative analysis of the suppression of shot noise in diffusive mesoscopic semiconductors

Conclusions

In this thesis we have treated, from the perspective of the numerical simulation, the transport in two-dimensional and quasi one-dimensional carrier systems, which are nowadays considered promising for the development of post-silicon electronics. We investigated different aspects of the conduction process, taking into account the presence of static electric and magnetic fields. We resorted to different numerical approaches but our simulations were always based on continuum approximations, since we have dealt with systems with a size too large to be modeled with atomistic detail.

We have addressed the issue of the simulation of non dissipative transport in large area monolayer graphene domains in the presence of an electrostatic potential varying both in the direction of the current flow and in the transversal one. We have studied the problem of the numerical solution of the one-dimensional Dirac equation, establishing, for this purpose, several numerical algorithms, both in the direct and in the reciprocal space. The more effective of these has been integrated into a recursive scattering matrix code, able to perform the computation of the conductance for domains of almost arbitrary shape. Within the same framework we have investigated more in depth and from a more analytical point of view some unusual properties of the transport in armchair graphene nanoribbons, finding a link with the field of non Hermitian Hamiltonians.

We have also considered the transport in bilayer graphene, focusing on the condition in which the sample is orthogonally threaded by a strong magnetic field and the Integer Quantum Hall effect appears. We have resorted to an effective percolative model, based on a semiclassical picture of the carrier motion. In

order to make a close comparison with the experimental data possible, we have focused our attention on scanning gate spectroscopy experiments and we have augmented the model by introducing the suitable links with the relevant experimental quantities. By exploring the space of the free parameters of the model we have found the best agreement with the measurement for values quite close to the estimates proposed in the literature. Our data support an interpretation of the experimental results in terms of the adopted percolative view, and thus, an explanation on the same basis of the Integer Quantum Hall effect in bilayer graphene.

Finally, we have studied the occurrence in realistic cases of the theoretically predicted suppression by 1/3 of the power spectral density of shot noise in diffusive mesoscopic devices. We have considered quantum wires defined in GaAs/AlGaAs heterostructures, simulating the transport within the effective mass approximation by means of recursive scattering matrix and recursive Green's function approaches. We have considered the case of both one-dimensional and two-dimensional disorder, tuning the disorder parameters over wide ranges, including the typical dispersion intervals. Our results allow to explain the discrepancy between theoretical predictions and experimental data in terms of an unlikelihood for mesoscopic systems to enter a fully diffusive regime (two-dimensional disorder case) and the impossibility for a system to enter this regime due to the lack of mode mixing (one-dimensional disorder case).

Bibliography

[1] V. Umansky *et al.*, Journal of Crystal Growth **311**,number = "7", 1658 (2009).

[2] K. S. Novoselov *et al.*, Science **306**, 666 (2004).

[3] Y. Zhang *et al.*, Nature **459**, 820 (2009).

[4] J. H. Chen *et al.*, Nature Nanotech. **3**, 206 (2006).

[5] A. Geim, Graphene update. Bull. Am. Phys. Soc. **55**, abstr. J21.0004, http://meetings.aps.org/link/BAPS.2010.MAR.J21.4 (2010).

[6] J. Wurm, M. Wimmer, I. Adagideli, K. Richter, H. U. Baranger, New Journal of Physics **11**, 095022 (2009).

[7] H. Li, L. Wang, Z. Lan, Y. Zheng, Phys. Rev. B **79**, 155429 (2009).

[8] Benliang Zhou, Benhu Zhou, Wenhu Liao, Guanghui Zhou, Phys. Lett. A **374**, 761 (2010).

[9] A. H. Castro Neto, F. Guinea, N. M. R. Peres, K. S. Novoselov, A. K. Geim, Rev. Mod. Phys. **81**, 109 (2009).

[10] L. Brey, H. A. Fertig, Phys. Rev. B **73**, 235411 (2006).

[11] P. Marconcini, M. Macucci, La Rivista del Nuovo Cimento **34**, 489 (2011).

[12] J. Tworzydło, C. W. Groth, C. W. J. Beenakker, Phys. Rev. B **78**, 235438 (2008).

BIBLIOGRAPHY

[13] A. R. Hernández, C. H. Lewenkopf, Phys. Rev. B **86**, 155439 (2012).

[14] R. Stacey, Phys. Rev. D **26**, 468 (1982).

[15] C. M. Bender, K. A. Milton, D. H. Sharp, Phys. Rev. Lett. **51**, 1815 (1983).

[16] L. Susskind, *Lattice fermions*, Phys. Rev. D **16**, 3031 (1977).

[17] I. Montvay, G. Münster, "Quantum fields on a lattice", Cambridge University Press, Cambridge (1994).

[18] A. Smilga, "Lectures on quantum chromodynamics", World Scientific, Singapore (2001).

[19] M. Fagotti, C. Bonati, D. Logoteta, P. Marconcini, M. Macucci, Phys. Rev. B **83**, 241406(R) (2011).

[20] J. Foerster, A. Saenz, U. Wolff, Phys. Rev. E **86**, 016701 (2012).

[21] S. Datta, *Electronic Transport in Mesoscopic Systems*, Cambridge University Press, Cambridge (1995).

[22] C. M. Bender, D. C. Brody, H. F. Jones, Phys. Rev. Lett. **89**, 270401 (2002).

[23] Code is available at "NanoTCAD ViDES," DOI: 10254/nanohub-r5116.5; http://nanohub.org/resources/ vides/

[24] C. E. Shannon, Proc. Institute of Radio Engineers, **37**, 10 (1949).

[25] K. von Klitzing, G. Dorda, M. Pepper, Phys. Rev. Lett. **45**, 494 (1980).

[26] K. S. Novoselov *et al.*, Science, **315**, 1379 (2007).

[27] K. S. Novoselov *et al.*, Nature Phys. **2**, 177 (2006).

[28] E. McCann, M. Koshino, arXiv:1205.6953 [cond-mat.mes-hall].

[29] D. A. Abanin, L. S. Levitov, Phys. Rev. B **78**, 035416 (2008).

[30] J. R. Williams, D. A. Abanin, L. DiCarlo, L. .S Levitov, C. M. Marcus, Phys. Rev. B **80**, 045408 (2009).

[31] D. H. Cobden, C. H. W. Barnes, C. J. B. Ford, Phys. Rev. Lett. **82**, 4695 (1999).

[32] S. Ilani *et al.* Nature **427**, 328 (2004).

[33] J. Martin *et al.*, Nat. Phys. **5**, 669 (2009)

[34] S. R. E. Yang, A. H. MacDonald, B. Huckestein, Phys. Rev. Lett. 74, 3229 (1995).

[35] A. Struck, B. Kramer, Phys. Rev. Lett. **97**, 106801 (2006).

[36] R. A. Römer, C. Sohrmann, Phys. Status Solidi B **245**, 336 (2008).

[37] C. Sohrmann, J. Oswald, R. A. Römer, *Quantum Percolation in the Quantum Hall Regime*; Lecture Notes in Physics; Springer: Berlin Heidelberg, 2009; Vol. 762.

[38] C. Zhou, M. Berciu, R. N. Bhatt1, Phys. Rev. B **71**, 125310 (2005).

[39] R. R. Gerhardts 1975 Z. Phys. B **21** 275 (1975); R. R. Gerhardts, Z. Phys. B **21** 285 (1975).

[40] T. Ando, Y. Uemura, J. Phys. Soc. Jpn. **37**, 1044 (1974).

[41] A. Potts *et al*, J. Phys.: Condens. Matter **8** 5189 (1996)

[42] J. T. Chalker and P. D. Coddington, J. Phys. C **21**, 2665 (1988).

[43] B. Kramer, T. Ohtsuki, and S. Kettemann, Physics Reports **417**, 211 (2005).

[44] H. A. Fertig and B. I. Halperin, Phys. Rev. B **36**, 7969 (1987).

[45] Y. Dubi, Y. Meir, and Y. Avishai, Phys. Rev. B **74**, 205314 (2006).

[46] M. R. Connolly *et al.*, arXiv:1111.0560.

[47] G. M. Rutter *et al.*, Nat. Phys. **7**, 649 (2011).

BIBLIOGRAPHY

[48] A. Deshpande, W. Bao, Z. Zhao, C. N. Lau, B. J. LeRoy, Appl. Phys. Lett. **95**, 243502 (2009).

[49] M. R. Connolly *et al.*, Nano Lett. **12**, 5448 (2012).

[50] T. Kato *Perturbation Theory for Linear Operators* (Springer, Berlin, 1995).

[51] M. V. Berry, Czech. J. Phys **54**, 1039 (2004); W. D. Heiss, Czech. J. Phys **54**, 1091 (2004).

[52] C. Dembowski *et al.*, Phys. Rev. Lett. **86**, 787 (2001); C. Dembowski *et al.*, Phys. Rev. Lett. **90**, 034101 (2003). S.-B. Lee *et al.*, Phys. Rev. Lett. **103**, 134101 (2009).

[53] H. Cartarius *et al.*, Phys. Rev. Lett. **99**, 173003 (2007).

[54] S. Klaiman *et al.*, Phys. Rev. Lett. **101**, 080402 (2008). A. Mostafazadeh, Phys. Rev. Lett. **102**, 220402 (2009).

[55] R. El-Ganainy *et al.*, Opt. Lett. **32**, 2632 (2007); Z. H. Musslimani *et al.*, Phys. Rev. Lett. **100**, 030402 (2008); K. G. Makris *et al.*, Phys. Rev. Lett. **100**, 103904 (2008).

[56] A. Guo *et al.*, Phys. Rev. Lett. **103**, 093902 (2009); C. E. Rüter *et al.*, Nature Phys. **6**, 192 (2010).

[57] H. Schomerus, Phys. Rev. Lett. **104**, 233601 (2010). Y. D. Chong *et al.*, Phys. Rev. Lett. **105**, 053901 (2010).

[58] V. Gerasik and M. Stastna, Phys. Rev. E **81**, 056602 (2010).

[59] W. Schottky, *Ann. Phys. (Leipzig)* **57**, 541 (1918).

[60] Ya. M. Blanter, M. Büttiker, *Phys. Rep.* **336**, 1 (2000).

[61] S. Datta, *Electronic transport in mesoscopic systems* (Cambridge University Press, Cambridge, 1995).

[62] C. W. Beenakker, *Rev. Mod. Phys.* **69**, 731 (1997).

[63] J.-L. Pichard, in *Quantum Coherence in Mesoscopic Systems*, ed. B. Kramer, NATO ASI Series B254 (Plenum, New York, 1991), p. 369.

[64] S. Kettemann, R. Mazzarello, *Phys. Rev. B* **65**, 085318 (2002).

[65] A. Kolek, A. W. Stadler, G. Hałdaś, *Phys. Rev. B* **64**, 075202 (2001).

[66] R. A. Jalabert, J.-L. Pichard, C. W. J. Beenakker, *Europhys. Lett.* **27**, 255 (1994).

[67] P. A. Mello, J.-L. Pichard, *Phys. Rev. B* **40**, 5276 (1989).

[68] M. J. M. de Jong, C. W. J. Beenakker, in *Coulomb and Interference Effects in Small Electronic Structures*, ed. D. C. Glattli and M. Sanquer (Editions Frontieres, France, 1995), p. 427.

[69] Yu. V. Nazarov, *Phys. Rev. Lett.* **73**, 134 (1994).

[70] C. W. J. Beenakker, M. Büttiker, *Phys. Rev. B* **46**, 1889 (1992).

[71] B. L. Altshuler, L. S. Levitov, A. Yu. Yakovets, *JETP Lett.* **59**, 857 (1994).

[72] Ya. M. Blanter and M. Büttiker, *Phys. Rev. B* **56**, 2127 (1997).

[73] K. E. Nagaev, *Phys. Lett. A* **169**, 103 (1992).

[74] M. J. M. de Jong, C. W. J. Beenakker, *Phys. Rev. B* **51**, 16867 (1995).

[75] M. Henny, S. Oberholzer, C. Strunk, C. Schönenberger, *Phys. Rev. B* **59**, 2871 (1999).

[76] F. Liefrink, J. I. Dijkhuis, M. J. M. de Jong, L. W. Molenkamp, and H. van Houten, *Phys. Rev. B* **49**, 14066 (1994).

[77] W. Song, A. K. M. Newaz, J. K. Son, E. E. Mendez, *Phys. Rev. Lett.* **96**, 126803 (2006).

[78] C. Beenakker and C. Schönenberger, Physics Today **56**, 37 (2003).

[79] C. W. J. Beenakker and M. Büttiker, Phys. Rev. B **46**, 1889 (1992).

BIBLIOGRAPHY

[80] M. J. M. de Jong and C. W. J. Beenakker, in *Coulomb and Interference Effects in Small Electronic Structures*, Atlantica Sguier Frontires, France, 1994, p. 427.

[81] P. W. Anderson, D. J. Thouless, E. Abrahams, D. S. Fisher, Phys. Rev. B **22**, 3519 (1980).

[82] P. W. Anderson, Phys. Rev. B **23**, 4828 (1981).

[83] E. Abrahams, P. W. Anderson, D. C. Licciardello, T. V. Ramakrishnan, Phys. Rev. Lett. **42**, 673 (1979).

[84] C. W. Beenakker, Rev. Mod. Phys. **69**, 731 (1997).

[85] J. L. Pichard, in Quantum Coherence in Mesoscopic Systems, ed. B. Kramer, NATO ASI Series B254 (Plenum, New York, 1991), p. 369.

[86] S. Kettemann and R. Mazzarello, Phys. Rev. B **65**, 085318 (2002).

[87] G. Gomila, T. Gonzalez, L. Reggiani, *Phys. Rev. B* **66**, 245423 (2002)

[88] L. Bonci, G. Fiori, M. Macucci, G. Iannaccone, S. Roddaro, P. Pingue, V. Piazza, M. Cecchini, F. Beltram, *Physica E* **19**, 107 (2003).

[89] F. Stern, W. E. Howard, *Phys. Rev.* **163**, 816 (1967).

[90] F. Sols, M. Macucci, U. Ravaioli, K. Hess, *J. Appl. Phys.* **66**, 3892 (1989).

[91] M. Macucci, A. Galick, U. Ravaioli, *Phys. Rev. B* **52**, 5210 (1995).

[92] M. Büttiker, *Phys. Rev. Lett.* **65**, 2901 (1990).

[93] M. Macucci, G. Iannaccone, G. Basso, B. Pellegrini, *Phys. Rev. B* **67**, 115339 (2003).

[94] P. Marconcini, M. Macucci, G. Iannaccone, B. Pellegrini, *Phys. Rev. B* **79**, 241307(R) (2009).

[95] P. Marconcini, M. Macucci, G. Iannaccone, B. Pellegrini, in *Proceedings of the 20th International Conference on Noise and Fluctuations (ICNF-2009)*, Pisa, Italy, 2009, *AIP Conference Proceedings* **1129**, p. 423 (2009).

[96] R. Liu, P. Eastman, Y. Yamamoto, *Solid State Commun.* **102**, 785 (1997).

[97] M. Totaro, P. Marconcini, D. Logoteta, M. Macucci, in *Proceedings of of the 9th IEEE Conference on Nanotechnology (IEEE Nano 2009)*, Genoa, Italy, 2009, *IEEE Conference Proceedings*, IEEE Catalog Number: CFP09NAN-CDR, p. 611 (2009).

[98] M. G. Pala, G. Iannaccone, *Phys. Rev. B* **69**, 235304 (2004).

[99] P. A. Lee, D. S. Fisher, *Phys. Rev. Lett.* **47**, 882 (1981).

[100] K. B. Efetov and A. I. Larkin, *Sov. Phys. JETP* **58**, 444 (1983).

[101] O. N. Dorokhov, *Sov. Phys. JETP* **58**, 606 (1983).

[102] J.-L. Pichard, M. Sanquer, K. Slevin, P. Debray, *Phys. Rev. Lett.* **65**, 1812 (1990).

[103] H. Tamura, T. Ando, *Phys. Rev. B* **44**, 1792 (1991).

[104] R. Blümel, U. Smilansky, *Phys. Rev. Lett.* **69**, 217 (1992).

[105] H. Schomerus, C. W. J. Beenakker, *Phys. Rev. Lett.* **84**, 3927 (2000).

[106] M. Weiss, T. Kottos, T. Geisel, *Phys. Rev. B* **63**, 081306(R) (2001).

[107] P. Marconcini, M. Macucci, *Journal of Computational Electronics* **2**, p. 387 (2003).

BIBLIOGRAPHY

Appendix A

Other approaches to the solution of the one-dimensional Dirac equation in AGRN

In this appendix we propose two alternative reformulation in the spatial domain for the problem of solving the Dirac equation in a transversal section of an AGNR, in the presence of a longitudinally constant electrostatic potential. In Sec. A.1 we rewrite Eq.(1.42) as a second order scalar differential equation, while in Sec. A.2 we consider a reformulation in a cardinal sines basis.

Other approaches to the solution of the one-dimensional Dirac equation in AGRN

A.1 Reformulation as a second order scalar differential equation

Let us consider Eq. (1.42) and an unknown scalar function $\xi(y)$. It is simple to see by direct computation that if ξ satisfies the following system

$$\begin{cases} \left(-\dfrac{d^2}{d\,y^2} + 2i\,h(y)\dfrac{d}{d\,y}\right)\xi(y) = -\kappa_x^2\xi(y) \\ \xi(2\tilde{W}) = e^{2iK_0\tilde{W}}\xi(0) \\ \xi'(2\tilde{W}) = e^{2iK_0\tilde{W}}\xi'(0) \end{cases}, \tag{A.1}$$

where $\xi'(y)$ is a shorthand for $d\xi/dy$ and K_0 is defined as

$$K_0 = K + \frac{1}{\tilde{W}}\int_0^{\tilde{W}} h(\alpha)d\alpha\,, \tag{A.2}$$

then

$$\vec{\varphi}(y) = e^{-i\int_0^y h(\alpha)d\alpha}\left[\kappa_x\xi(y)\begin{pmatrix}1\\ i\end{pmatrix} - \xi'(y)\begin{pmatrix}1\\ -i\end{pmatrix}\right] \tag{A.3}$$

satisfies the original system (1.42). Again the boundary condition can be seen as a periodic boundary condition for the function $e^{-iK_0y}\xi(y)$ and its derivative.

A.2 Reformulation in a cardinal sines basis

Let us define

$$\mathrm{sinc}(y) = \frac{\sin(\pi y)}{\pi y}\,. \tag{A.4}$$

The sampling theorem [24], reformulated in the spatial domain, states that a function $f(y)$ with Fourier spectrum limited to $\nu_{max} = 1/\lambda_{min}$ can be expanded as

$$f(y) = \sum_{m=-\infty}^{+\infty} f(mw)\ \mathrm{sinc}(\frac{y-mw}{w})\,, \tag{A.5}$$

provided that the sampling period w verifies the condition $w < 1/(2\nu_{max})$. If $f(y)$ is periodic with period Nw, the previous equation can be rearranged in

order to involve only the samples of the function within a single period:

$$f(y) = \sum_{l=1}^{N} f(lw) \sum_{m=-\infty}^{+\infty} \mathrm{sinc}(\frac{y-(l+mN)w}{w}) \,. \tag{A.6}$$

We can exploit this property to obtain a reformulation of the problem in the orthonormal basis of the functions $1/\sqrt{w}\ \mathrm{sinc}(\frac{y-mw}{w})$.
Let us consider Eqs. (1.42), and, in particular, the extension by periodicity outside $[0, 2\tilde{W}]$ of the function $e^{-i\tilde{K}y}\varphi(y)$ and of the function $h(y)$. We restrict to the case in which the same number N of samples are considered for the function $e^{-i\tilde{K}y}\varphi(y)$ and for for the function $h(y)$. Since these functions may not have a limited spectrum, in general Eq. (A.5) applies to them only as an approximation. The integer N should be chosen large enough in order for the condition $w < 1/(2\nu_{max})$ to hold for the highest harmonic in the spectrum of both functions that is estimated to be relevant to achive the desired precision of the computation.
Following Eq. (A.6) we can write

$$e^{-i\tilde{K}y}\vec{\varphi}(y) = \sum_{l=1}^{N} e^{-i\tilde{K}lw}\vec{\varphi}(lw) \sum_{m=-\infty}^{+\infty} \mathrm{sinc}(\frac{y-(l+mN)w}{w}) \,, \tag{A.7}$$

and thus

$$\vec{\varphi}(y) = e^{i\tilde{K}y} \sum_{l=1}^{N} e^{-i\tilde{K}lw}\vec{\varphi}(lw) \sum_{m=-\infty}^{+\infty} \mathrm{sinc}(\frac{y-(l+mN)w}{w}) \,, \tag{A.8}$$

and

$$h(y) = \sum_{l=1}^{N} e^{-i\tilde{K}lw} h(lw) \sum_{m=-\infty}^{+\infty} \mathrm{sinc}(\frac{y-(l+mN)w}{w}) \,. \tag{A.9}$$

Moreover,

$$\begin{aligned} \frac{d}{dy}\vec{\varphi}(y) = e^{i\tilde{K}y} \sum_{l=1}^{N} e^{-i\tilde{K}lw}\vec{\varphi}(lw) \sum_{m=-\infty}^{+\infty} \Big[& i\tilde{K}\mathrm{sinc}(\frac{y-(l+mN)w}{w}) + \\ & \frac{d}{dy}\mathrm{sinc}(\frac{y-(l+mN)w}{w}) \Big] \,. \end{aligned} \tag{A.10}$$

By substituting these expressions in the first of Eqs. (1.42), we obtain

Other approaches to the solution of the one-dimensional Dirac equation in AGRN

$$\sigma_z \sum_{l=1}^{N} e^{-i\tilde{K}lw}\vec{\varphi}(lw) \sum_{m=-\infty}^{+\infty} \Big[i\tilde{K}\mathrm{sinc}(\frac{y-(l+mN)w}{w}) + \frac{d}{dy}\mathrm{sinc}(\frac{y-(l+mN)w}{w}) \Big] + \sigma_x \sum_{l,p=1}^{N} h(pw)e^{-i\tilde{K}lw}\vec{\varphi}(lw) \times \sum_{m,k=-\infty}^{+\infty} \mathrm{sinc}(\frac{y-(p+kN)w}{w})\mathrm{sinc}(\frac{y-(l+mN)w}{w}) = - k_x \sum_{l=1}^{N} e^{-i\tilde{K}lw}\vec{\varphi}(lw) \sum_{m=-\infty}^{+\infty} \mathrm{sinc}(\frac{y-(l+mN)w}{w}) \,. \tag{A.11}$$

We can obtain a set of N independent equation by projecting Eq. (A.11) over the functions $\{\mathrm{sinc}(\frac{y-nw}{w})\}$, $n = 1, \ldots, N$. We use the scalar product

$$\langle f(y)|z(y)\rangle = \frac{1}{w}\int_{-\infty}^{+\infty} f(y)z(y)dy \,, \tag{A.12}$$

with respect to which the functions $\{\mathrm{sinc}(\frac{y-nw}{w})\}$, $n \in \mathbb{N}$, form an orthonormal set.

The projected equation reads

$$\sigma_z \sum_{l=1}^{N} e^{-i\tilde{K}lw}\vec{\varphi}(lw) \sum_{m=-\infty}^{+\infty} \langle \left(i\tilde{K} + \frac{d}{dy} \right) \mathrm{sinc}(\frac{y-(l+mN)w}{w})|\mathrm{sinc}(\frac{y-nw}{w})\rangle + \sigma_x \sum_{l,p=1}^{N} h(pw)e^{-i\tilde{K}lw}\vec{\varphi}(lw)\Gamma_{nl}(p) = -k_x \sum_{l=1}^{N} e^{-i\tilde{K}lw}\vec{\varphi}(lw) \times \sum_{m=-\infty}^{+\infty} \langle \mathrm{sinc}(\frac{y-nw}{w})|\mathrm{sinc}(\frac{y-(l+mN)w}{w})\rangle \,, \tag{A.13}$$

where we have set

$$\Gamma_{nl}(p) = \sum_{m,k=-\infty}^{+\infty} \mathrm{sinc}(\frac{y-(p+kN)w}{w})\mathrm{sinc}(\frac{y-(l+mN)w}{w})|\mathrm{sinc}(\frac{y-nw}{w})\rangle \,. \tag{A.14}$$

As a consequence of the orthonormality of the functions involved, we get

$$\langle \mathrm{sinc}(\frac{y-nw}{w})|\mathrm{sinc}(\frac{y-(l+mN)w}{w})\rangle = \delta_{n,l+mN}\,, \tag{A.15}$$

and, thus,

$$\sum_{m=-\infty}^{m=+\infty} \langle \mathrm{sinc}(\frac{y-nw}{w})|\mathrm{sinc}(\frac{y-(l+mN)w}{w})\rangle = \delta_{n,l}\,; \tag{A.16}$$

indeed, since $l, n = 1, \ldots, N$, the condition $n = l + mN$ for some value of m, or, equivalently, $(n-l)/N \in \mathbb{Z}$, requires $l = n$.
Eq. (A.13) can then be rewritten as

$$\begin{aligned}\sigma_z \sum_{l=1}^{N} \Bigg[e^{i\tilde{K}(n-l)w} i\tilde{K}\delta_{nl} + \sum_{m=-\infty}^{+\infty} \langle \frac{d}{dy}\mathrm{sinc}(\frac{y-(l+mN)w}{w})|\mathrm{sinc}(\frac{y-nw}{w})\rangle + \\ \sigma_x \sum_{p=1}^{N} h(pw) e^{i\tilde{K}(n-l)w} \Gamma_{nl}(p) \Bigg] \vec{\varphi}(nw) = -k_x \vec{\varphi}(nw)\,,\end{aligned} \tag{A.17}$$

and is now apparent that it represents an algebraic eigensystem. The components of the eigenvectors are the (N) samples of the function $\vec{\varphi}(y)$ in $[0, 2\tilde{W}]$, while the eigenvalues are the opposite of the longitudinal wave vectors. The matrix of the system is composed by the 2×2 blocks

$$\begin{aligned}M_{nl} = e^{i\tilde{K}(n-l)w} i\tilde{K}\delta_{nl} + \sum_{m=-\infty}^{+\infty} \langle \frac{d}{dy}\mathrm{sinc}(\frac{y-(l+mN)w}{w})|\mathrm{sinc}(\frac{y-nw}{w})\rangle + \\ \sigma_x \sum_{p=1}^{N} h(pw) e^{i\tilde{K}(n-l)w} \Gamma_{nl}(p)\,.\end{aligned} \tag{A.18}$$

It is possible to find analytical expressions for the sum of the series involved in the previous equation, as detailed in the following.
We have found

$$\langle \frac{d}{dy}\mathrm{sinc}(\frac{y-(l+mN)w}{w})|\mathrm{sinc}(\frac{y-nw}{w})\rangle = \frac{(-1)^{n-(l+mN)}}{w[n-(l+mN)]}(1-\delta_{n,l+mN})\,, \tag{A.19}$$

and

$$\sum_{m=-\infty}^{+\infty} \langle \frac{d}{dy}\mathrm{sinc}(\frac{y-(l+mN)w}{w})|\mathrm{sinc}(\frac{y-nw}{w})\rangle = (-1)^{n-l}\frac{\pi}{wN}\times \csc\left[\frac{\pi(n-l)}{N}\right](1-\delta_{n,l})\,. \tag{A.20}$$

Concerning the terms $\Gamma_{nl}(p)$, we considered an exhaustive list of mutually exclusive cases, each one associated to a condition on the integers l, p and n. We summarize below the results we have found.

For $l \neq n$, $p \neq n$ and $l \neq p$:

$$\Gamma_{nl}(p) = \frac{(-1)^{n-l}}{2N^2}\csc\left[\pi\left(\frac{n-l}{N}\right)\right]\left\{\cot\left[\pi\left(\frac{l-p}{N}\right)\right] - \cot\left[\pi\left(\frac{n-p}{N}\right)\right] + (-1)^{n-p} - (-1)^{s-p}\csc\left[\pi\left(\frac{n-l}{N}\right)\right]\csc\left[\pi\left(\frac{n-l}{N}\right)\right]\right\}; \tag{A.21}$$

for $n = p$, $l \neq p$:

$$\Gamma_{nl}(p) = -\frac{1}{2N^2}\csc\left[\pi\left(\frac{n-l}{N}\right)\right]\left\{(-1)^{n-s}\cot\left[\pi\left(\frac{n-l}{N}\right)\right] + (-1)^{n+p}\csc\left[\pi\left(\frac{l-p}{N}\right)\right]\right\}; \tag{A.22}$$

for $n \neq p$, $l = p$:

$$\Gamma_{nl}(p) = -\frac{1}{2N^2}\csc\left[\pi\left(\frac{n-l}{N}\right)\right]\left\{(-1)^{n-s}\cot\left[\pi\left(\frac{n-l}{N}\right)\right] + (-1)^{l+p}\csc\left[\pi\left(\frac{n-p}{N}\right)\right]\right\}; \tag{A.23}$$

for $n = p = l$:

$$\Gamma_{nl}(p) = \frac{1}{4N^2} + \frac{3}{4}\,; \tag{A.24}$$

finally, for $n = l$, $l \neq p$:

$$\Gamma_{nl}(p) = \frac{1}{2N^2}\csc\left[\pi\left(\frac{n-l}{N}\right)\right]\left\{\csc\left[\pi\left(\frac{n-p}{N}\right)\right] - (-1)^{n+p}\cot\left[\pi\left(\frac{n-p}{N}\right)\right]\right\}. \tag{A.25}$$